MULTIMODALITY IMAGING IN CARDIOVASCULAR DISEASE

KAREN S. L. TEO

M.B.,B.S., F.R.A.C.P.

Discipline of Pharmacology

University of Adelaide

Adelaide, SA, 5005

AUSTRALIA

Submitted in the total fulfillment of the requirements

for the degree of Doctor of Philosophy

University of Adelaide

AUSTRALIA

November 2007

DECLARATION

I performed the research presented in this thesis within the Department of Pharmacology, University of Adelaide, Adelaide, Australia. This work contains no material which has been accepted for the award of any other degree or diploma in any university or other tertiary institution and, to the best of my knowledge and belief, contains no material previously published or written by another person, except where due reference has been made in the text. I give consent to this copy of my thesis, when deposited in the University Library, being made available for loan and photocopying, subject to the provisions of the Copyright Act 1968.

Dr. Karen S.L. Teo
University of Adelaide
Adelaide
South Australia 5000
AUSTRALIA

TABLE OF CONTENTS

ACKNOWLEDGEMENTS

I would like to thank both my supervisors, Professors Stephen Worthley and Derek Frewin. I am indebted to Professor Worthley for his mentorship and guidance throughout this thesis. Professor Worthley's intellect, vision and infectious enthusiasm have inspired me greatly and have taught me much in all aspects of research. I also acknowledge his expertise in cardiac imaging, in particular cardiovascular magnetic resonance that has provided a firm foundation for me. I would also like to thank Professor Frewin for his guidance, wisdom and support from the time that we first embarked on the project as well as throughout this thesis.

I acknowledge my fellow co-workers of the Cardiovascular Research Centre at the Royal Adelaide Hospital for their help with work related to the projects and to Adelaide Cardiac Imaging for the use of both CMR and CT for our research projects.

I also acknowledge scholarships and financial support from the Royal Adelaide Hospital (Dawes scholarship), the Cardiac Society of Australia and New Zealand (CSANZ research scholarship), Pfizer Cardiovascular Research Scholarship and the CVL Research grant (Pfizer Australia).

Thanks also to my family and friends for their support during this thesis. I especially want to thank my parents, Jenny and Pek Kim Teo for their love, guidance and encouragement throughout my life. Finally, I give thanks to God.

THESIS RELATED PUBLICATIONS

ORIGINAL RESEARCH

Teo KSL, Carbone A, Piantadosi C, Chew DP, Hammett CJ, Brown MA, Worthley SG. Cardiac MRI assessment of left and right ventricular parameters in healthy Australian normal volunteers. Heart Lung and Circulation 2008 (in press).

RELATED WORK

Duncan RF, **Teo KSL,** Worthley SG. Heart Lung and Circulation 2007. Cardiac magnetic resonance documentation of a double atrial septal defect before and after percutaneous closure with an Amplatzer septal occluder. Int J Cardiol. 2007 (in press).

O'Hanlon R, **Teo KSL,** Buchiarelli-Ducci C, Pennell DJ. Perfusion CMR and SPECT in hypertrophic cardiomyopathy. Int J Cardiol. 2007 (in press).

Teo KSL, Roberts-Thomson KC, Worthley SG. Utility of intravascular ultrasound in the diagnosis of ambiguous calcific left main stenoses. J Invasive Cardiol. 2004 Jul; 16(7): 385.

Roberts-Thomson KC, **Teo KSL,** Stuklis R, Worthley SG. Left atrial myxoma: magnet or echo? Intern Med J. 2004 Apr; 34(4): 210-1.

PRESENTATIONS

Cardiovascular MR Advances and Read with the Experts: 10th Annual Course, National Heart and Lung Institute, London. November 2006. Read with the experts session (Cases in Heart Failure: Co-presenter).

THESIS RELATED ABSTRACTS

Teo KSL, Korlaet M, Lott C, Brown MA, Worthley SG. Comparison of four and sixteen detector MDCT for noninvasive coronary angiographic imaging. *51st Scientific Sessions of the Cardiac Society of Australia and New Zealand*, Adelaide, August 2003.

Teo KSL, Ellis C, Lennon-George J, Fowler SM, Keenan RJ, Worthley SG. Cardiac MRI determines reproducibly left ventricular parameters in normal volunteers. *51st Scientific Sessions of the Cardiac Society of Australia and New Zealand*, Adelaide, August 2003.

Teo KSL, Ellis C, Lennon-George J, Keenan RJ, Worthley SG. Cardiac MRI determines reproducibly left ventricular parameters in normal volunteers. *Royal Australian and New Zealand College of Radiologists 54th Annual Scientific Meeting*, Brisbane, September 2003.

Teo KSL, Parkin G, Keenan RJ, Brown MA, Worthley SG. Tricuspid valve position using Cardiac MRI: Establishment of a surface anatomical algorithm for central venous pressure zero point. *Royal Australian and New Zealand College of Radiologists 54th Annual Scientific Meeting*, Brisbane, September 2003.

Lott C**, Teo KSL,** Korlaet M, Brown MA, Worthley. Comparison of Four and Sixteen Multi-detector CT for non-invasive coronary angiographic imaging. *Royal Australian and New Zealand College of Radiologists 54th Annual Scientific Meeting*, Brisbane, September 2003.

Teo KSL, Ellis CA, Lennon-George J, Worthley SG Assessment of Atrial Septal Defects: A comparative study in adult patients with cardiac magnetic resonance and transoesophageal echocardiography. *52st Scientific Sessions of the Cardiac Society of Australia and New Zealand*, Brisbane, August 2004. Heart Lung Circulation 2004; 13(Supp) 2:S57.

Teo KSL, Campbell P, Zaman AG, Worthley SG. Coronary Artery Bypass Graft Assessment with multi-detector CT in asymptomatic patients. *52st Scientific Sessions of the Cardiac Society of Australia and New Zealand*, Brisbane, August 2004. Heart Lung Circulation 2004;13(Supp)2:S58

Teo KSL, Ellis CA, Lennon-George J, Worthley SG. Assessment of Atrial Septal Defects: A comparative study in adult patients with cardiac magnetic resonance and transoesophageal echocardiography. *European Society of Cardiology Congress*, Munich, Germany, August 2004.

Brown G, Pontre B, **Teo KSL**, Taylor J, St.Pierre T, Chua-anusorn W, Worthley SG T2* Relaxometry in Secondary Haemochromatosis: Impact of Techinical Variations. *13th Scientific Meeting & Exhibition of the International Society for Magnetic Resonance in Medicine*, Miami, Florida, May 2005

Teo KSL, Grieve SM, Hammett, CJK, Piantadosi C, Chew DP, Korlaet M, Worthley SG. Common Carotid artery wall assessment with MRI: variations

between patients with severe versus absent internal carotid disease. *53rd Scientific Sessions of the Cardiac Society of Australia and New Zealand*, Perth, August 2005

Teo KSL, Piantadosi C, Hammett CJK, Ellis CA, Lennon-George J, Worthley SG. Utility of cardiovascular magnetic resonance in assessing cardiac volumes pre- and post- percutaneous ASD closure: A serial study. *53rd Scientific Sessions of the Cardiac Society of Australia and New Zealand*, Perth, August 2005. Heart Lung Circulation 2005;14S-S39.

Hammett CJK, **Teo KSL**, Piantadosi C, Grieve SM, Chew DP, Lennon-George J, Ellis CA, Worthley SG. Assessment of common and internal carotid artery vessel wall area: a feasibility study using high resolution MRI. *53rd Scientific Sessions of the Cardiac Society of Australia and New Zealand*, Perth, August 2005. Heart Lung Circulation 2005; 14(Supp) 1:S40.

Grieve SM, **Teo KSL,** Piantadosi C, Hammett CJK, Worthley SG. Algorithm for co-registration and analysis of mulit-contrast MRI sequence: utility in carotid atherosclerosis. *53rd Scientific Sessions of the Cardiac Society of Australia and New Zealand*, Perth, August 2005. Heart Lung Circulation 2005; 14(Supp) 1-S41.

Pontre B, Brown G, **Teo KSL**, Chua-anusorn W, St.Pierre T, Worthley SG. Iron Deposition patterns in the liver and heart of patients with beta-Thalassaemia: an MRI analysis. *53rd Scientific Sessions of the Cardiac Society of Australia and New Zealand*, Perth, August 2005. Heart Lung Circulation 2005;14S:S39.

Farquharson AL, Magarey J, **Teo KSL**, Roberts-Thomson K, Hutchinson MR. Comparison of manual anterolateral cardioversion with remote anteroposterior cardioversion of atrial fibrillation using current biphasic defibrillation. *53rd Scientific Sessions of the Cardiac Society of Australia and New Zealand*, Perth, August 2005.

Hammett CJK, **Teo KSL**, Piantadosi C, Grieve SM, Chew DP, Lennon-George J, Ellis CA, Worthley SG. Assessment of common and internal carotid artery vessel wall area: a feasibility study using high resolution MRI. *European Society of Cardiology Congress*, Stockholm, Sweden September 2005.

Teo KSL, Piantadosi C, Brown MA, Worthley MI, Disney PJ, Hammett CJK, Waddy PJ, Sanders P, Worthley SG. Percutaneous closure of atrial septal defects leads to a reduction in right ventricular volumes and corresponding normalisation of left ventricular volumes: ventricular interdependence and cardiac MRI. *54th Scientific Sessions of the Cardiac Society of Australia and New Zealand*, Canberra, August 2006. Heart, Lung and Circulation 2006;15S-83.

Teo KSL, Grieve SM, Worthley MI, Korlaet MB, Brown MA, Fitridge R, Thomas A, Carbone A, Worthley SG. Multi-detector CT imaging fails to accurately quantify vessel wall calcification: analysis of multiple algorithms and comparison with micro CT. *54th Scientific Sessions of the Cardiac Society*

of Australia and New Zealand, Canberra, August 2006. Heart, Lung and Circulation 2006;15S-85.

Teo KSL, Nicholls SJ, Kee P, Rye KA, Barter PJ, Worthley SG. Combination high-density lipoprotein infusion and atorvastatin significantly reduces experimental atherosclerosis compared to either therapy alone: serial analysis with high-resolution MRI. *54th Scientific Sessions of the Cardiac Society of Australia and New Zealand*, Canberra, August 2006. Heart, Lung and Circulation 2006;15S-86.

Greenwell TH**, Teo KSL**, Chew DP, Hammett CJK, Piantadosi C, Carbone A, Worthley MI, Worthley SG. Early Atherosclerotic Disease in the Carotid and Coronary Territories in At-Risk Individuals. *54th Scientific Sessions of the Cardiac Society of Australia and New Zealand*, Canberra, August 2006. Heart, Lung and Circulation 2006; 15S-111. Heart Lung Circulation 2006; 15 (Supp) 1:S47.

Teo KSL, Nicholls SJ, Kee P, Rye KA, Barter PJ, Worthley SG. Combination high-density lipoprotein infusion and atorvastatin significantly reduces experimental atherosclerosis compared to either therapy alone: serial analysis with high-resolution MRI. *European Society of Cardiology Congress*, Barcelona, Spain September 2006. European Heart Journal 2006,27(1): 827, P 5517.

Piantadosi C, Worthley MI, **Teo KSL**, Nalivaiko E, McAinch A, Wittert GA, Worthley SG. Effects of obesity and diet induced weight loss on Cardiovascular risk factors, vascular and ventricular structure and function in obsess men. International Atherosclerosis Society Scientific Sessions, Rome, Italy June 2006.

Leung MCH, Brown GC, Young AA, Cowan BR, Pontré B, **Teo KSL**, St. Pierre T, S.G. Worthley SG. 3D MRI Myocardial Strain in Patients with Transfusion-Induced Haemochromatosis. *55th Scientific Sessions of the Cardiac Society of Australia and New Zealand*, Christchurch, August 2007. Heart, Lung and Circulation 2007; 16 (Supp 2), S45.

Liew G, Hammett C, Dundon B, **Teo KSL**, M. Worthley MI, Nicholls SJ, Zaman A, Worthley SG Multi-Detector Computed Tomography (MDCT) and Magnetic Resonance Imaging (MRI) Non-Invasively Quantifies Saphenous Vein Graft Atherosclerotic Plaque: A Comparison with Intravascular Ultrasound (IVUS). *55th Scientific Sessions of the Cardiac Society of Australia and New Zealand*, Christchurch, August 2007. Heart, Lung and Circulation 2007; 16 (Supp 2), S45.

Liew G, Hammett C, Dundon B, **Teo KSL**, Worthley MI, Nicholls SJ, Zaman A, Worthley SG. Predictors of Atheroembolic Complications During Saphenous Vein Graft Percutaneous Coronary Intervention. *55th Scientific Sessions of the Cardiac Society of Australia and New Zealand*, Christchurch, August 2007. Heart, Lung and Circulation 2007; 16 (Supp 2), S105.

THESIS RELATED AWARD

Oral Presentation Winner: Diagnostic Imaging Paper (Mayne Health Scientific Paper Prize). Annual Scientific Sessions of the Royal Australian and New Zealand College of Radiology 2003, Brisbane, Australia

Abstract: Cardiac MRI determines reproducibly left ventricular parameters in normal volunteers.

Authors: **Teo KSL**, Ellis C, Lennon-George J, Fowler SM, Keenan RJ, Worthley SG.

LIST OF ABBREVIATIONS

ASD	Atrial septal defect
CAC	Coronary Artery Calcium
CNR	Contrast-to-Noise
CT	Computerised Tomography
CMR	Cardiovascular Magnetic Resonance
EBCT	Electron Beam Computerised Tomography
ECG	Electrocardiograph
ESP	Echo Spacing
ETL	Echo Train Length
FOV	Field Of View
FSE	Fast Spin Echo
Gd-DTPA	Gadolinium-DiethyleneTriamine PentaAcetate
HDL	High Density Lipoprotein
HU	Hounsfield Units
IVUS	Intravascular Ultrasound
LAD	Left Anterior Descending
LCx	Left Circumflex
LDL	Low Density Lipoprotein
LV	Left ventricle
MHz	Megahertz
MRI / MR	Magnetic Resonance Imaging / Magnetic Resonance
MWT	Mean Wall Thickness
NMR	Nuclear Magnetic Resonance
PDW	Proton Density Weighted
PET	Positron Emission Tomography
RCA	Right Coronary Artery
RF	Radiofrequency
RV	Right ventricle
SD	Standard Deviation
SEM	Standard Error of the Mean
SSFP	Steady-state free precession
T	Tesla
TE	Echo Time

TGF-β	Transforming Growth Factor-β
TI	Inversion Time
TOF	Time Of Flight
tPA	tissue-type Plasminogen Activator
TR	Recovery Time
T1W	T1 Weighted
T2W	T2 Weighted
VCAM-1	Vascular Cellular Adhesion Molecule-1
VEC	Velocity Encoded Contrast
VWA	Vessel Wall Area

SYNOPSIS

The non-invasive cardiovascular imaging modalities, cardiovascular magnetic resonance (CMR) and multi-detector computer tomography (MDCT) are playing an increasing role in both clinical and research settings.

CMR is a unique imaging modality due to unsurpassed contrast between soft tissue structures that is non-invasive, does not use ionising radiation and is able to provide high-resolution information about cardiac anatomy, function, flow, perfusion, viability and metabolism. It has provided the gold standard in imaging in congenital heart disease. Recent advances in this technology have led to images of high spatial and temporal resolution that has made the characterisation of atheroma possible. While currently spatial resolution still limits its ability to characterise atheroma in native human coronary arteries in living patients, CMR imaging of the coronary arteries has future potential with further technological and sequence advances.

MDCT has been used in clinical settings to measure of the amount of calcification in the coronary arteries with “coronary artery calcium scoring” of the coronary tree a surrogate marker of atherosclerosis. MDCT has also become the gold standard for angiographic imaging in most arterial beds such as the carotid and peripheral vascular systems. In the coronary arteries in particular, there have been major advances in the accuracy of coronary MDCT angiography, particularly with regards to its negative predictive value, although excessive calcification and blooming artefacts still limit the diagnostic accuracy of the technique for assessing stenotic severity.

In this thesis, our aims were to address some specific novel areas advancing the utility of these imaging modalities in two major areas of interest, namely congenital heart disease and atheroma imaging.

Our first step was to validate the accuracy and reproducibility of CMR, the main imaging modality we utilised. To achieve this, we assessed MR imaging of cardiac volumes and function in a normal adult Australian population with a specific focus on the reproducibility of the technique. In confirming that this technique in our hands is both accurate and reproducible, we would then be in a position to be able to confidently use this technique in our future chapters. However, more than this, we sought to establish some normal ranges for left and right atrial and ventricular parameters in our local population. This would be crucial background information for us to be able to make comparisons with future studies in patients with congenital heart disease.

Having established our technique and reference ranges, we would then explore the two specific issues in the ensuing two chapters using CMR in one area of congenital heart disease, atrial septal defect. Atrial septal defect is the most common congenital heart defect first diagnosed in adults. The traditional method of assessment of these patients and for suitability for ASD closure involves semi-invasive investigation with transoesophageal echocardiography (TOE) for measurement of the defect size and atrial septal margins. MRI assessment of patients prior to percutaneous device closure compared to TOE assessment would provide information on the accuracy of TOE assessment and provide information of the utility of cardiac MRI as an alternative to TOE for the work-up of these patients prior to ASD closure.

In our third original research chapter, we utilised CMR to understand the effects of percutaneous ASD closure on cardiac chamber volumes. We achieved this by assessing with cardiac MRI pre-closure and post-closure atrial and ventricular cardiac volumes. Longstanding right heart dilatation in the setting of an ASD may lead to complications including right heart failure, pulmonary hypertension and arrhythmia. Closure of the ASD should reduce right heart volumes by removing left-to-right shunting and lead to normalisation of ventricular volumes. The assessment of atrial volume changes with ASD closure may be important in furthering our understanding in its contribution to arrhythmia.

Having assessed the ability of CMR to assess both the ASD dimensions, and therefore suitability for percutaneous closure, as well as the effects of ASD closure on cardiac chamber size, we look in the final two original research chapters to move to another area of research development with these high-resolution imaging technologies, atherosclerosis imaging. Two particular areas we wished to focus on included the potential of high-resolution MR imaging to monitor effects of HDL infusion on atherosclerosis, and secondly to explore mechanisms behind limitations in MDCT imaging of atherosclerosis, specifically calcification and blooming artifacts.

For assessing the effects of HDL infusion on atherosclerosis, we utilised a cholesterol-fed rabbit model of atherosclerosis. The abdominal aorta of the rabbit is comparable in size to the human coronary artery. Previous work with the rabbit model of atherosclerosis and magnetic resonance imaging of the aortic wall has

shown that it can provide information about atherosclerotic composition as well as provide serial data of the arterial wall. While high intensity lipid-lowering with statins remains the first line management of at risk individuals, modest manipulations of serum HDL levels are associated with a significant impact on cardiovascular risk. Thus, we assessed the effect of HDL infusion and atorvastatin in a rabbit model of using MRI aortic atherosclerosis as the end-point.

In our fifth and final original research chapter, we assessed the accuracy of quantification of atherosclerotic calcification with MDCT in the carotid arteries of patients undergoing carotid endarterectomy, and sought to identify algorithms or techniques that may improve quantification of calcification. This would potentially lead to an improvement in the ability of MDCT techniques to quantify stenotic severity in coronary arteries that were calcified. To achieve these we utilised MDCT in vivo and in comparison with carotid endarterectomy specimen micro-CT. Importantly, as part of this study, we undertook a thorough assessment of reproducibility of these techniques.

Thus, in summary, we have been able to confirm the accuracy and reproducibility of CMR and MDCT in the areas of a specific congenital defect (ASD) and atherosclerosis imaging, and utilised these techniques to advance our understanding of these disease states. This thesis identifies strengths and weaknesses of these techniques that will allow us to more appropriately use them for future purposes in cardiovascular disease. Future work directly stemming from this thesis has already begun, and now looks to address issues of whether CMR and MDCT may provide complimentary information about atherosclerotic

lesions that may benefit outcomes in certain conditions. Specifically the work in this thesis has led to studies commencing in carotid atherosclerosis and saphenous vein graft atherosclerosis and using these imaging techniques to potentially predict adverse future outcomes.

Chapter 1

INTRODUCTION

TABLE OF CONTENTS

1. 1. BACKGROUND

Cardiovascular disease due to the complications of atherosclerosis remains the leading cause of premature death and disability in Western Society. It causes 38% of all deaths in Australia (Australian Institute of Health and Welfare. et al. 2004) and the total burden of cardiovascular disease is expected to increase due to an increasingly elderly population. The prevention, identification and management of coronary heart disease remain a significant challenge. Non-invasive cardiovascular imaging modalities including the newer technologies of cardiovascular magnetic resonance and multi-detector computer tomography are playing an increasing role in both clinical and research settings. In particular, these modalities have the potential to increase our recognition and understanding of cardiovascular disease in both symptomatic and asymptomatic individuals.

Cardiovascular magnetic resonance (CMR) is a unique imaging modality due to unsurpassed contrast between soft tissue structures. It is non-invasive, does not use ionising radiation and is able to provide high-resolution information about cardiac anatomy, function, flow, perfusion, viability and metabolism. CMR has become the gold standard imaging in certain areas of congenital heart disease and there are increasing roles for CMR in the assessment of paediatric and adult patients with congenital heart disease (Wood 2006). Recent advances in CMR technology have led to images of high spatial and temporal resolution that has made the characterisation of atheroma possible (Cai et al. 2005; Helft et al. 2001; Worthley et al. 2000). While spatial resolution still limits its ability to characterise atheroma in native human coronary arteries in living patients, CMR imaging of the coronary arteries has future potential with further technological and sequence advances.

Multidetector computer tomography (MDCT) has been used in clinical settings to measure the amount of calcification in the coronary arteries with coronary artery calcium scoring of the coronary tree as a surrogate marker of atherosclerosis. MDCT has also become the gold standard for angiographic imaging in most arterial beds such as the carotid and peripheral vascular systems. In the coronary arteries, there have been major advances in the accuracy of coronary MDCT angiography, particularly with regards to its negative predictive value, although excessive calcification and blooming artefacts still limit the diagnostic accuracy of the technique for assessing stenotic severity.

1. 2. CARDIOVASCULAR MAGNETIC RESONANCE

Cardiovascular magnetic resonance (CMR) has in recent years emerged as a non-invasive cardiovascular imaging modality with increasing application in both clinical and research settings. CMR is able to provide information about cardiac anatomy, function, flow, perfusion and metabolism. It is completely non-invasive and does not use ionising radiation. It allows the free choice of tomographic planes. Of all the imaging modalities currently available, it provides the greatest intrinsic contrast between soft tissue structures producing images of high spatial and temporal resolution. Its limitations are the relatively long imaging time, relative isolation of the patient from medical care during image acquisition and contraindications in patients with certain metallic implants such as permanent pacemakers and intracerebral metallic clips. There are also a small, but significant number of patients who are unable to undergo CMR imaging because of claustrophobia.

1. 2. 1. Magnetic Resonance Basics

Magnetic resonance (MR) imaging is based on the detection of hydrogen ions (protons), largely water and fat within the body. These protons have an intrinsic angular momentum or spin and the frequency of the spin is related to the magnitude of the magnetic field and its intrinsic gyromagnetic ratio. The proton spins in a magnet are randomly distributed around the axis of a magnet and as a result, there is no net signal to detect. When placed within a strong magnetic field, a person becomes partially magnetised due to the effect associated with hydrogen ions (protons) within the body. To detect a MR signal, a magnetic field is applied perpendicular to the main magnetic field, which causes the protons in the body to be aligned. By subjecting the person to different and subsequent magnetic fields perpendicular to the first magnetic field, the vector of magnetisation within the person changes. These changing magnetic fields emit radiofrequency waves and the collection of this information is detected with receiver coils that can be translated into the final MR image.

The characteristics of these radiofrequency waves and subsequent signals detected are determined by many factors. This includes the parameters of MR techniques, such as relaxation times, proton density, motion and flow, molecular diffusion, magnetization transfer and changes in susceptibility. The signals detected are also affected by the tissues themselves which allows for the accurate differentiation between the soft tissue components of the body.

Following a radiofrequency (RF) excitation pulse, each voxel will contain a certain amount of precessing net magnetization, which will then induce an oscillating current or signal in the RF receiver coil. In time, the signal from each voxel will

decay under the influence of the various relaxation processes T1, T2 and T2*. T1 determines the loss of transverse magnetization as it relaxes back to the longitudinal axis. T2 and T2* characterise the phase coherence of the remaining net magnetization in the transverse plane.

Tissues with different relaxation properties will lead to a signal difference or contrast, which can be used to distinguish different voxels from each other and thus distinguish different tissue types. A T1 weighted image has a contrast that shows high signal intensity for those voxels containing tissues with short T1 values and low signal for voxels with tissues having long T1 values. A T2 weighted image has high signal for voxels containing tissues with long T2 values and low signal for voxels containing tissues with short T2 values. A proton-density weighted image, a measurement of the net magnetization before any of the relaxation processes have had a significant effect, has a high signal from voxels with a high equilibrium net magnetization (Lardo 2003).

A great strength of MRI is the ability to create many different image contrasts by manipulating the image timing parameters, thus enabling the differentiation of various tissues.

1. 2. 2. MR pulse sequences

There are three main imaging sequences that are currently being used: gradient echo imaging, spin echo imaging and steady-state free precession imaging.

To sample data for all of k-space, pulses (RF pulse, frequency encoding, phase encoding gradients) must be repeated a number of times to reconstruct a 2D image.

In successive repetitions, the amplitude of the phase-encoding gradient is changed to sample different lines of k-space. The time to repeat the pulses is called the repetition time (TR). The time from the centre of the RF pulse to the echo peak is called the echo time (TE).

1. 2. 2. 1. Spin Echo Imaging

Spin echo imaging is able to provide excellent discrimination between various components of the heart. This imaging sequence has traditionally been used for the imaging of static phenomena such as myocardial wall thickness, cardiac chamber volumes and intracardiac thrombus.

In a spin echo sequence, spins are first excited by a 90 degree RF pulse in the presence of a slice-selection gradient. However, in contrast to gradient echo imaging, a spin echo pulse sequence then uses a refocusing RF pulse (180 degree pulse) to eliminate signal loss due to static magnetic field inhomogeneity. This refocusing pulse is placed at the time t=TE/2 and flips the transverse magnetization during the subsequent period of duration TE/2 that phase accumulation due to static magnetic field inhomogeneity cancels the phase accumulation of the initial period TE/2. The echo that refocuses at the time TE is referred to as a spin echo and this is significantly less sensitive than a gradient echo due to signal loss from static field inhomogeneity. In spin echo imaging, blood flowing rapidly through the image plane appears dark (“black blood” images) as any spins that are excited by the initial 90 degree radiofrequency pulse dephase and are rephased by the subsequent 180 degree radiofrequency pulse. Spin echo sequences have a generally increased tissue contrast and relatively reduced sensitivity to small magnetic field inhomogeneities caused by metallic implants (Manning and Pennell 2002).

Conventional spin echo imaging acquires a single line of k-space data per slice and this is susceptible to respiratory artefacts. To overcome this, techniques that utilise shorter imaging times are used. The fast or turbo spin echo sequence encodes for multiple k-space lines after a single 90 degree radiofrequency excitation pulse via a train of refocusing 180 degree radiofrequency pulses. This produces shorter imaging time and reduced respiratory motion artefacts. In addition, to ensure that a signal from blood is adequately suppressed, a double inversion recovery magnetization preparation pulse is used (Simonetti et al. 1996). A slice-selective inversion pulse then restores the magnetization within the imaged slice.

In T1-weighted images, the repetition time (TR) is short relative to T1 and TE is short relative to T2. In T2-weighted images, TR is long (usually equal to 2 or more R-R intervals) and TE is long. In proton density weighted images, TR is long and TE is short. To generate an image of a specific spatial resolution and image field of view (FOV), data for a minimal set of spatial frequencies or k-space lines must be sampled. In each R-R interval, data at different spatial locations are acquired with the same k-space encoding value and therefore images at different spatial locations are at a different temporal phase of the cardiac cycle. Only one k-space is acquired per cardiac trigger and thus a scan with 128 k-spaces in the phase encoding direction will take 128 heartbeats to complete for a T1-weighted image or 256 beats for a T2-weighted image where TR is equal to 2 R-R. Spin-echo images are usually acquired with 2 signal averages. T2 weighted images are lower quality compared to T1-weighted images because of the lower signal-to noise ratio due to the longer TE and longer acquisition time.

1. 2. 2. 2. Gradient Echo Imaging

A gradient echo sequence uses a single slice-selective RF pulse of flip-angle α generally $\leq$ 90 degrees. There is no slice-selective refocusing pulse and subsequent slice-selective excitation results in partial saturation of the spins remaining. As blood flowing into the slice during the interpulse interval has been affected by the earlier pulses, it contributes to a greater signal than stationary tissue (Manning and Pennell 2002). Thus, in gradient echo imaging, flowing blood appears white ("bright blood" imaging). The gradient echo-sequence can be repeated rapidly using a reduced flip angle so that saturation does not occur and allows for cardiac cine imaging of the heart for the assessment of myocardial function and vascular lumen angiography (Mohiaddin 2002). Real-time imaging is possible with the advent of extremely rapid image acquisition (10 to 15 images per second).

However, gradient echo imaging provides less tissue contrast compared with spin echo imaging. The gradient echo images are mainly T1-weighted and are characterised by short sequence repetition times, flip angles of less than 90 degrees and greater signal intensity of the ventricular blood pool compared to that of myocardium.

Gradient echo cine imaging can be sensitive to signal loss due to inhomogeneity of the static magnetic field from the interaction of the applied magnetic field with multiple tissues such as the heart, lung and liver that have different magnetic susceptibilities. The amount of spin dephasing increases linearly with TE, thus to minimise these artefacts, short TE is important in gradient echo imaging.

1. 2. 2. 3. Steady-state free precession cine MRI

Conventional gradient echo imaging uses RF excitation pulses to create transverse magnetization from longitudinal magnetization, then samples the signal generated by precessing transverse magnetization while a gradient echo is formed. A gradient pulse is then applied to cause phase incoherence of the transverse magnetization (also called “spoiling” of the transverse magnetization) before the sequence is repeated.

Improvement of gradient hardware capable of fast slew rates and high gradient strengths has resulted in a newer technique called steady-state free precession (SSFP) imaging. These sequences rephase, rather than discard or “spoil” the transverse magnetization as in conventional gradient echo imaging and thus, the transverse magnetization can be used to achieve higher signal to noise ratio and improved blood-myocardium contrast (Moon et al. 2002), while also allowing allows faster imaging times.

Blood appears very bright in SSFP images because T2/T1 is large while myocardium appears relatively dark on SSFP because T2/T1 is small. SSFP imaging is now used in the assessment of cardiac function as well as in other applications such as myocardial perfusion and myocardial viability assessment.

1. 2. 3. CMR of Ventricular Function

CMR is an accurate and reproducible tool for the assessment of both left and right ventricular function assessment (Longmore et al. 1985; Semelka et al. 1990). The information that can be obtained in a single examination includes cardiac anatomy, ventricular volumes, ventricular mass and ejection fraction which provide both

diagnostic and prognostic information (Haider et al. 1998; Rehr et al. 1985; Semelka et al. 1990). As it is non-invasive and does not utilise ionising radiation, it is ideal for serial assessments such as the assessment of response to therapeutic interventions in both clinical and research settings that will help to further our understanding of the effects of such therapies.

1. 2. 3. 1. Accuracy of CMR

The accuracy of ventricular volume measurements has been shown in *ex vivo* studies that have compared CMR assessment of left ventricles with water displacement volumes of human cadaveric casts of the left ventricle (Longmore et al. 1985; Rehr et al. 1985) and right ventricle (Jauhiainen et al. 1998). Measurement of LV mass by CMR has been validated in human autopsy hearts and in animals (Katz et al. 1988) while right ventricular mass measurements have been validated against *ex vivo* animal hearts (Katz et al. 1993).

1. 2. 3. 2. Reproducibility of CMR

Echocardiography is a widely available, non-invasive technique that is used for assessment of the left ventricle. However, image acquisition depends on the operator and acoustic window. It also relies on geometric assumptions, in particular in M-mode echocardiography, where a single basal slice is used to calculate ejection fraction and left ventricular mass. The left ventricle is assumed to have a uniform geometric shape with no regional variation in wall thickness or thickening. Two-dimensional echocardiography is more accurate and reproducible than with M-mode echocardiography as it takes into account the length of the cavity as well as thickness. This is based on Simpson’s biplane method of discs and relies on

planimetry of the endocardial border in end-diastolic and end-systolic frames. However, this still assumes an ellipsoid shape, a uniform wall thickness and good visualisation of the endocardial border which is not seen in up to one-third of patients (Bellenger et al. 2000; Teichholz et al. 1976).

CMR has the advantages of being independent of geometric assumptions (Doherty et al. 1992) and has been shown to be both accurate (Longmore et al. 1985) and reproducible (Alfakih et al. 2003; Grothues et al. 2004; Semelka et al. 1990). CMR has improved inter-study reproducibility in the assessment of left and right ventricular volumes, function and mass. When directly compared to 2D echocardiography, the interstudy reproducibility coefficient of variability was superior for CMR for all parameters (LV ESV 4.4 to 9.2 % versus 13.7% to 20.3%, LV EF 2.4 to 7.3% versus 8.6 to 19.4%, LV mass 2.8% to 4.8% versus 11.6% to 15.7%, $p < 0.001$) {Grothues, 2002 #391}. The improved reproducibility for CMR has also been shown to result in significant reductions in sample sizes required in studies using CMR (reductions of 55 to 93%) compared to echocardiography (Bellenger et al. 2000; Grothues et al. 2004). Thus, CMR allows reproducible serial assessments of ventricular parameters and monitoring of remodelling with therapy.

1. 2. 3. 3. Image acquisition

The ventricular assessment with CMR is performed in a standardised way, with the acquisition of long-axis cine images as well as a stack of 10 to 12 long axis images. A cine image is acquired in a breath-hold of about 10 seconds and a ventricular stack acquired in about 5 minutes. All images are acquired over several cardiac cycles during a breath-hold. The final image is averaged from the data acquired across these cardiac cycles. Images are electrocardiograph (ECG)- gated either prospectively or

retrospectively. Retrospective ECG gating by the scanner ensures that the end of diastole is not missed, which may occur with the earlier prospective triggering approaches (Gatehouse and Firmin 2000).

1. 2. 3. 4. CMR pulse sequences

There are two main pulse sequences used for the assessment of ventricular volumes and function. The first is with conventional gradient-echo sequences that have been shown to be accurate and reproducible (Pattynama et al. 1993; Semelka et al. 1990; Shapiro et al. 1989). The second, more recent technique is with steady-state free precession (SSFP) imaging. Steady-state free precession sequences have been designated as fast imaging with steady-state precession (FISP), balanced fast-field echo imaging; or fast imaging employing steady-state acquisition (FIESTA) depending on the manufacturer.

SSFP sequences rephase the transverse magnetization that undergoes dephasing during phase encoding and readout between radiofrequency pulses, and imaging occurs when all transverse and longitudinal magnetisation components are at steady state. This improves the signal to noise ratio, thus improving blood-myocardium contrast and also allows faster imaging times. SSFP imaging is less dependent on blood flow (Moon et al. 2002). However, there remains the potential for artefact from field inhomogeneities, susceptibility effects and artefacts related to eddy current induction (Moon et al. 2002). Due to these characteristics, cardiac volume, mass and function analysis may differ between SSFP and conventional gradient-echo sequences. Gradient echo and SSFP techniques have been compared, with measurements for LV and RV end-diastolic volumes larger ($p<0.0001$) while those for LV and RV EF were smaller ($p=0.0001$ and 0.0005) with SSFP techniques. LV

mass was also smaller with the SSFP technique. The significant difference for all the parameters remained even with indexation to height and body surface area (Alfakih et al. 2003). SSFP has a typical in-plane resolution of 1.4 x 1.8 mm, a slice thickness of 6 to 8 mm and a typical temporal resolution of 50ms.

1. 2. 3. 5. Assessment of the right ventricle

CMR can be used for the assessment of the human right ventricle despite its complex triangular cavity shape and distinct inflow and outflow tracts. Right ventricular function is an important determinant in the prognosis of myocardial infarction (Mehta et al. 2001) and chronic heart failure (Oakley 1988), in addition to its major role in congenital heart disease (Davlouros et al. 2006). Lower interstudy reproducibility of the right ventricle compared to LV may be due to factors such as difficulty defining the most basal RV slice due to the large area of the basal slice which includes the RV outflow tract and the inflow region with the tricuspid valve. Endocardial boundary delineation can also be more difficult for the RV with its thin free wall, increased trabeculation compared to the LV and variable structure of the moderator band.

1. 2. 3. 6. Limitations of CMR in ventricular assessment

Partial volume effect is a known problem in volumetric measurements by CMR (Luft et al. 1996). When section thickness is 7 to 10 mm, one voxel can encompass different structures causing blurring of the anatomic boundaries and small errors in anatomic analysis with volumetric error increasing with slice thickness (Jauhiainen et al. 1998; Luft et al. 1996). Cardiac motion during *in vivo* imaging with ventricles

contracting, rotating and shortening in addition to the heart moving with the diaphragm during the respiratory cycle can also cause errors in volume analysis.

Poor breath hold during image acquisition may be a problem with patients who have left ventricular dysfunction. Ways to reduce breath hold time include reducing the temporal resolution of the image and more recently with newer imaging techniques such as parallel-imaging techniques. These reduce imaging time by acquiring multiple lines of data simultaneously, thus providing the full spatial information needed to form an image of a given spatial resolution and field of view (Niendorf and Sodickson 2006). If breath holding is not possible, real-time imaging where the image is acquired in one cardiac cycle rather than several cycles, although the limitation of this is reduced image resolution (Yang et al. 1998).

1. 2. 4. Myocardial tagging

Myocardial tagging is a CMR technique used for the determination of the thickening and torsion of specific myocardial segments. The underlying principle is to apply selective saturation pre-pulses in late diastole to superimpose grid lines across the field of view and thus create non-invasive markers within the heart. These grid lines are deformed by myocardial contraction, torsion and strain (Gotte et al. 2006). Myocardial thickening and rotational torsion can then be quantified.

Information about myocardial strain is currently obtained by echocardiography with tissue Doppler imaging based on longitudinal and radial motion data. Myocardial tagging with CMR allows the measurement of myocardial strain and has the potential of quantifying myocardial deformation in not just longitudinal and radial directions, but also in the circumferential direction. Thus myocardial tagging allows for the

evaluation of regional and diastolic myocardial function in three dimensions. This has important clinical utility in the evaluation of patients with cardiac failure. Furthermore quantification of myocardial strain and torsion and diastolic strain rate with MR myocardial tagging has the potential of early detection of cardiac disease in patients prone to the development of cardiomyopathy.

Quantitative assessment of myocardial deformation with semi-automatic analysis methods is now possible using specialised software to detect and track gridlines (Axel et al. 1992) as well as almost fully automated analysis with harmonic phase (HARP) analysis which can track points through the cardiac cycle or to calculate the deformation directly (Osman et al. 1999).

1. 2. 5. CMR of Myocardial Viability

1. 2. 5. 1. Myocardial viability

Myocardial viability assessment is important in predicting which patients with coronary disease and left ventricular impairment will have improved ventricular function and survival with revascularisation (Braunwald and Rutherford 1986; Pagley et al. 1997). Traditional methods for assessing myocardial viability include positron-emission tomography (PET), single photon emission computed tomography (SPECT) and dobutamine echocardiography. Dobutamine echocardiography and PET imaging have high positive predictive value (82%) compared to SPECT (69%). However, SPECT has a higher negative predictive value (90%) compared to both PET (83%) and dobutamine echocardiography (81%) (Bonow 1996). These techniques assess different indirect markers of cellular viability and there are limitations with each test. SPECT is susceptible to attenuation artefacts, PET

imaging is limited by high costs and dobutamine stress echocardiography is suboptimal or non-diagnostic in up to 15% of patients (Nagel et al. 1999).

CMR with a gadolinium-based contrast agent not only identifies acute myocardial infarction, but is also able to accurately identify the transmural extent of infarction and distinguish between reversible and irreversible myocardial injury (Kim et al. 1999). In addition, the transmural extent of myocardial delayed hyperenhancement with gadolinium has been shown to be significantly related to the likelihood of improvement in contractility after revascularisation (Kim et al. 2000). The likelihood of functional improvement in regions with no hyperenhancement was 100%, while 90% of regions with hyperenhancement of 50 to 75% of tissue before revascularisation did not improve post-revascularisation (Kim et al. 2000).

Normal myocardial tissue volume is predominantly intracellular. Gadolinium is a biologically inert tracer that freely distributes in extracellular water, but is unable to cross the intact cell membrane. Expansion of extracellular space in the myocardium can be caused by fibrosis, protein infiltration and myocardial disarray, which result in a combination of increased volume of distribution and slower washout kinetics. Thus, there is a relative accumulation of gadolinium in comparison with the normal myocardium which can be detected in the late phase (Kim et al. 1996; Moon et al. 2004). Gadolinium shortens the longitudinal relaxation time (T1) and T1 is shortened more in infarcted regions than in normal myocardium.

1. 2. 5. 2. CMR sequences in viability assessment

Contrast-enhanced images are acquired with inversion-recovery segmented gradient echo sequences after the administration of a gadolinium-based contrast (0.1 to 0.2

mmol/kg). Images are acquired 10 minutes after the administration of contrast. The inversion time (TI) is the time in milliseconds between the application of the 180-degree prepulse and acquisition of signal at the centre of the k-space. The optimal inversion time is the time at which myocardial tissue signal magnetisation signal is equal to zero or “nulled” and the blood signal in the cardiac chambers in hyperintense. TI ranges from 140 ms to 300 ms. Areas of myocardial infarction appear hyperintense or “bright” due to the higher concentration of gadolinium in the infarcted region, which causes rapid T1 relaxation. A short-axis image stack and long-axis views are acquired to cover the left ventricle from base to apex.

1. 2. 5. 3. Clinical Application

The differentiation of an underlying cause for LV dysfunction has important management and prognostic implications (Bart et al. 1997). Patients with an ischaemic cause may benefit from revascularisation. In the non-ischaemic group, secondary causes including alcohol, infective and inherited abnormalities need to be excluded. Some patients with non-ischaemic cardiomyopathy may benefit from implantable cardiovertor-defibrillators and biventricular pacemakers and identifying those who may benefit would be important.

CMR is potentially able to distinguish LV dysfunction that is related to coronary artery disease or idiopathic dilated cardiomyopathy. In one study of patients with unobstructed coronary arteries on coronary angiogram and dilated hearts, 60% of patients had no gadolinium enhancement, but the remainder had gadolinium enhancement in 2 distinct patterns of subendocardial enhancement similar to ischaemic aetiology and mid-wall striae or patchy enhancement (McCrohon et al. 2003). The possibilities for the pattern of subendocardial enhancement include prior

infarction but with recanalisation after an occlusive event or embolization from minimally stenotic but unstable plaque.

Preliminary data also show that contrast-enhanced CMR has prognostic significance in patients without known myocardial infarction (Kwong et al. 2006). In this study, late gadolinium enhancement involving even a small amount of myocardium was the most important independent predictor of major cardiac adverse events over other clinical predictors in a group of 195 patients with suspected coronary artery disease referred for a clinical CMR examination. In addition, late gadolinium enhancement provided complementary and incremental prognostic value beyond clinical predictors alone or combined with angiographic or LV function predictors (Kwong et al. 2006). Thus contrast-enhanced CMR may improve the current risk assessment of patients who present with possible coronary artery disease.

Late gadolinium enhancement of the myocardium has been shown to be not only due to myocardial infarction, but has been shown to be a marker of myocardial fibrosis of any aetiology. In acute myocarditis, late gadolinium enhancement has been noted in the basal lateral wall in the mid-wall and epicardium (Mahrholdt et al. 2004; Mahrholdt et al. 2006). In hypertrophic cardiomyopathy, late gadolinium enhancement is particularly noted at the right ventricular insertion site, which is a common site of interstitial fibrosis. Infiltrative cardiomyopathies such as amyloidosis and sarcoidosis also show distinct patterns of late gadolinium enhancement (Maceira et al. 2005; Smedema et al. 2005).

1. 2. 6. CMR in Congenital Heart Disease

The value of CMR in the assessment of congenital heart disease (CHD) was first recognised over 20 years ago (Didier et al. 1986; Higgins et al. 1984). The ability of CMR to image in arbitrary planes complemented by three-dimensional angiography allows it to obtain superior anatomic and functional data. CMR has become the gold standard for imaging in certain areas of congenital heart disease, replacing cardiac catherisation as the modality of choice for anatomic and functional characterisation of congenital heart disease when echocardiographic imaging is inadequate (Wood 2006).

1. 2. 6. 1. Defining anatomy in Congenital Heart Disease

The anatomy in congenital heart disease can range from simple to complex and may be pre- or post-operative. In complex congenital heart disease, defining morphology of the atria and ventricles is crucial and requires a systematic examination of the atria, atrioventricular connections, ventricles, ventriculoarterial connections as well as conduits and baffles. Although echocardiography may provide this information, in the adult population in particular, poor acoustic windows because of body habitus or interposition of scar or lung tissue may limit adequate images (Hirsch et al. 1994; Hoppe et al. 1996). CMR can acquire images in multiple and complex planes and is not affected by artefacts from calcification or surgical patch materials in the post-operative patient.

A CMR study in a patient with CHD includes contiguous axial images (in horizontal, coronal and sagittal views) that provide initial information about morphology and allows further detailed images in regions of interest to be acquired. In addition, serial cine images are acquired to provide comprehensive information about congenital

anatomy. The use of diagnostic catheterisation use may potentially be reduced if information can be obtained with non-invasive imaging such as MRI, which provides information about function and physiology in addition to anatomy.

Currently, CMR already has clinical applications in the assessment of great artery anatomy (aorta and pulmonary arteries), venous connections (systemic and pulmonary veins), extracardiac conduits and baffles, intracardiac shunts (e.g. atrial and ventricular septal defects) and in the assessment of complex congenital heart disease

1. 2. 6. 2. Defining function and physiology in Congenital Heart Disease

CMR can provide information on the ventricle such as ventricular volumes, ventricular mass, stoke volume and ejection fraction and is now established as the gold standard technique for the assessment of RV volume, mass and function (Katz et al. 1993; Longmore et al. 1985). Other imaging modalities such as echocardiography and angiography are able to provide this information, however as CMR does not rely on geometric assumptions, even abnormally shaped ventricles can be assessed for volume and function. In particular, the assessment of the right ventricle is important in congenital heart disease, where it may be a subpulmonary RV and support the pulmonary circulation or may be a systemic RV and support the systemic circulation. While the left ventricle has a conical shape with its wall thickness three to four times greater than the RV free wall and with fine trabeculations, the right ventricle is of a complex shape, has coarse trabeculations and a muscular RV outflow tract (Davlouros et al. 2006).

1. 2. 6. 3. CMR pulse sequences in Congenital Heart Disease

Black Blood Imaging

In “black blood” imaging with fast spin-echo sequences, blood appears black while myocardium and blood vessel walls are signal-rich and appear bright. Black blood images have high signal-to-noise ratio, resolution and contrast. These sequences are useful for defining anatomy, characterising abdominal situs and characterising soft tissue detail (Geva et al. 1994). Images can be obtained with both T1- and T2-weighted spin-echo sequences, as well as using Half Fourier Acquired Turbo Spin Echo (HASTE) sequences. HASTE sequences are useful for obtaining axial, coronal and sagittal images from the level of the aortic arch to the diaphragm to provide initial assessment of anatomy.

White Blood Imaging

Gradient echo or “white blood” sequences are useful for the assessment of cardiac function. The older sequences using spoilt gradient echo techniques have the advantages of flow sensitivity. Flowing blood carries non-saturated spins and appears bright, while blood accelerated to the point of turbulence, such as with obstruction, causes signal voids. These sequences are useful for characterising the severity of valvular and vascular stenoses, but is limited by its relative poor image contrast and low signal-to-noise ratio (Wood 2006)

Steady state free precessing (SSFP) imaging, a newer gradient echo sequence relies on contrast between the blood pool and the myocardium for delineation of anatomy. Blood is signal rich, while the myocardium and blood vessel walls have less signal. Cine SSFP imaging provides information about cardiac morphology and function. It

is also useful to image specific areas of interest in congenital heart disease such as shunts, valves, pulmonary vessels and the aorta.

Velocity-encoded cine-MR imaging

This is a flow-sensitive cine-MRI technique that is based on the principle that the phase of flowing spins relative to stationary spins along a magnetic gradient changes in direct proportion to the velocity of flow (Didier et al. 1999). This allows the quantification of blood flow velocity and volume flow in cardiac chambers and great vessels. Two sets of images are usually acquired simultaneously (one with and one without velocity encoding) and the subtraction of the two images allows the calculation of a phase shift which is proportional of flow. Images are then reconstructed in magnitude, providing anatomical information and in phase, providing velocity information (Didier et al. 1999). Velocity can be encoded in planes perpendicular ("through-plane" velocity measurement) or parallel ("in-plane" velocity measurement) to the direction of flow. This technique has been validated for the measurement of aortic and pulmonary flow representing left and right ventricular stroke volumes (Kondo et al. 1991), thus allowing quantification of left-to-right shunts (Hundley et al. 1995), quantitative assessment of valvular regurgitation and the peak flow velocity in valvular stenosis (Kilner et al. 1991; Kilner et al. 1993).

Gadolinium-enhanced MR Angiography

The accurate diagnosis of vascular anomalies in congenital heart disease is important for both prognosis and management (Herlong et al. 2000). Contrast-enhanced MR angiography is non-invasive and provides information about vascular anatomy of the aorta, pulmonary vessels and collateral vessels including major aortopulmonary collaterals (Ferrari et al. 2001; Prasad et al. 2004). Multiple cross-sectional images

can be obtained with a single breath-hold and the images can be reconstructed off-line to obtain images similar to conventional angiography, which can be viewed in multiple planes.

1. 2. 6. 4. Clinical applications for CMR in Congenital Heart Disease

In summary, using a combination of the above techniques and sequences available, anatomical, functional and physiological assessment is currently possible and provides a comprehensive examination of the patient with congenital heart disease. Current major indications for CMR in congenital heart disease include segmental description of cardiac morphology, thoracic aortic assessment, detection and quantification of shunts, stenoses and regurgitation, detection of complex anomalies, pulmonary and systemic venous anomalies in addition to post-operative assessment in adult patients.

1. 2. 7. CMR assessment of atherosclerosis

Cardiovascular disease due to the complications of atherosclerosis is the leading cause of mortality and morbidity in the Western world. This is related to the acute coronary syndromes such as acute myocardial infarction, unstable angina pectoris and sudden cardiac death. It is a diffuse condition and affects not only the coronary arteries, but also the carotid arteries, aorta and peripheral arteries.

The pathogenesis of the acute coronary syndrome is atherosclerotic plaque disruption and subsequent thrombosis (Falk et al. 1995). This is determined by the atherosclerotic plaque composition rather than the degree of arterial stenosis with the majority of acute coronary events occurring with a non-critically stenosed

atherosclerotic lesion (Falk et al. 1995). Pathological features of plaque vulnerability are a large lipid-rich necrotic core and a thin overlying fibrous cap as well as inflammation (Burke et al. 2001; Virmani et al. 2000). Despite much progress in diagnostic investigations to assess atherosclerotic disease, we are still extremely limited in our ability to accurately identify patients at risk for an acute cardiovascular event. Improved prediction of such high-risk asymptomatic individuals is important as these patients would potentially benefit from treatments such as anti-platelet, lipid-lowering or anti-hypertensive therapies in addition to aggressive lifestyle modification.

The current assessment of a patient's cardiovascular risks include assessment of risk factors such as diabetes, smoking, family history of cardiovascular disease, hypercholesterolaemia and hypertension. However, these risk factors by themselves are variable in their ability to predict acute cardiovascular and cerebrovascular events and death (Brindle et al. 2006; Law et al. 2004). Absolute risk assessment is based on equations that have been derived from several cohort studies and randomised trials (Anderson et al. 1991; Assmann et al. 2002; Conroy et al. 2003; Wilson et al. 1998) especially those derived from prospective follow-up of individuals from the Framingham Heart Study (Anderson et al. 1991).

In addition to risk factors, investigations with imaging of coronary artery disease and assessment of serological markers are potentially important in patient cardiovascular risk assessment. Coronary angiography, currently the gold standard investigation for the detection of coronary atherosclerotic disease, provides information on lumen stenotic severity but little information on atherosclerotic plaque composition. Non-invasive imaging modalities such as carotid intima media thickness (IMT) measured

by ultrasound techniques have been used as a surrogate marker of atherosclerosis (Bots et al. 1997; Chambless et al. 1997; Salonen and Salonen 1993). While carotid IMT may predict future cardiovascular and cerebrovascular events, it has limitations including heterogeneity of ultrasound protocols and low specificity of IMT location for a clinical event (Lorenz et al. 2007). An imaging modality that is able to visualise and quantify atherosclerotic plaque would enable us to identify the vulnerable atherosclerotic lesion. High-resolution magnetic resonance imaging (MRI) has been shown to both quantify and characterise non-invasively atherosclerotic components in both human and animals. In addition, there is the potential to monitor the regression of atherosclerotic plaque with therapy such as with lipid-lowering treatments (Worthley et al. 2000).

1. 2. 7. 1. Atherosclerotic plaque components with MR imaging

Atherosclerotic plaque disruption is the most frequent underlying cause of the onset of acute thromboembolic cardiovascular and cerebrovascular events such as myocardial infarction, unstable angina, cerebrovascular accidents and transient ischaemic attacks (Falk et al. 1995). Clinical risk factors for atherosclerosis help to predict risk of these events and angiography provides information about the degree of obstruction to flow in coronary and carotid vessels, but does not provide information to identify patients with atherosclerotic plaques that are vulnerable to disruption.

The majority of acute coronary events involve non-critically stenosed atherosclerotic lesions that are undetected by conventional stress testing and imaging techniques. Atherosclerotic plaque composition rather than stenotic severity predicts the risk of plaque rupture and its thrombogenicity (Fernandez-Ortiz et al. 1994; Fuster et al.

1992; Fuster et al. 1992; Ross 1999). A vulnerable atherosclerotic plaque that is at high risk of rupture has a thin fibrous cap and a large lipid-rich necrotic core. Plaques containing large atheromatous cores are more prone to disruption and are responsible for the atherothrombotic complications leading to acute coronary syndromes (Falk et al. 1995).

Imaging modalities that can characterise atherosclerotic plaque and its components may allow risk stratification in both asymptomatic and symptomatic patients with coronary artery disease and potentially enable appropriate selection of therapies to reduce this risk (Worthley et al. 2000). The ideal imaging modality would be one that is safe, non-invasive, accurate and reproducible allowing longitudinal studies in the same patient (Celermajer 1998). High-resolution MRI has emerged as the potential leading non-invasive modality to differentiate plaque components. Of the imaging modalities, it has the greatest soft tissue contrast that is able to accurately identify plaque tissue components with sub-millimetre resolution (Shinnar et al. 1999; Toussaint et al. 1996; Worthley et al. 2000; Yuan et al. 1998). Furthermore, MRI does not use ionising radiation and allows the free choice of tomographic planes. Recent technical developments in MRI technology such as dedicated surface coils, the introduction of high-field systems and developments in the field of molecular imaging such as contrast agents targeted to specific plaques constituents will potentially lead to further improvements in signal to noise ratio, spatial resolution and imaging speed. Its limitations include relatively long imaging time, isolation of the patient from medical care during image acquisition and contraindication in patients with some metallic implants.

Plaque components are differentiated with MRI based on biophysical and biochemical parameters of chemical composition, water content, physical state, molecular motion or diffusion (Fuster et al. 2005). *In vivo* and *ex vivo* MRI has been shown to be able to differentiate lipid core, fibrous cap, calcifications, intraplaque haemorrhage, normal intima and adventitia *in vivo* in human atherosclerotic plaques (Coombs et al. 2001; Serfaty et al. 2001; Shinnar et al. 1999; Yuan et al. 2001). MRI is thus a potential tool not only for assessing atherosclerotic lesions, but also for the serial assessment of lesion progression or regression following lipid-lowering therapy (Corti et al. 2002). In addition, MRI has the potential to provide information about cardiac anatomy, function, perfusion and metabolism.

The proton density of water determines signal intensity in MRI images and MR images can be weighted to T1, T2 or proton density values through manipulation of the MR parameters. In a T1-weighted image, tissues with low T1 values will be displayed with high signal intensity, while high T1 values will be displayed with low signal intensity. In T2-weighted images, tissues with high T2 values will be of high signal intensity while those of low T2 values will be of low signal intensity. In a proton density-weighted image, the differences in contrast are proportional to the density of water and fat protons within the tissue (Worthley and Badimon 2005).

In atherosclerotic plaque, fibrous tissues consist mainly of extracellular matrix elaborated by smooth muscle and are associated with a short T1. Plaque lipids consist mainly of unesterified cholesterol and cholesteryl esters and are associated with a short T2 (Toussaint et al. 1995) Perivascular fat is composed mainly of triglycerides and appears different from atherosclerotic plaque lipids on MRI (Toussaint et al. 1996; Toussaint et al. 1995).

Calcified tissue has low signal intensity on both T2 and T1-weighted sequences due to low water proton content. Fibrocellular tissue and thrombus may also be dark on proton density weighted images. In T2-weighted sequences, atheromatous core has low signal intensity relative to the fibrous cap and outer layers of the vessel wall. Intraplaque haemorrhage is bright on T1-weighted images due to the presence of methaemoglobin, a breakdown product of haemoglobin. Methaemoglobin causes a shortening of T1 and hence an increase in signal intensity on T1-weighted images (Toussaint et al. 1996).

MRI Signal Intensity

Imaging Sequence	Dense fibrocellular	Lipid Rich	Haematoma	Calcification
PDW	High	Intermediate	Intermediate	Nil
T1W	High	Intermediate	High	Nil
T2W	High	Low	Low	Nil

Used with permission Atherosclerosis 2000 Table 1 (Worthley et al. 2000)

1. 2. 7. 2. MR imaging of coronary arteries

MRI of the coronary arteries is technically more challenging compared to carotid and aortic artery imaging due to cardiac and respiratory motion artefacts, the smaller size of the coronary arteries and its curvilinear course (van der Wall et al. 1995). Bright blood non contrast-enhanced MR coronary angiography is unable to provide information about the coronary wall structure of atherosclerotic plaque characteristics. In black blood MRI, the signal from static tissue is maximised and the transverse magnetization of flowing blood is made incoherent resulting in blood signal void (Fayad et al. 2000).

High resolution *in vivo* coronary MRI was first validated using a clinical 1.5T system in a porcine model where coronary lesions were induced by balloon angioplasty and black blood in vivo images of the coronary artery wall and lesions were obtained with a double-inversion-recovery fast-spin-echo sequence (Worthley et al. 2000).

In an *ex vivo* setting in porcine coronary arteries and aortas, complex atherosclerotic lesions including calcified, lipid-rich, fibrocellular and haemorrhagic regions can be accurately characterised (Worthley et al. 2000). Dense fibrocellular areas had high signal intensity on all 3 imaging sequences (T1, T2 and PDW), lipid-rich areas were of intermediate signal intensity on PDW and T1W sequences but low signal intensity on T2W sequences, while calcification produced signal loss on all 3 sequences due to the low mobile proton density within the calcified area (Worthley et al. 2000). Plaque haematoma was less accurately identified. Mean vessel wall thickness measurements were approximately 10-20% larger with MR imaging than by histopathology. This was attributed to specimen shrinkage during paraffin embedding for histopathology analysis and volume averaging due to MR images being significantly thicker than the histopathology sections.

In humans, high resolution black blood MRI of both normal and atherosclerotic coronary arteries has been performed for direct assessment of coronary wall thickness and visualisation of atherosclerotic plaque in the wall (Fayad et al. 2000).

1. 2. 7. 3. MRI studies of carotid artery atherosclerosis

The superficial location and relative absence of motion of the carotid arteries allow imaging and characterisation of its walls, fibrous cap (Toussaint et al. 1996; Yuan et al. 2001) and quantification of atherosclerotic plaque size (Corti et al. 2001).

MRI can characterise the composition of human carotid atherosclerotic plaque including fibrous tissue, lipid and necrotic core, calcium, haemorrhage, thrombus and the fibrous cap *in vivo* and *ex vivo* (Cai et al. 2002; Hatsukami et al. 2000; Shinnar et al. 1999; Toussaint et al. 1996; Yuan et al. 2001).

The characterisation of carotid plaque composition *ex vivo* with high-field MRI has been shown to have a high level of sensitivity and specificity (Shinnar et al. 1999). Identification of calcium, fibrocellular, lipid and fibrous cap components had sensitivity of 100% while the lowest sensitivity was with thrombus identification (Shinnar et al. 1999). Using diffusion-weighted MRI, thrombus appears as a bright area in diffusion-weighted images, however if thrombus was adjacent to areas of calcification, the signal obtained has been shown to be so low that it may not appear bright and thus difficult to identify (Shinnar et al. 1999). In addition, acute thrombus may not have the characteristic bright appearance on diffusion-weighted images (Toussaint et al. 1996). Fibrocellular tissue and thrombus may appear dark on proton density images, and T2-weighted images and these components may appear darker than their T2 would suggest (Shinnar et al. 1999).

The fibrous cap is an important structure for the stability of the atherosclerotic plaque. An intact thick fibrous cap can be distinguished from an intact, thin and ruptured cap using high resolution MRI with a 3D time-of flight protocol.

(Hatsukami et al. 2000; Yuan et al. 2001). A thin fibrous cap or ruptured fibrous cap in human carotid atherosclerotic plaque on MRI has been shown to be highly associated with a recent history of transient ischaemic attack or stroke (Yuan et al. 2002). Compared with patients with thick fibrous caps, patients with thin fibrous caps were 10 times more likely to have had a recent TIA or stroke (Yuan et al. 2002). *In vivo* multicontrast MRI is able to further classify human carotid atherosclerotic lesions as early, intermediate or advanced lesions according to the AHA classification (Cai et al. 2002) and with a high degree of reproducibility (Chu et al. 2004).

Multicontrast MRI has been shown to accurately detect the presence and age of the carotid intraplaque haemorrhage (Chu et al. 2004). Acute intraplaque haemorrhage appears as a hyperintense signal on T1 weighted and TOF images and as an isointense signal on PD/T2W images while subacute haemorrhage appears as a hyperintense signal on all four contrast weightings. Intraplaque haemorrhage has been found to be associated with greater progression in both lipid-rich necrotic core and plaque volume in a serial high-resolution MRI study on asymptomatic patients with carotid stenosis (Takaya et al. 2005).

The use of gadolinium based, contrast-enhanced MRI have shown that post-contrast T1-weighted MR images help to discriminate the fibrous cap from the necrotic core (Cai et al. 2005; Wasserman et al. 2002; Yuan et al. 2002). The contrast agents are known to distribute into the extracellular fluid space and cause a greater degree of enhancement in the vessel wall and fibrous cap which may be due to increased permeability, increased extracellular volume or decreased washout (Wasserman et al. 2002).

1. 3. CARDIAC COMPUTED TOMOGRAPHY

1. 3. 1. Background

Multidetector computed tomography (MDCT) has been used in clinical settings to measure of the amount of calcification in the coronary arteries with coronary artery calcium scoring of the coronary tree, a surrogate marker of atherosclerosis. MDCT has also become the gold standard for angiographic imaging in most arterial beds such as the carotid and peripheral vascular systems. In the coronary arteries, there have been major advances in the accuracy of coronary MDCT angiography, particularly with regards to its negative predictive value, although excessive calcification and blooming artefacts still limit the diagnostic accuracy of the technique for assessing stenotic severity.

1. 3. 2. MDCT Basics

Improvements in CT systems in recent years have resulted in faster rotation speed of the gantry and thin slice collimation. This has led to substantial improvements in spatial and temporal resolution, with shortened acquisition time achieved in one breath hold. Electron-beam computed tomography (EBCT) uses a rotating electron beam and non-mechanical movement of the X-ray source to acquire triggered tomographic X-ray images over 100 milliseconds at 3 mm intervals with a 30 second breath-hold. Multidetector computed tomography (MDCT) uses a rotating gantry with motion of the X-ray source and table, combined with multiple detectors (from 4 to 64) to acquire the data in spiral or helical fashion.

Multidetector spiral CT systems with simultaneous acquisition by 4 detector rows and a minimum rotation of 500 msec were introduced in 1998. Increasing the number of sections that are simultaneously acquired have led to further improvement with fast high-resolution volume coverage that has resulted in the introduction of eight, 10, 16, 32, 40 and 64-detector row CT scanners with further reduced gantry rotation times and minimum beam collimation widths of less than 1 mm (Schoepf et al. 2004).

Motion artefacts caused by cardiac pulsation is minimised by acquiring or reconstructing data at a time point with the least cardiac motion, usually in the diastolic phase of the heart cycle (Schoepf et al. 2004). Prospective triggering has been used in electron beam CT and single-detector row spiral CT where a trigger signal is derived from the patient's ECG on the basis of the prospective estimation of the present R-R interval. The scan is started at a defined time point after a detected R wave, usually during diastole (Schoepf et al. 2004). With retrospective ECG gating, scan data is acquired and available for the entire phase of the cardiac cycle, although the scan data used for image reconstruction is selected during the diastolic phase. A stack of images is reconstructed at every heartbeat, which enables faster coverage than prospectively ECG-triggered multi-detector row CT scanning. Reconstruction of image stacks at exactly the same phase of the heart cycle enables continuous and phase-consistent coverage of the entire heart and adjacent anatomy in the selected scanning range (Becker et al. 2000; Schoepf et al. 2004).

The effective radiation dose of 1mSv has been reported for routine scanner settings and prospectively ECG-triggered acquisitions (e.g. in calcium scoring) with EBCT (3 mm beam collimation) and four-detector row CT (2.5 mm beam collimation).

With retrospectively ECG-gated imaging of the heart, there is relatively high radiation exposure due to continuous X-ray exposure and overlapping data acquisition (Morin et al. 2003). For high spatial resolution (1.00-1.25 mm beam collimation), a retrospectively ECG-gated acquisition (e.g. in contrast CT of the heart) with four-detector row CT, there is an exposure limit of approximately 10 mSv applied which is comparable to a routine diagnostic conventional coronary angiographic examination (Schoepf et al. 2004). This dose can be reduced to approximately 5 to 7 mSv with ECG-gated dose modulation where the nominal tube output is applied only during the diastolic phase of the cardiac cycle, where most images are likely to be reconstructed and for the rest of the cardiac cycle, the tube output is reduced.

1. 3. 3. Coronary artery calcification

1. 3. 3. 1. Pathophysiology

Atherosclerotic calcification begins as early as the second decade of life, just after fatty streak formation (Stary 2001; Stary et al. 1995). Calcific deposits are found more frequently and in greater amounts in elderly individuals and in more advanced lesions. In one autopsy study of patients over 60 years of age, 94% of coronary arteries had some degree of calcification (McCarthy and Palmer 1974). It has been suggested that coronary calcium is seen exclusively in atherosclerotic arteries, but is absent in normal vessel wall (Fitzpatrick et al. 1994; Stary et al. 1995).

The mechanisms for the formation of atherosclerotic calcification are poorly understood, however, pathologic calcification of atherosclerotic vessels shares features with normal bone such as cellular proliferation, matrix deposition and

calcification. The principal collagen found in atherosclerotic plaques is Type I collagen which is associated with bone formation (Burleigh et al. 1992). There is evidence that mineral deposits in arterial plaques consist of calcium hydroxyapatite which is the major inorganic component of bone (Bostrom et al. 1993). This formation of calcium hydroxyapatite is an active process regulated by calcifying vascular cells or associated with smooth muscle cell or macrophage production of ectopic bone matrix proteins (Bostrom et al. 1993)

The relation of arterial calcification to the probability of plaque rupture is unknown (Falk et al. 1995). Vulnerable plaque is frequently present in the absence of calcification (Davies et al. 1993) and although coronary artery calcium may provide a measure of total plaque burden, calcium does not concentrate only at sites with severe coronary artery stenosis (Wexler et al. 1996). There are histopathologic reports of small numbers of patients which have suggested that ruptured plaques are less likely to be calcified (Cheng et al. 1993; Gertz and Roberts 1990; Wexler et al. 1996). *In vivo* evidence of the relative stability of calcified lesions has been obtained with intravascular ultrasound in larger studies (Mintz et al. 1997; Mintz et al. 1995). The presence and magnitude of target lesion calcium paralleled the atherosclerotic plaque burden as assessed by IVUS, but the presence and magnitude of target lesion calcium did not parallel the extent of lumen compromise as assessed by coronary angiography (Mintz et al. 1997). In the same study, intermediate lesions had as much target lesion calcium as did severe lesions and the only clinical risk factors for coronary calcification were patient age and non-insulin dependent diabetes. However when controlled for patient age, non-insulin dependent diabetes was not an independent predictor (Mintz et al. 1997). Insulin-dependent diabetic patients were

less likely to have coronary calcification than either non-diabetic or non insulin-dependent diabetic patients (Mintz et al. 1997; Tuzcu et al. 1996).

1. 3. 3. 2. Coronary artery calcium estimation with CT

Coronary artery calcification is potentially detectable by plain film roentgenography, coronary arteriography, fluoroscopy, computed tomography (electron beam and multidetector CT) and intravascular ultrasound. Although fluoroscopy can detect moderate to large calcifications, its ability to identify small calcific deposits is low compared to CT and it is not able to quantify calcification (Wexler et al. 1996).

As calcium attenuates the X-ray beam, computed tomography is highly sensitive in detecting vascular calcification and CT distinguishes mural calcium because of its high CT density relative to blood. Earlier published studies utilised EBCT for quantification of coronary artery calcium which demonstrated high correlation coronary artery calcium on EBCT with histopathology (Rumberger et al. 1995) and intravascular ultrasound (Baumgart et al. 1997; Schmermund et al. 1997). Average whole coronary system calcium area as measured by EBCT defines on average only approximately 20% of the total atherosclerotic plaque present at histological examination (Rumberger et al. 1995). There were also arteries that had demonstrable atherosclerotic plaque but little or no associated coronary calcium. For plaque areas $< 1mm^2$, the EBCT coronary calcium areas were nearly zero, for plaque areas 1 to 5 mm^2, the mean calcium area was 0.46 mm^2 and only when coronary plaque areas were consistently in the range of 5 to 10 mm^2 per segment were the corresponding coronary calcium areas $> 1mm^2$ (Rumberger et al. 1995). This minimal calcium area of 1 mm^2 may be too small for consistently reproducible results as with a standard 512 by 512 matrix, pixel areas are 0.34 mm^2 and with the criterion of two contiguous

pixels with CT density of > 130 HU, pixel areas are 0.68 mm^2 (Rumberger et al. 1995). This has important implications as only calcifications associated with larger atherosclerotic plaques (>5mm^2) are detected while smaller segmental areas are not reliably detected.

Although EBCT has a faster temporal resolution than MDCT, both modalities have a good agreement for estimation of coronary artery calcium scoring (Becker et al. 2001; Knez et al. 2002). Coronary calcification has traditionally been assessed by means of a score introduced by Agatston, measured in Hounsfield units (Agatston et al. 1990; Janowitz et al. 1993; Rumberger et al. 1995). The Agatston score calculates the calcium burden by multiplying the area of the calcified lesion by a weighting factor dependent on the peak signal of the lesion (Agatston et al. 1990). An area of threshold of ≥1mm^2 and a density threshold of > 130 Hounsfield units are used to identify a calcified lesion. Histological studies support the association of tissue densities of 130 Hounsfield units with calcified plaques (Wexler et al. 1996). Individual scores are separately accumulated for the left main, left anterior descending, left circumflex and right coronary artery with a total score obtained from the sum of these scores. However, the Agatston score is limited by the low (17% interscan variability) reproducibility (Wang et al. 1996) and newer methods which measure calcium volume (Callister et al. 1998; Hong et al. 2002) have shown improved reproducibility (13% interscan variability).

1. 3. 3. 3. Clinical Implications of Coronary Artery Calcification

Coronary artery calcification is almost invariably present only if atherosclerotic disease is present in the coronary circulation (Burke et al. 2003; Rumberger et al. 1995). It is closely related to ageing, a major factor increasing the risk of

atherosclerosis. Coronary calcification has been shown to be a good predictor for the burden of atherosclerotic disease, however there is some contention about the role of calcification in its relation to instability of atherosclerotic plaque rupture and subsequent thrombosis. Coronary calcification does not necessarily indicate significant obstructive disease (Stary 2001) and there is only a weak, nonlinear correlation between the amount of coronary calcium and the angiographic severity of obstructive coronary artery disease (O'Rourke et al. 2000). Pathological (Beckman et al. 2001; Burke et al. 2000; Huang et al. 2001) and imaging (Nikolaou et al. 2004) data have shown that the actual sites of coronary artery calcification do not co-locate with culprit coronary lesions associated with myocardial infarction. However, coronary artery calcification remains a strong predictor for revascularisation (coronary artery bypass grafting and angioplasty) rather than “hard” cardiovascular events of death and non-fatal myocardial infarction (Kondos et al. 2003).

In asymptomatic individuals, there are large and consistent observational studies that have shown that coronary artery calcium scoring with EBCT is a predictor for cardiovascular events (Arad et al. 2000; Budoff et al. 2007; Greenland et al. 2004; Kondos et al. 2003; Shaw et al. 2003; Wong et al. 2002) and provided incremental information over that provided by conventional risk factor analysis (Shaw et al. 2003). In study of over 1000 asymptomatic subjects who were predominantly moderate to high risk, coronary artery calcium scores of >300 significantly added prognostic information to Framingham risk analysis in the 10 to 20% 10-year Framingham risk category (Greenland et al. 2004). In addition, in a recent observational study of the largest follow-up of >25000 middle-aged asymptomatic subjects, coronary artery calcium score was shown to predict all-cause mortality (Budoff et al. 2007) and these are consistent with the findings of a previous study

(Shaw et al. 2003). Given its independent risk prediction, the role of coronary artery calcium screening would most likely benefit individuals who are at intermediate risk for coronary events i.e. those with 0.5 to 2.0% annual event rate based on traditional risk factor analysis.

The role of coronary artery calcium to monitor atherosclerotic disease has not been demonstrated. Randomised double-blind trials with lipid-lowering therapy have not showed slowing of coronary artery calcium progression with atorvastatin 20 mg (Arad et al. 2005) and atorvastatin 80 mg versus pravastatin 40 mg (Raggi et al. 2005) in asymptomatic patients.

1. 3. 4. Computed Tomography Coronary Angiography

While invasive coronary angiography is the gold standard in coronary artery imaging, it carries a small, but defined risk of both major and minor complications. The major risk of complication reported by the largest described series from the Society of Cardiac Angiography and Intervention is 1.7% including vascular, haemodynamic, arrhythmic and renal complications (Noto et al. 1991). Coronary arteries because of their small dimensions and motion have been difficult to image by computed tomography (CT). Typically, the luminal diameter of coronary vessels tapers down from 5 mm in the left main coronary artery to 1 mm in the distal left anterior descending coronary artery (Funabashi et al. 2003). Image acquisition of the coronary arteries requires a high temporal resolution, which with CT (50 to 300 msec) is lower than that of conventional angiography (<10 msec) (Schoenhagen et al. 2004) and a high spatial resolution. Electron beam CT (EBCT) uses a rapidly rotating electron beam, which is reflected onto and a stationary tungsten target. EBCT can achieve temporal resolutions of 50 to 100 msec per slice and was used

initially to detect and quantify coronary artery calcification (Agatston et al. 1990). Images with EBCT are usually obtained with 3 mm thickness during one breath hold. Improvement in multi-detector CT (MDCT) technology from the combination of faster rotation time and multi-detector row acquisition with sub-millimetre spatial resolution have increased the ability to visualise the coronary lumen. While 16 slice MDCT acquires 16 parallel projections within a single rotation (420 msec per rotation with 210 msec temporal resolution) and thinner image sections (0.75 mm)(Schoenhagen et al. 2004), new MDCT scanners with 64 slices have further improved spatial resolution (Wintersperger and Nikolaou 2005). Image sections can now be obtained in the range of 0.5 to 0.625 mm at a maximum gantry rotation speed of 330ms/360° for the 64-slice scanners which allows for a higher temporal resolution further improving both functional assessment of the heart and image quality at various heart rates (Wintersperger and Nikolaou 2005).

MDCT angiography has been shown in expert centres and selected patients to have a consistently very high negative predictive value (98%) and positive predictive value (80%) for the detection of coronary stenoses (Kuettner et al. 2004; Leschka et al. 2005; Mollet et al. 2005; Morgan-Hughes et al. 2005; Nieman et al. 2002; Ropers et al. 2003). In these studies, however, patient with renal failure and arrhythmias were excluded and analysis was limited to coronary segment diameter of greater than 1.5 to 2.0 mm. Coronary venous bypass grafts are larger than native coronary arteries and MDCT has been shown to accurately document coronary artery bypass graft patency (Nieman et al. 2003; Pache et al. 2006; Schlosser et al. 2004).

A regular and low heart rate significantly improves the image quality, arteries accessibility and accuracy for stenosis detection (Giesler et al. 2002; Hoffmann et al.

2005; Schroeder et al. 2002) for imaging of the coronary arteries with CT. Patients in atrial fibrillation or with other arrhythmias cannot be studied adequately. Motion can lead to artefacts with the right coronary artery most frequently affected. Severe calcifications of the coronary artery cause partial volume artefacts and the apparent volume of areas of calcification is larger on CT. This may obscure the lumen and thus limit accurate quantification of stenosis severity. Quantitative measurement of coronary artery stenosis severity is currently also limited by spatial resolution.

Unlike coronary calcification assessment with CT which does not require contrast administration, to visualise non-calcified plaques, contrast agent administration is required. This makes the investigation not suitable for patients with renal insufficiency and contrast allergy. The patient's heart rate at the time of MDCT has to be slow to reduce motion artefacts and achieve diagnostic image quality, ideally <65 beats per minute and this may require the administration of beta blocker medications (Nieman et al. 2001; Schroeder et al. 2002). Multislice CT investigations are associated with a considerable radiation exposure (between 5 to 9 mSv).

1. 3. 5. Atherosclerotic Plaque Imaging with CT

Atherosclerotic plaque composition is an important predictor of plaque stability with most plaque ruptures occurring in plaques containing a soft lipid-rich core with an overlying thin fibrous cap (Virmani et al. 2000). The detection of calcified and non-calcified plaques in the coronary arteries of patients with suspected coronary arteries has been shown to be feasible with contrast-enhanced multi-detector CT angiography (Becker et al. 2000). Plaques have been divided into calcified (density >130 HU)

while non-calcified lesions are identified on the basis of their lower density (density <130 HU) compared with the contrast-enhanced lumen (Schroeder et al. 2001).

The AHA criteria defines type I and II lesions as early atherosclerotic lesions, type III and IV as intermediate lesions with extracellular lipid pools, type V lesions as fibroatheromas and type VI lesions as complicated lesions with surface defects, haematoma, haemorrhage or thrombus (Stary et al. 1995). An ex vivo MDCT study to characterise atherosclerotic plaque found the CT attenuation in predominantly lipid-rich plaques (type IV and Va) was significantly lower than in predominantly fibrous-rich plaques (Becker et al. 2003). The CT Hounsfield values of lipid and fibrous-rich plaques were 47+/-9 HU for lipid and 104+/-28 HU for fibrous plaques. Compared to the AHA criteria, type III to type VI plaques could be visualised by CT while early stages (type I and II lesions) were not detectable (Becker et al. 2003).

In a coronary artery study of atherosclerotic plaque with MDCT (Schroeder et al. 2001), patients with chronic stable angina and >70% stenosis in proximal segments of the LAD or RCA were scheduled for intra-coronary ultrasound-guided PTCA (Schroeder et al. 2001). Soft plaques showed a mean density of <50 HU, intermediate plaques of 50 to 119 and calcified plaques >120 HU. There was a strong correlation of tissue density measurements within the plaque and the qualitative ultrasound classification of “soft, intermediate and calcified” (Schroeder et al. 2001). A more precise assessment of plaque composition using MDCT by visualizing lipid cores, fibrous caps or calcified is restricted due to limited spatial resolution.

Coronary calcium studies with EBCT have suggested that coronary calcium increases with total atherosclerotic burden. However, it is unclear what stage of

atherosclerosis coronary calcification is a feature of, and whether the presence and amount of calcium can also predict unstable coronary artery disease. There have been a few CT studies looking at the plaque burden in stable versus unstable group of patients with coronary artery disease and have shown a greater plaque burden with calcified plaques in patients with stable angina pectoris compared to patients with acute myocardial infarction (Leber et al. 2003). Furthermore, a third of patients with acute myocardial infarction had moderate calcium scores of <100. In these patients, calcified plaques reflected only 52% of the plaque burden (Leber et al. 2003). In a small group of 5 patients with a clinical presentation of acute myocardial infarction who had near normal coronary angiograms, large coronary soft plaque lesions were found on four-detector MDCT and IVUS and attributed as the cause for the acute myocardial infarction (Caussin et al. 2003). These findings suggest that the severity of coronary atherosclerosis may be underestimated significantly if only calcified plaques are considered surrogate markers for total plaque burden.

Non-calcified coronary plaques can be detected with a sensitivity of 78% with sixteen-detector MDCT when compared to intravascular ultrasound (Leber et al. 2004). However, due to limitations in temporal resolution, the ability to identify non-calcified plaques was found to be restricted to larger advanced lesions with a plaque diameter of at least 1.5 mm located in the proximal and middle coronary segments. Intraplaque haemorrhage may be a marker of plaque instability which is a contributing factor to a more rapid progression of atherosclerosis (Beach et al. 1993). In MDCT images, intraplaque haemorrhage may be visualised as an area of reduced contrast material passage, however, MDCT currently does not reliably detect intraplaque haemorrhage (Saba et al. 2007).

The fibrous cap and its potential rupture has been better visualised using MRI and in particular, the percentage of lipid-rich necrotic core can be quantified (Coombs et al. 2001; Hatsukami et al. 2000; Shinnar et al. 1999; Toussaint et al. 1996). MRI can more easily detect intraplaque haemorrhage and also has the potential to distinguish between acute and non-acute haemorrhage, which may have clinical implications as acute haemorrhages were significantly more likely to be found in patients with symptomatic plaques than in patients with asymptomatic plaques (Saam et al. 2006; Takaya et al. 2006).

1. 4. MICRO COMPUTED TOMOGRAPHY

1. 4. 1. Background

Traditionally, histopathologic analysis of human autopsy specimens and explanted tissue has been the established standard for analysis of human arteries. However, histopathologic analysis is limited as it does not provide three dimensional information, causes loss of the intact volume of the specimen resulting in difficulty of further examination with other methods and in addition, serial sectioning of multiple thin slices from tissue specimen is time-consuming and expensive (Langheinrich et al. 2004).

1. 4. 2. Micro CT Basics

Micro computed tomography (micro CT) is a technique that enables micro CT systems to generate thin-section images of small specimens. The first micro-tomography (micro-CT) scanners were first developed in the 1980s using bench-top X-ray sources (Ritman 2004). A micro-focused x-ray source illuminates the object of

interest, which is positioned on a precision manipulator and a sensitive camera acquires the x-ray images. During image acquisition, the sample is rotated step at a time through 180 degrees with images recorded at each rotation. Using complex software, 2 dimensional images based on x-ray density can be recalculated from the x-ray images and data can be calculated from the morphology of the samples. Rapid acquisition of approximately 10 cross sections per minute can be achieved and with spatial resolution of 5 to 8 μm (Langheinrich et al. 2004).

1. 4. 3. Micro CT application

Earlier studies with micro CT have been of small animal models for bone structural analysis and intact rodent organ vasculature (Feldkamp et al. 1989; Jorgensen et al. 1998; Kuhn et al. 1990; Paigen et al. 1987). Micro CT has been also shown to be a sensitive method to detect vascular calcification in animal models in vivo (Persy et al. 2006). There have been a limited number of human studies to analyse vascular structure and calcification (Clarke et al. 2003; Langheinrich et al. 2004). As calcium is removed during histological processing, micro-CT has been used as the gold standard for identifying calcium deposits within the human carotid *ex vivo* atherosclerotic plaque (Clarke et al. 2003). In an autopsy small study of ten epicardial human coronary arteries, micro CT provided quantitative information about plaque morphology equivalent with histopathological analysis. This was assessed using micro CT grey-scale value differences to classify lesions as fibrous, calcified or lipid-rich plaques (Langheinrich et al. 2004). However, a limitation in this study was that only structures delineated with sufficient contrast material could be visualised and quantified exactly.

Micro CT analysis can be performed prior to histologic processing and thus has the advantages of avoiding artefacts from fixation, dehydration, decalcification and embedding. As it is a non-destructive approach, micro CT potentially allows the analysis of atherosclerotic plaque characteristics such as plaque area, lumen area, calcified areas and lipid core as a continuous and complete dataset of the vessel over its entire length. Micro CT is thus a useful additional tool for the ex vivo assessment of atherosclerosis. There is ongoing work on more detailed classification of plaque types according to grey-scale attenuation (Langheinrich et al. 2007).

1. 5. AIMS OF THE THESIS

In this thesis, our aims were to address some specific novel areas advancing the utility of these imaging modalities in two major areas of interest, namely congenital heart disease and atheroma imaging.

Our first step was to validate the accuracy and reproducibility of CMR, the main imaging modality we utilised. To achieve this, we assessed MR imaging of cardiac volumes and function in a normal adult Australian population with a specific focus on the reproducibility of the technique. In confirming that this technique in our hands is both accurate and reproducible, we would then be in a position to be able to confidently use this technique in our future chapters. However, more than this, we sought to establish some normal ranges for left and right atrial and ventricular parameters in our local population. This would be crucial background information for us to be able to make comparisons with future studies in patients with congenital heart disease.

Having established our technique and reference ranges, we would then explore the two specific issues in the ensuing two chapters using CMR in one area of congenital heart disease, atrial septal defect. Atrial septal defect is the most common congenital heart defect first diagnosed in adults. The traditional method of assessment of these patients and for suitability for ASD closure involves semi-invasive investigation with transoesophageal echocardiography (TOE) for measurement of the defect size and atrial septal margins. MRI assessment of patients prior to percutaneous device closure compared to TOE assessment would provide information on the accuracy of TOE assessment and provide information of the utility of cardiac MRI as an alternative to TOE for the work-up of these patients prior to ASD closure.

In our third original research chapter, we utilised CMR to understand the effects of percutaneous ASD closure on cardiac chamber volumes. We achieved this by assessing with cardiac MRI pre-closure and post-closure atrial and ventricular cardiac volumes. Longstanding right heart dilatation in the setting of an ASD may lead to complications including right heart failure, pulmonary hypertension and arrhythmia. Closure of the ASD should reduce right heart volumes by removing left-to-right shunting and lead to normalisation of ventricular volumes. The assessment of atrial volume changes with ASD closure may be important in furthering our understanding in its contribution to arrhythmia.

Having assessed the ability of CMR to assess both the ASD dimensions, and therefore suitability for percutaneous closure, as well as the effects of ASD closure on cardiac chamber size, we look in the final two original research chapters to move to another area of research development with these high-resolution imaging technologies, atherosclerosis imaging. Two particular areas we wished to focus on

included the potential of high-resolution MR imaging to monitor effects of HDL infusion on atherosclerosis, and secondly to explore mechanisms behind limitations in MDCT imaging of atherosclerosis, specifically calcification and blooming artifacts.

For assessing the effects of HDL infusion on atherosclerosis, we utilised a cholesterol-fed rabbit model of atherosclerosis. The abdominal aorta of the rabbit is comparable in size to the human coronary artery. Previous work with the rabbit model of atherosclerosis and magnetic resonance imaging of the aortic wall has shown that it can provide information about atherosclerotic composition as well as provide serial data of the arterial wall. While high intensity lipid lowering with statins remains the first line management of at risk individuals, modest manipulations of serum HDL levels are associated with a significant impact on cardiovascular risk. Thus, we assessed the effect of HDL infusion and atorvastatin in a rabbit model of using MRI of aortic atherosclerosis as the end-point.

In our fifth and final original research chapter, we assessed the accuracy of quantification of atherosclerotic calcification with MDCT in the carotid arteries of patients undergoing carotid endarterectomy, and sought to identify algorithms or techniques that may improve quantification of calcification. This would potentially lead to an improvement in the ability of MDCT techniques to quantify stenotic severity in coronary arteries that were calcified. To achieve these we utilised MDCT in vivo and in comparison with carotid endarterectomy specimen micro CT. Importantly, as part of this study, we undertook a thorough assessment of reproducibility of these techniques.

Thus, in summary, we have been able to confirm the accuracy and reproducibility of CMR and MDCT in the areas of a specific congenital defect (ASD) and atherosclerosis imaging, and utilised these techniques to advance our understanding of these disease states. This thesis identifies strengths and weaknesses of these techniques that will allow us to more appropriately use them for future purposes in cardiovascular disease. Future work directly stemming from this thesis has already begun, and now looks to address issues of whether CMR and MDCT may provide complimentary information about atherosclerotic lesions that may benefit outcomes in certain conditions. Specifically the work in this thesis has led to studies commencing in carotid atherosclerosis and saphenous vein graft atherosclerosis and using these imaging techniques to potentially predict adverse future outcomes.

Chapter 2

METHODS

TABLE OF CONTENTS

2. 1. STUDY POPULATIONS

2. 1. 1. Normal healthy volunteers

Healthy volunteers with no history of cardiovascular or respiratory disease and a normal resting blood pressure and a normal resting electrocardiogram were studied. All volunteers gave their informed consent for the study. Ethics approval was obtained from the institutional Research Ethics Committee (Royal Adelaide Hospital). Exclusion criteria were contraindications to MRI scanning and arrhythmia.

2. 1. 2. Patients with Atrial Septal Defects

Consecutive patients with secundum atrial septal defects diagnosed on transthoracic echocardiography (TTE) and with significant left to right shunt (>1.5:1) were invited to undergo both transoesophageal echocardiography (TOE) and cardiac magnetic resonance imaging (MRI). Only patients in sinus rhythm pre-ASD closure were included in the study.

2. 2. ANIMAL MODEL OF ATHEROSCLEROSIS

2. 2. 1. Rabbit Aortic Atherosclerosis

Cholesterol fed New Zealand White rabbits (Institute of Medical and Veterinary Science, Gilles Plains, Australia) aged 12 weeks were used. Complex atherosclerotic aortic lesions were induced in New Zealand white rabbits (3.0 to 3.5 kg) by a

combination of atherogenic diet (0.2% cholesterol enriched chow, Glen Forest Stock Feed, Western Australia) for 17 weeks and balloon denudation, one week after initiation of the atherogenic diet. Aortic denudation of the aorta from the aortic arch to the iliac bifurcation was performed by four withdrawals, with moderate resistance, of a 4 French Fogarty embolectomy catheter introduced through the iliac artery. All procedures were performed under general anaesthesia by intramuscular injection of ketamine (Fort Dodge Animal Health, Fort Dodge, IA) (20mg/kg) and xylazine (Bayer Corporation, Shawnee Mission, KA) (10mg/kg).

2. 3. CMR SYSTEM AND IMAGING SEQUENCES

The Siemens Sonata system (Siemens Medical Solutions, Erlangen, Germany) is a high resolution, whole body imaging system operated at 1.5 Tesla. All magnetic resonance imaging for the purposes of this thesis was performed with this system.

2. 3. 1. Ventricular volume and function sequences

2. 3. 1. 1. Steady state in free precession sequence (SSFP)

All cine images were acquired with retrospectively ECG-gated True FISP (Fast Imaging with Steady-State Precision), a steady state in fee precession (SSFP) sequence. The short axis section thickness was 6 mm with intersection gaps of 4 mm. Image matrix 256 X 150, field of view 380 mm, repetition time 52.05 ms, echo time 1.74 ms and flip angle 70°. Twelve to 17 heart phases were acquired per repetition time interval. This has an in-plane resolution of 1.4 x 1. 8 mm and a temporal resolution of 50 ms. Retrospective ECG-gating ensures that end-diastole is included, which can be missed with prospective ECG triggering (Gatehouse and Firmin 2000).

2. 3. 1. 2. Image Acquisition

All Cardiac MR imaging studies were performed with subjects in the supine position with a phased array surface coil. Long-axis reference views were used for positioning the 8 to 12 perpendicular LV short-axis slices from the level of the mitral valve to the left ventricular apex. Images were obtained during breath-hold (8 to 10 seconds) with retrospectively ECG-gated True FISP sequences.

2. 3. 1. 3. Image Analysis

Ventricular analysis was performed off-line with a proprietary software program (Argus software, Siemens, Germany). For the left ventricular (LV) data set, short-axis endocardial contours were manually traced in end-diastole (start of R-wave) and in end-systole (smallest cavity area). Papillary muscles and trabeculations were excluded from the ventricular volume and were included if contiguous with the myocardial mass (Lorenz et al. 1999). The basal slice was selected if the blood volume was surrounded by >50% of ventricular myocardium. In the right ventricular (RV) data sets, endocardial contours were manually traced in LV end-diastole and in end-systole (Lorenz et al. 1999). For the right ventricular (RV) data set, one observer manually traced the endocardial contours at end-diastole and at end-systole.

Both LV and RV end-diastolic and end-systolic cavity surface areas were summed up and volumes: end-diastolic (EDV) and end-systolic (ESV) estimated by multiplying with interslice intervals as per Simpson's rule. Ejection fraction (EF) was calculated as EF = (EDV-ESV)/EDV X 100 (%). LV mass = 1.05 X (epicardial volume – endocardial volume). RV mass was not measured.

2. 3. 2. Congenital Anatomy and Volume Sequences

Cardiac MRI studies were performed with subjects in the supine position using a 1.5 Tesla MRI scanner (Siemens Sonata, Germany) and a phased array surface coil. Images were obtained during breath-hold (8 to 10 seconds) with retrospectively cardiac-gated True FISP (Fast Imaging with Steady-state free precession) sequences. Both short (modified bi-atrial) and long axis images (4 chamber views) were obtained through the ASD, with section thickness of 6 mm and no intersection gap. Thus, consecutive slices were obtained to cover the whole of the interatrial septum in both short and long axis views. Assessment of atrial septal margins, maximal and minimal defect dimensions in both short and long axis views was performed.

For the ventricular image set, long-axis reference views were used for positioning 8 to 12 perpendicular ventricular short-axis slices from the level of the mitral valve to the left ventricular apex. Images were obtained during end-expiratory breath-hold (8 to 10 seconds) with retrospectively ECG-gated True-FISP (Fast Imaging with Steady-State Precision) sequences (Image matrix 256 X 150, field of view 380 mm, repetition time 52.05 ms, echo time 1.74 ms and flip angle 70°). Ventricular short axis slice thickness was 6 mm with intersection gaps of 4 mm, based on previous published studies (Alfakih et al. 2003; Lorenz et al. 1999).

For the atrial image set, multiple contiguous slices in both short (bi-atrial) and horizontal long axis views (four chamber) were obtained through the ASD, with slice thickness of 6 mm and no intersection gap.

2. 3. 2. 1. Measurement of the atrial septal margins and defect size

TOE and CMR studies were reviewed retrospectively and 2 independent observers performed the measurements. Images were reviewed for (a) assessibility of defect size and septal margins by TOE, and (b) assessibility of defect size and septal margins by CMR, (c) Agreement of the measurements between TOE and CMR. The maximal diameters of the atrial septal defects were measured on both TOE and CMR. Atrial septal margins were measured as previously published (Durongpisitkul et al. 2004; Masani 2001). The anterior inferior (AI) rim was measured from the defect to the mitral valve, the anterior superior (AS) rim from the defect to the aortic root, posterior inferior (PI) rim from the defect to the inferior vena cava and posterior superior (PS) rim from the defect to the superior vena cava (see Figure 1, Chapter 4).

The TOE views for measurement of the rims were: the mid-oesophageal four-chamber view for AI rim, basal short axis view for AS rim and biatrial views for PI and PS rims. Corresponding CMR views were the four-chamber view for AI rim, short axis view through the aorta for the AS rim and modified biatrial short axis views for PS and PI measurements. The size of the device occluder device used was also compared to the maximal defect size on CMR and TOE in patients who subsequently underwent ASD closure.

2. 3. 2. 2. Image Analysis

Ventricular and atrial analyses were performed off-line with a proprietary software program (Argus software, Siemens Medical Solutions, Germany). For the left ventricular (LV) data set, short-axis endocardial and epicardial contours were

manually traced in end-diastole (at start of R-wave) and in end-systole (smallest cavity area). Papillary muscles and trabeculations were excluded from the ventricular volume and were included if contiguous with the myocardial mass. The basal slice was selected as the slice where the blood volume was surrounded by >50% of ventricular myocardium (Alfakih et al. 2003; Lorenz et al. 1999). For the right ventricular (RV) data set, one observer manually traced the endocardial contours at end-diastole and at end-systole. The selection of the RV basal slice was based on published methods where, if the pulmonary valve was seen, only the portion of the volume below the level of the pulmonary valve was included (Alfakih et al. 2003). Both LV and RV end-diastolic and end-systolic cavity surface areas were summed up and volumes: end-diastolic (EDV) and end-systolic (ESV) estimated by multiplying with interslice intervals as per Simpson's rule. Ejection fraction (EF) was calculated as EF = (EDV-ESV)/EDV X 100 (%). LV mass = 1.05 X (epicardial volume – endocardial volume).

A true three-dimensional atrial volume assessment technique in which the endocardial borders were manually traced for both left and right atria in the horizontal long axis (four chamber) views in ventricular end-systole when atrial volume is maximal (Hauser et al. 2004). Borders of left atrium were defined as the plane of the mitral valve and the visually apparent juncture of left atrium with pulmonary veins. Borders of right atrium were defined as the plane of the tricuspid valve and the juncture with the vena cavae. The atrial appendage was included if present on the images. Atrial volumes were calculated as a sum of atrial cavity areas with interslice intervals using a modification of Simpson's rule.

2. 3. 3. Rabbit Black Blood CMR Imaging

2. 3. 3. 1. Imaging Sequences

The black blood MR imaging techniques used in this thesis was Fast spin echo (FSE). Standard FSE MR techniques were used to provide high-resolution images of rabbit aortic atherosclerotic. The animals were fully anaesthetised with ketamine and xylazine as described above and placed supine in the 1.5 Tesla MRI system (Sonata, Siemens Medical Solutions), using a conventional phased-array volume coil. Fast gradient-echo coronal images were used to localise the abdominal aorta. Sequential axial images (3-mm thickness, 56 slices) of the abdominal aorta from the renal arteries to the iliac bifurcation were obtained using a fast spin-echo sequence with an in plane resolution of 350 x 350 μm (PDW: TR/TE: 2000/11 msec, field of view (FOV)=9 x 9 cm, matrix 256 x 256, echo train length=9, flip angle=180°, signal averages=4). Inferior and superior radio frequency flow saturation pulses were used to null signal from flowing blood in the inferior vena cava and aorta. Fat suppression was used to null the signal from the peri-adventitial fat, in order to minimise chemical shift artefacts.

2. 3. 3. 2. Imaging analysis

All images were analysed by an investigator who was blinded to the treatment status of the animals. The MR images from the same animals were matched by use of distance from the renal arteries and the iliac bifurcation for registration as previously validated (Helft et al. 2001; Worthley et al. 2000). Cross sectional areas of the lumen and the outer boundary of each aortic section were determined by manual tracing with Image Pro Plus (Media Cybernetics) by an observer who was blinded to the treatment status of the animals. From these measurements, lumen area, outer vessel area and vessel wall area (outer vessel area minus lumen area) were calculated. The

outer wall was defined as the vessel wall-epicardial fat interface. The vessel wall areas of 8 contiguous abdominal aortic slices per animal were consecutively averaged.

2. 4. TOE IMAGING

2. 4. 1. Image Acquisition

TOE imaging was performed with a Sonos 5500 (Phillips) TOE system with a multiplanar 7.0mHz phased-array transducer. Cross-sectional studies of the atrial septum were performed utilising multi-plane views as previously described: mid-oesophageal 4-chamber views, short axis view and biatrial long axis views (Cooke et al. 2001).

2. 4. 2. Image Analysis

The maximal diameters of the atrial septal defects were measured on both TOE and CMR. Atrial septal margins were measured as previously published (Durongpisitkul et al. 2004; Masani 2001). The anterior inferior (AI) rim was measured from the defect to the mitral valve, the anterior superior (AS) rim from the defect to the aortic root, posterior inferior (PI) rim from the defect to the inferior vena cava and posterior superior (PS) rim from the defect to the superior vena cava.

The TOE views for measurement of the rims were: the mid-oesophageal four-chamber view for AI rim, basal short axis view for AS rim and biatrial views for PI and PS rims. Corresponding CMR views were the four-chamber view for AI rim, short axis view through the aorta for the AS rim and modified biatrial short axis views for PS and PI measurements. The size of the device occluder device used was

also compared to the maximal defect size on CMR and TOE in patients who subsequently underwent ASD closure.

2. 5. MDCT IMAGING SYSTEM AND SEQUENCES

2. 5. 1. Image Acquisition

A sixteen detector MDCT scanner (Siemens Sensation 16, Germany) was used (12 X 0.75 mm collimation, gantry rotation time 420 ms, table feed 2.8 mm per rotation, tube voltage 0f 120 kV). A non-contrast localization scan was first performed to obtain an anteroposterior view of the head and neck. This was used to position the imaging volume for carotid imaging. Automated bolus tracking software allows the full bolus to be accurately followed without a timing bolus first.

2. 5. 2. Image Analysis

Cross sectional images were reconstructed with a slice thickness of 1.0 mm in 1.0 mm intervals. These images were then transferred to a computer workstation for analysis using Image-Pro Plus (Media Cybernatics) where the cross-sectional areas of the lumen and outer boundary of the carotid lesion were determined for the CT images by manual tracing.

2. 6. MICRO-CT IMAGING SYSTEM AND SEQUENCES

2. 6. 1. Image Acquisition

Micro-CT scanning was performed on a desktop micro-CT (Skyscan 1072; Aartselaar, Belgium). Carotid endarterectomy specimens, fixed in formalin were place in sealed polypropylene tubes. The carotid specimens were held in place in the tubes with polystyrene, which has X-ray absorption equivalent to air. Samples were then imaged using an unfiltered tungsten x-ray source, which was run at 80kV and 120μA. Images were collected at 0.675-degree steps through a total angle of approximately 180 degrees. Total imaging time per sample was 1 hour. Although the maximum resolution for the Skyscan 1072 is approximately 4 μm, however due to the size of carotid endarterectomy specimens, the resolution ranged from 10 to 18 μm.

2. 6. 2. Image analysis

Projection images were converted to tomogram using proprietary software (Skyscan ConeRec). Three-dimensional rendering of the images and data analysis was performed using CT-Analyser software (Skyscan). Non-calcified areas could not be distinguished from surrounding tissues because of comparable X-ray absorption, while calcified areas were able to be easily distinguished. Density histograms were generated which provided quantitative results. The lower limit for threshold was selected to exclude non-calcified tissue, while the upper limit corresponded to the densest calcified part. The 3-D models rendered from the reconstructed cross-sections were analysed to determine calcium volume.

2. 7. STATISTICAL ANALYSIS

Interobserver variability was assessed using the Bland and Altman method (Bland and Altman 1986) as well as intraclass correlation coefficients. The correlation calculation is a statistical method to quantify the relationship between two variables measured independently and where r=1 is taken as a perfect correlation. Unpaired sample t-tests were performed for the difference in measurements between males and females with the level of significance taken as $p<0.05$.

Data is presented as mean ± standard deviation. Analyses between TOE and MRI were made using simple linear regression analysis (SPSS 11.0 software) and Bland Altmann analysis. Statistical significance was taken at a p value of 0.05.

Comparison of cardiac volumes pre- and 6 months post-ASD closure was performed with paired t-testing between groups. Statistical significance was taken as $p<0.05$.
Intra and Interobserver variability was assessed using the Bland and Altman method (Bland and Altman 1986) as well as intraclass correlation coefficients.

Paired Student's t tests were used to compare MR image-derived parameters from the same sites in the rabbit abdominal aorta at the 2 time points. All probabilities are 2-sided and statistical significance taken as a value of $p<0.05$. All values are assessed as mean ± SEM (mm^2).

For the MDCT calcification project, all data was assessed for normality using the Kolmogorov-Smirnov statistic (SPSS 11.0 software). Data is presented as mean calcium volume (mm^3±SD) and simple linear regression performed for normally distributed data. Bland-Altman analyses were performed between the different

methods, as the most appropriate comparison of different techniques assessing the same entity (i.e. amount of vascular calcification).

Chapter 3:

CARDIAC MRI ASSESSMENT OF LEFT AND RIGHT VENTRICULAR PARAMETERS IN HEALTHY AUSTRALIAN NORMAL VOLUNTEERS

TABLE OF CONTENTS

3. 1. INTRODUCTION

Cardiovascular Magnetic Resonance (CMR) imaging has been shown to be an accurate and reproducible tool for the assessment of left and right ventricular measurements (Alfakih et al. 2003; Grothues et al. 2004; Grothues et al. 2002; Hudsmith et al. 2005; Lorenz et al. 1999). The information that can be obtained in a single examination includes ventricular volumes, mass and ejection fraction which provide both diagnostic and prognostic information. Like echocardiography, CMR is a non-invasive investigation and does not utilise ionising radiation. However, the additional advantage is the higher inter-observer reproducibility compared to echocardiography, as CMR does not rely on geometric assumptions (Grothues et al. 2002). This allows the serial assessment of ventricular parameters particularly the monitoring of ventricular remodelling with therapy.

Earlier CMR studies for ventricular function and volumes utilised a technique with a pulse sequence using segmented k-space turbo gradient echo (Alfakih et al. 2003). This has remained in current use, but a more recent technique is the steady-state free precession (SSFP) technique. This technique has been validated in animal studies (Fieno et al. 2002). Compared to the gradient echo technique, SSFP allows improved definition of the endocardial borders and faster acquisition time (Alfakih et al. 2003; Moon et al. 2002).

In this study, we sought to establish normal ranges for left ventricular (LV) volumes, mass and ejection fraction (EF) as well as right ventricular volumes in normal healthy non-Aboriginal Australian volunteers. We also sought to establish that the assessment of these parameters using CMR with SSFP is reproducible.

3. 2. METHODS

3. 2. 1. Study Population

Sixty (41 males, 19 females, mean age 51±13 years) consecutive normal healthy volunteers with no history of cardiovascular or respiratory disease and a normal resting blood pressure and a normal resting electrocardiogram were studied. All volunteers gave their informed consent for the study. Ethics approval was obtained from the institutional Research Ethics Committee (Royal Adelaide Hospital, South Australia). Exclusion criteria were contraindications to CMR scanning and arrhythmia.

3. 2. 2. Image Acquisition

All CMR imaging studies were performed with subjects in the supine position using a 1.5 Tesla MRI scanner (Siemens Sonata, Germany) and a phased array surface coil. Long-axis reference views were used for positioning the 8 to 12 perpendicular LV short-axis slices from the level of the mitral valve to the left ventricular apex. Images were obtained during breath-hold (8 to 10 seconds) with prospectively ECG-gated True FISP (Fast Imaging with Steady-State Precision) sequences. The short axis section thickness were 6 mm with intersection gaps of 4 mm, based on previous published studies (Alfakih et al. 2003; Hudsmith et al. 2005; Lorenz et al. 1999). Acquisition time was 90% of the RR-interval, image matrix 256 X 150, field of view 380 mm, repetition time 52.05 ms, echo time 1.74 ms and flip angle 70°. Twelve to 17 heart phases were acquired per repetition time interval.

3. 2. 3. Image Analysis

Ventricular analysis was performed off-line with a proprietary software program (Argus software, Siemens Medical Solutions, Germany). For the left ventricular (LV) data set, short-axis endocardial and epicardial contours were manually traced in end-diastole (start of R-wave) and in end-systole (smallest cavity area). Papillary muscles and trabeculations were excluded from the ventricular volume and were included if contiguous with the myocardial mass. The basal slice was selected as the slice where the blood volume was surrounded by >50% of ventricular myocardium (Alfakih et al. 2003; Lorenz et al. 1999). For the right ventricular (RV) data set, one observer manually traced the endocardial contours at end-diastole and at end-systole. The selection of the RV basal slice was based on published methods where, if the pulmonary valve was seen, only the portion of the volume below the level of the pulmonary valve was included (Alfakih et al. 2003).

Both LV and RV end-diastolic and end-systolic cavity surface areas were summed up and volumes: end-diastolic (EDV) and end-systolic (ESV) estimated by multiplying with interslice intervals as per Simpson's rule. Ejection fraction (EF) was calculated as EF = (EDV-ESV)/EDV X 100 (%). LV mass = 1.05 X (epicardial volume – endocardial volume). RV mass was not measured.

3. 2. 4. Reproducibility

To assess the interobserver variability, a second independent observer re-measured the data sets for both left and right ventricular parameters.

3. 2. 5. Statistical Analysis

Data was collected for assessment of left ventricular EF, mass, EDV and ESV, and presented as mean ± standard deviation (SD). The normal range was calculated as 2 standard deviations above the mean. Interobserver variability was assessed using the Bland and Altman method (Bland and Altman 1986) as well as intraclass correlation coefficients. The correlation calculation is a statistical method to quantify the relationship between two variables measured independently and where r=1 is taken as a perfect correlation. Unpaired sample t-tests were performed for the difference in measurements between males and females with the level of significance taken as $p<0.05\%$. Statistical analyses were performed using SPSS software.

3. 3. RESULTS

Total imaging time was approximately 15 minutes. All patients were able to complete the full protocol and diagnostic imaging was obtained in all subjects. The left ventricular parameters were: EF 58.5 ± 8.0 %, LV mass 114.2 ± 40.6 g, EDV 117.3 ± 33.4 mls and ESV 50.0 ± 22.2 mls.

The right ventricular parameters were: EF 45.6 ± 11.6 %, EDV 163.5 ± 52.2 mls and ESV 89.5 ± 34.3 mls.

Figure 1 shows a mid-ventricular short axis SSFP image in end-diastole and end-systole with left ventricular endocardial and epicardial contours traced and right ventricular endocardial contour traced.

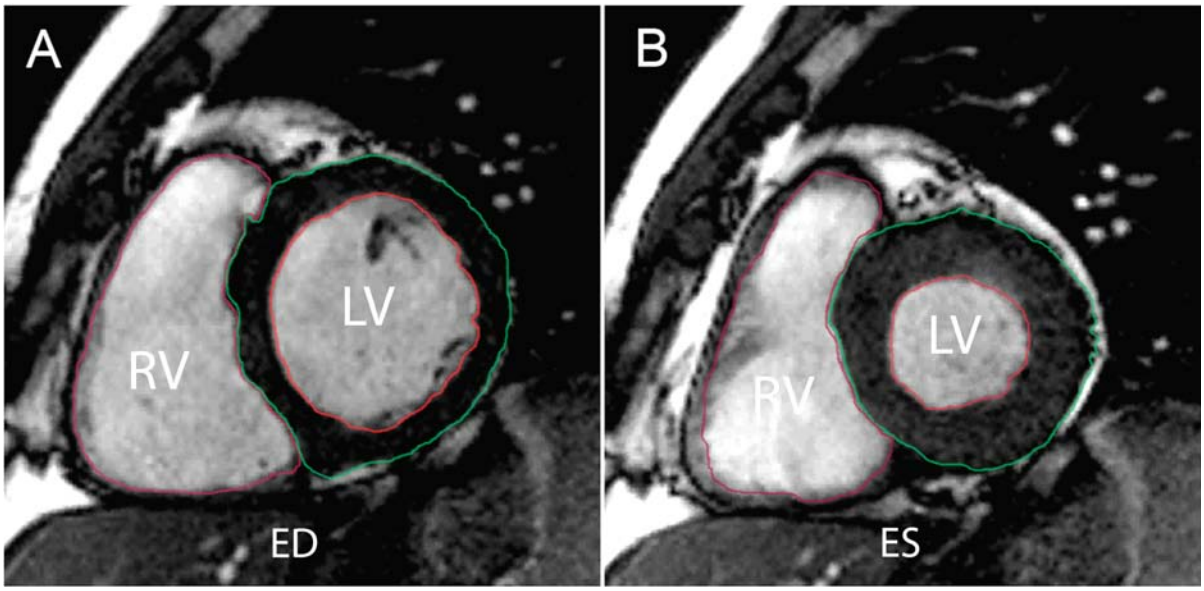

Figure 1: CMR image of a mid-ventricular short axis slice in end-diastole (ED) and end-systole (ES) with traced left ventricular endocardial (red) and epicardial contours (green) and right ventricular endocardial contour (red).

Tables 1 and 2 show the means ± standard deviation for all LV and RV volumes for both males and females.

Table 1. Mean Values ± SD of left ventricular (LV) dimensions with SSFP

	Combined	**Males**	**Females**
EDV (mls)	117.26 ± 33.40	124.22 ± 32.95	104.58 ± 31.24
ESV (mls)	50.03 ± 20.20	52.92 ± 20.54	44.77 ± 19.04
EF (%)	58.52 ± 7.97	58.62 ± 8.24	58.35 ± 7.68
Mass (g)	114.16 ± 40.61	131.20 ± 39.85	83.07 ± 16.66
LV EDV/BSA (ml/m2)	59.92 ± 17.31	60.21 ± 16.69	61.82 ± 21.26
LV mass/BSA (g/m2)	58.65 ± 10.55	71.98 ± 12.8	52.10 ± 10.37
LV EDV/HT (ml/m)	66.44 ± 21.46	69.97 ± 18.54	64.13 ± 22.01
LV Mass/ HT (g/m2)	65.59 ± 17.46	71.98 ± 12.80	54.09 ± 11.28

Table 2. Mean Values ± SD of right ventricular (RV) dimensions with SSFP

	Combined	Males	Females
EDV (ml)	163.63 ± 52.21	186.23 ± 40.60	116.87 ± 42.69
ESV (ml)	89.48 ± 34.26	92.74 ± 26.93	57.11 ± 23.33
EF (%)	45.59 ± 11.58	45.89 ± 9.56	44.75± 16.38
RV EDV/BSA (ml/m2)	81.43 ± 23.14	86.95 ± 28.97	67.03 ± 24.25
RV EDV/HT (g/m2)	92.96 ± 28.62	101.64 ± 33.85	70.34 ± 8.11

Intraclass correlation coefficients between 2 independent observers for LV parameters were: EF 0.82, LV mass 0.94, EDV 0.95 and ESV 0.91. Results from the Bland and Altman analyses for interobserver and intraobserver variability for LV and RV are presented as mean, the difference between the means ± 2 SD. Interobserver mean of LVEF was 56.6% with difference between the means of 0.7 ± 8.6%. Interobserver mean of RVEF was 51.1%, difference between the means -1.7 ± 22.7%. This is presented graphically for ejection fraction in Figures 2A and 2B for LV inter- and intraobserver data and in Figures 3A and 3B for RV inter- and intraobserver data. Interobserver LVEDV mean 124, difference 10.8 ± 33 mls, LVESV mean 54.1, difference 3.3 ± 18.0 mls and LV mass mean 107, difference 5.24 ± 37 g. Interobserver RVEDV mean 151.8, difference 31.5 ± 48.4 mls and RVESV mean 76.0, difference 18.21 ± 49 mls.

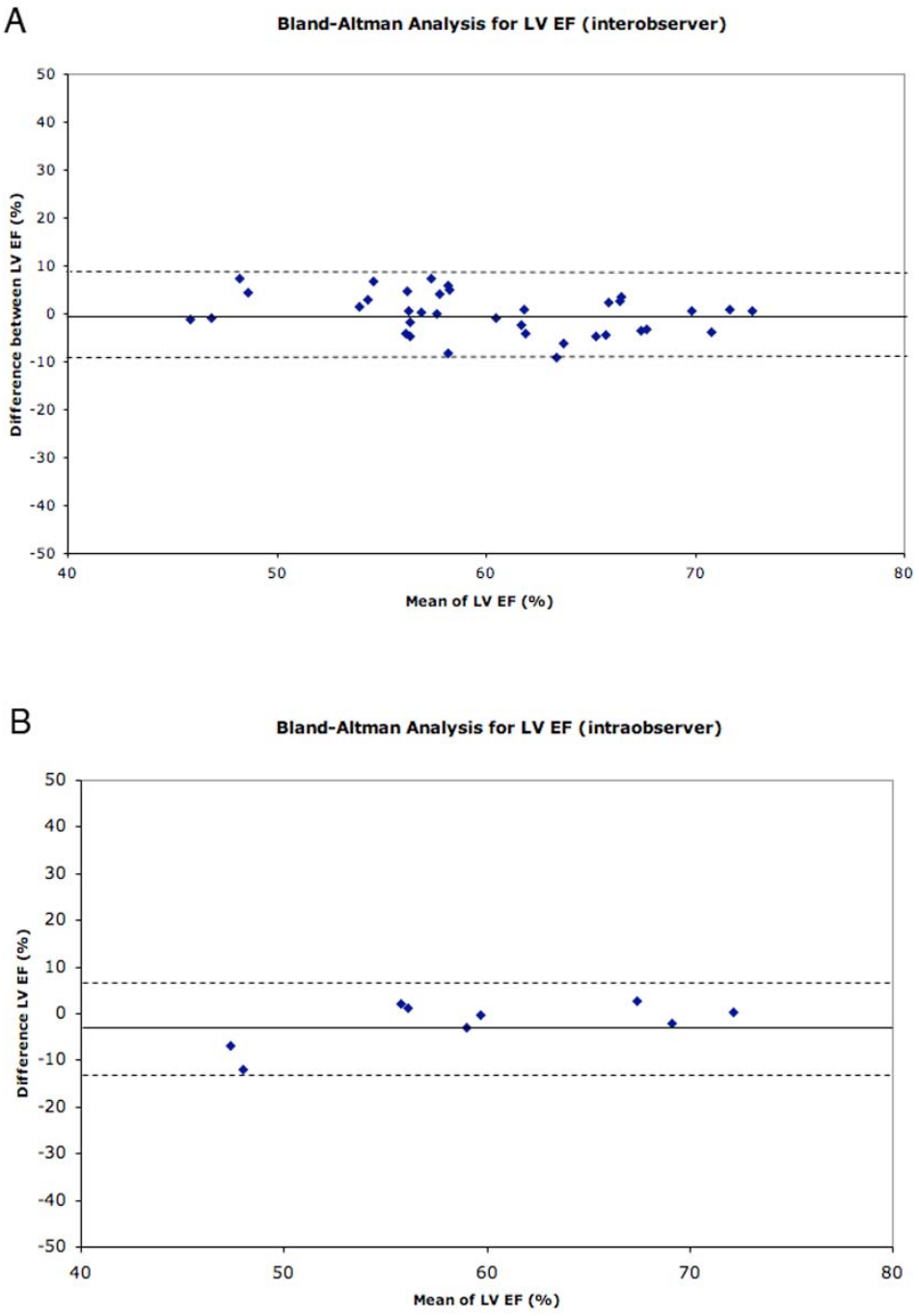

Figure 2: Bland and Altman analyses of LV ejection fraction for interobserver (Figure 2A) and intraobserver (Figure 2B) variability. Solid line indicates the mean difference and dashed lines ± 2 standard deviations (SD).

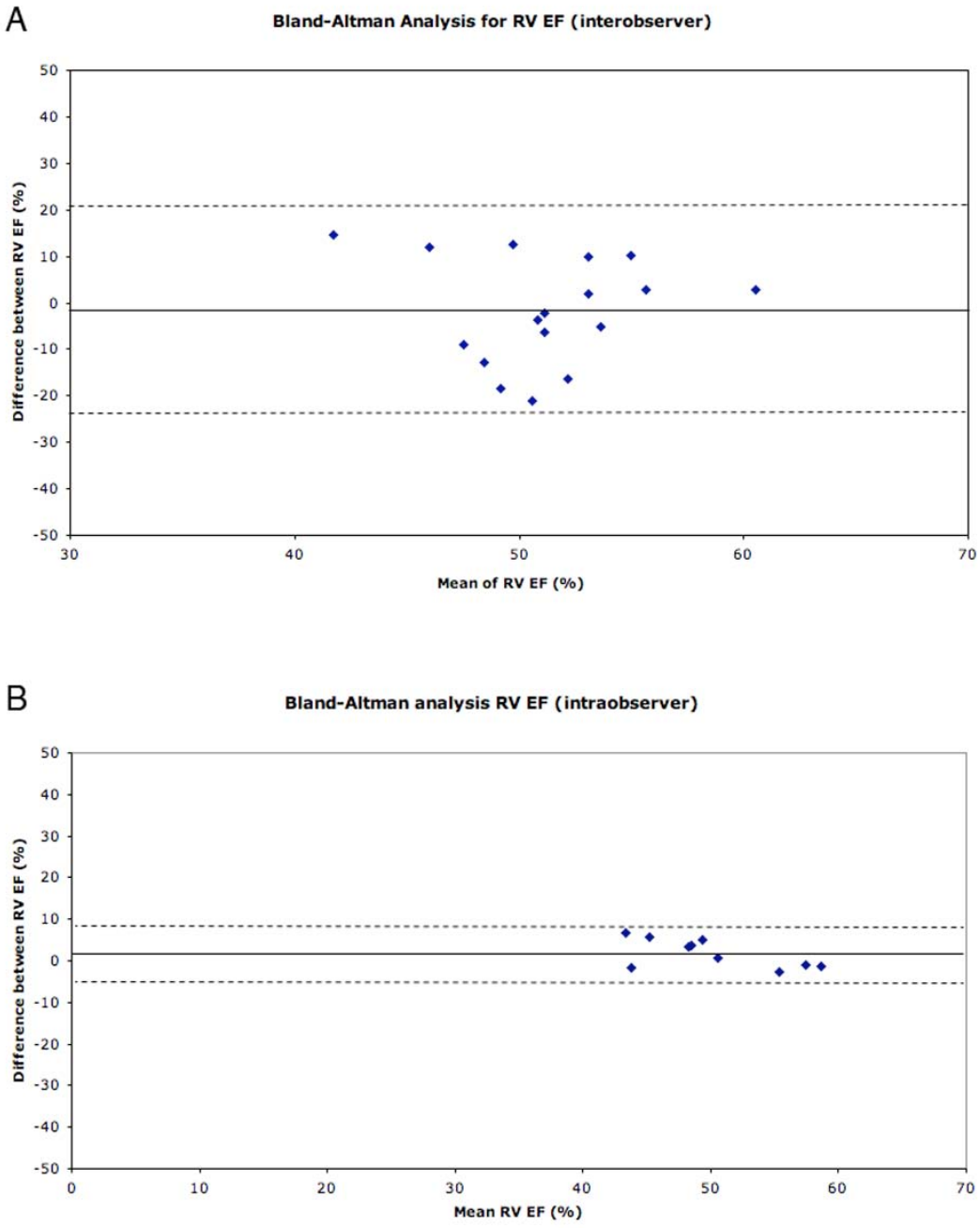

Figure 3: Bland and Altman analyses of RV ejection fraction for interobserver (Figure 3A) and intraobserver (Figure 3B) variability. Solid line indicates the mean difference and dashed lines ± 2 standard deviations (SD)

There was a statistically significant difference in volumes and mass between males and females. This difference was present for LVEDV ($p=0.01$), RVEDV ($p<0.001$), RVESV ($p<0.01$) as well as LV mass ($p<0.0001$). The difference between male and

female LV mass measurements remained significant after indexation to body surface area (p=0.008) but not the difference between the measurements for LVEDV and RVEDV. There was no significant difference in LVEF between males and females.

3. 4. DISCUSSION

Cardiovascular magnetic resonance imaging is a non-invasive and accurate method for assessing ventricular volumes, mass and function. This study has established the normal ranges for left and right ventricular parameters in a group of normal healthy Australian volunteers using CMR. We have used the more recent technique with steady-state free precession (SSFP) imaging, which allows for improved endocardial and epicardial border definition. The slice thickness and inter-slice gaps used (left ventricular slice thickness of 6 mm with a 4 mm inter-slice gap) were chosen on the basis of published studies of CMR assessment of LV function, volume and mass (Alfakih et al. 2003; Hudsmith et al. 2005). Although thinner slices without slice gaps may increase the accuracy of the ventricular imaging, problems with cross-excitation between slices and signal-to-noise become significant. Papillary muscles not contiguous with the myocardial mass were excluded in keeping with published studies, due to the variability created in attempting to include this (Lorenz et al. 1999). However, new software options may allow inclusion of the papillary muscles in the future.

The excellent reproducibility between observers using this technique for assessment of left ventricular parameters allows it to be a reliable tool for both baseline ventricular assessments as well as for serial measurements. This will be particularly

useful for assessing ventricular remodelling with therapy in both clinical and research settings.

In this study, we found that there was greater interobserver and intraobserver variability in the right ventricular parameters. This could be due to factors related to the shape of the RV, selection of the basal slice as well as the irregular surface of the RV endocardial surface due to trabeculations, which results in some difficulty in tracing the surfaces. These factors may be improved with further software development to automate boundary detection and also assist in the selection of the basal slice during analyses.

Our results were comparable to the results obtained with SSFP sequences in normal populations except for slightly smaller left ventricular end-diastolic volumes in our group. This could be due to the known difficulty in selecting the basal slice for inclusion in ventricular volume analysis. Previous CMR studies on normal ventricular parameters have predominantly used the older gradient echo pulse sequence, although there are studies comparing it to the newer SSFP sequences (Alfakih et al. 2003; Moon et al. 2002). The differences are small, but consistent between the techniques, and may relate to variations in imaging characteristics of the blood-myocardial interface with different sequences. In one study, the LV EDV and LV ESV were larger and LV mass was smaller with SSFP imaging than with the older sequences (Moon et al. 2002). However, this does highlight the need for robust population based “normal” values for the different techniques, and furthermore highlights that echocardiography based indices should not be used for CMR normal indices.

Our results demonstrate a statistically significant difference between male and female LV and RV volumes as well as in the LV mass, but no difference in the LV

EF. This has also been previously described. When indexed to body surface area, the gender difference in LV mass persisted, but not the ventricular volumes.

3. 6. CONCLUSION

Cardiac magnetic resonance imaging provides high quality information about cardiac structure and function, with a high level of reproducibility. Normal values for the non-Aboriginal Australian population are provided. Further work to define such values in Aboriginal Australians is required.

Chapter 4:

ASSESSMENT OF ATRIAL SEPTAL DEFECTS: A COMPARATIVE STUDY IN ADULT PATIENTS WITH CARDIAC MAGNETIC RESONANCE AND TRANSOESPHAGEAL ECHOCARDIOGRAPHY

TABLE OF CONTENTS

4. 1. INTRODUCTION

Atrial septal defects are the most common congenital cardiac malformation first diagnosed in adults and account for approximately 10% of all congenital heart lesions (Hoffman et al. 2004). Patients with a significant shunt (Qp/Qs >1.5/1.0) experience symptoms over time with effort dyspnoea seen in about 30% of patients by the third decade and in over 75% of patients by the 5th decade. Complications may include the development of pulmonary hypertension, supraventricular arrhythmias (atrial fibrillation and atrial flutter) and right-sided heart failure from right ventricular volume overload.

Surgical closure of atrial septal defects (ASDs) has previously been shown to have excellent results in both medium and long term studies (Roos-Hesselink et al. 2003), but is associated with significant morbidity and mortality (Galal et al. 1994). Many adults with secundum ASDs are now able to have these defects closed percutaneously using septal occluder devices such as the Amplatzer Septal Occluder (ASO), a self-expanding circular double disc with a conjoint waist containing polytetrafluoroethylene (PTFE) and a nitinol mesh. This device has now become an accepted alternative to surgical repair with studies comparing ASO device closure to surgical closure showing decreased complication rates, shorter hospital stays and greater cost-effectiveness (Du et al. 2002).

The echocardiographic morphology of the ASD and accurate assessment of the stretched diameter has been important for patient selection. Initially, it was felt that atrial septal defects up to 26 mm stretched diameter could be closed with the ASO (Chan et al. 1999). More recently, there is registry data of larger ASDs closed successfully using the 40 mm ASO (Lopez et al. 2005) and this has been standard

clinical practice (Harper et al. 2002). Inclusion criteria for percutaneous ASD closure have included: 1) the presence of a secundum ASD <40mm by echocardiography, 2) a left-to-right shunt with a Qp/Qs ratio of >1.5:1 or the presence of right ventricular volume overload 3) patients with minimal shunt in the presence of symptoms and 4) the presence of a distance of >5 mm from the margins of the ASD to the coronary sinus, atrioventricular valves and right upper pulmonary vein as measured by echocardiography (Cooke et al. 2001; Du et al. 2002; Harper et al. 2002). Traditionally, these assessments of ASD size, geometry and atrial septal margins have been obtained by transoesophageal echocardiography (TOE) prior to the percutaneous closure (Cao et al. 2000; Cooke et al. 2001). This is a semi-invasive technique and all of the information could potentially be obtained by non-invasive cardiac magnetic resonance (CMR) imaging. Furthermore, TOE is imperfect at assessing all atrial septal margins. A large atrial septal defect that is located inferoposteriorly is difficult to both assess and close (Cooke et al. 2001) and relates to the limited assessment of the posterior inferior margin by TOE (Durongpisitkul et al. 2004).

The aim of this study was to compare the assessment of atrial septal defects in consecutive adult patients being considered for percutaneous ASD closure using CMR and TOE.

4. 2. METHODS

4. 2. 1. Subjects

Consecutive patients with secundum atrial septal defects diagnosed on transthoracic echocardiography (TTE) were invited to undergo both transoesophageal echocardiography (TOE) and cardiac magnetic resonance (CMR).

4. 2. 2. Transoesophageal echocardiographic imaging

TOE imaging was performed with a Sonos 5500 (Phillips) TOE system with a multiplanar 7.0mHz phased-array transducer. Cross-sectional studies of the atrial septum were performed utilising multi-plane views as previously described: mid-oesophageal 4-chamber views, short axis view and biatrial long axis views (Cooke et al. 2001).

4. 2. 3. Cardiac Magnetic Resonance

CMR studies were performed with subjects in the supine position using a 1.5 Tesla MRI scanner (Siemens Sonata, Germany) and a phased array surface coil. Images were obtained during end-expiratory breath-hold (8 to 10 seconds) with retrospectively cardiac-gated True FISP (Fast imaging with steady-state free precession) sequences. Both short (modified bi-atrial) and long axis images (4 chamber views) were obtained through the ASD, with section thickness of 6 mm and no intersection gap. Thus, consecutive slices were obtained to cover the whole of the interatrial septum in both short and long axis views. Assessment of atrial septal

margins, maximal and minimal defect dimensions in both short and long axis views was performed.

4. 2. 4. Measurement of the atrial septal margins and defect size

TOE and CMR studies were reviewed retrospectively and 2 independent observers performed the measurements. Images were reviewed for (a) assessibility of defect size and septal margins by TOE, and (b) assessibility of defect size and septal margins by CMR, (c) Agreement of the measurements between TOE and CMR. The maximal diameters of the atrial septal defects were measured on both TOE and CMR. Atrial septal margins were measured as previously published (Durongpisitkul et al. 2004; Masani 2001). The anterior inferior (AI) rim was measured from the defect to the mitral valve, the anterior superior (AS) rim from the defect to the aortic root, posterior inferior (PI) rim from the defect to the inferior vena cava and posterior superior (PS) rim from the defect to the superior vena cava (see Figure 1).

The TOE views for measurement of the rims were: the mid-oesophageal four-chamber view for AI rim, basal short axis view for AS rim and biatrial views for PI and PS rims. Corresponding CMR views were the four-chamber view for AI rim, short axis view through the aorta for the AS rim and modified biatrial short axis views for PS and PI measurements. The size of the device occluder device used was also compared to the maximal defect size on CMR and TOE in patients who subsequently underwent ASD closure.

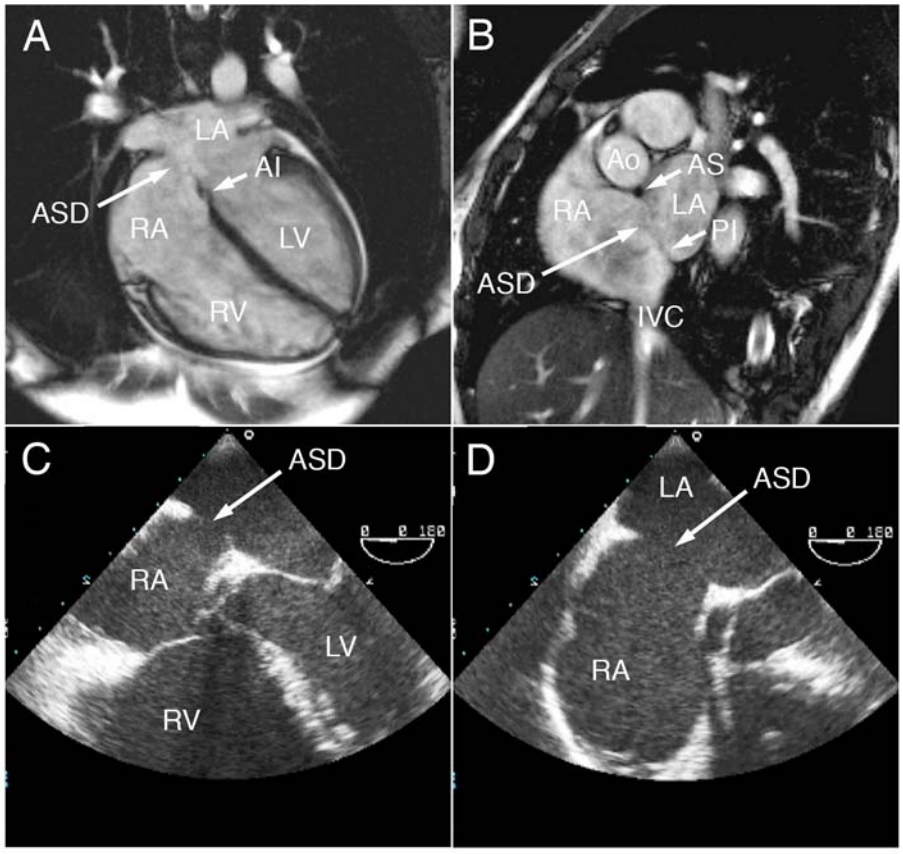

Figure 1 Atrial septal defect (ASD) and margins imaged with cardiac MRI (panel A – 4 chamber view, panel B – modified biatrial short axis view) and transoesophageal echocardiography (panel C – 4 chamber view, panel D – biatrial short axis view). Margins are denoted with AS anterior superior rim, AI anterior inferior, PI posterior inferior.

4. 2. 5. ASD device implantation

All implantation of the ASD devices with the Amplatzer Septal occluder were performed with TOE guidance and fluoroscopy. A sizing balloon was used to determine the stretched diameter of the ASD before selection and deployment of ASO device, as previously described (Harper et al. 2002). In brief, a Meditech balloon (Boston Scientific, Watertown, MA) sized 20 or 27 mm was used in this series. This balloon was inflated within the left atrium and firm continuous pressure applied to pull it into the atrial septum, using TOE guidance. The diameter at which

the balloon just gets through the atrial septal defect was the stretched balloon diameter (SBD).

4. 2. 6. Statistical Analysis

Data is presented as mean ± standard deviation. Analyses between TOE and CMR were made using simple linear regression analysis (SPSS 11.0 software) and Bland Altman analysis (Bland and Altman 1986). Statistical significance was taken at a p value of 0.05 or less.

4. 3. RESULTS

A total of 20 patients (M: F = 5: 15, mean age 42.8 years ± 15.7) were included in the analyses. All but 1 patient had both TOE and CMR to evaluate their suitability for percutaneous ASD closure. TOE was not performed in 1 patient due to history of an oesophageal stricture. CMR was well tolerated in all patients. Total CMR examination time was 20 to 30 minutes in all cases. Three patients were found not to be suitable for percutaneous ASD closure due to excessive ASD diameter of >30 mm on both TOE and CMR (CMR diameters 32, 38 and 33 mm) and all 3 patients went on to surgical closure.

4. 3. 1. Assessibility of defect and margins with TOE

The maximal defect size could be assessed in all patients (n=20) with TOE. The anterior inferior (AI) margin, which was measured from the defect to the mitral valve in the mid-oesophageal 4-chamber view could be assessed in all patients. The

anterior superior margin was assessable in 80%, the posterior inferior margin in 60% and the posterior superior margin in 70% of patients (See Table 1).

Table 1. Assessment of atrial septal defect size and margins (CMR vs. TOE)

	Able to be assessed by CMR (%)	Able to be assessed by TOE (%)
Maximal defect size	(20/20) 100%	(20/20) 100%
Anterior superior margin	(20/20) 100%	(16/20) 80%
Anterior inferior margin	(20/20) 100%	(17/20) 85%
Posterior superior margin	(19/20) 95%	(14/20) 70%
Posterior inferior margin	(20/20) 100%	(12/20) 60%

4. 3. 2. Assessibility of defect and margins with CMR

The maximal defect size could be assessed in all patients (n=20) with CMR. The anterior inferior, anterior superior and posterior inferior margins could be assessed in all patients. The posterior superior margin could not be assessed in only one patient.

4. 3. 3. Agreement between TOE and CMR

There was a good agreement between CMR and TOE for estimation of maximum defect size (R=0.87) and minimum defect size (0.92). There was similar agreement between CMR and TOE versus size of the ASO device (Maximum defect size by CMR vs. ASO size, R=0.53 and maximum defect size by TOE vs. ASO size R=0.57).

Bland and Altman analyses comparing CMR and TOE measurements of defect size and atrial septal margins are shown in Figures 2A to E and presented as mean of the

2 measurements obtained by MRI and TOE ± difference between the 2 measurements.

Figure 2 (A to E): Bland Altman comparative analyses of the mean ASD dimensions and difference in dimensions between CMR and TOE for A. Maximum defect size, B. Anterior inferior (AI) margins, C. Anterior superior (AS) margins, D. Posterior inferior (PI) margins and E. Posterior superior (PS) margins.

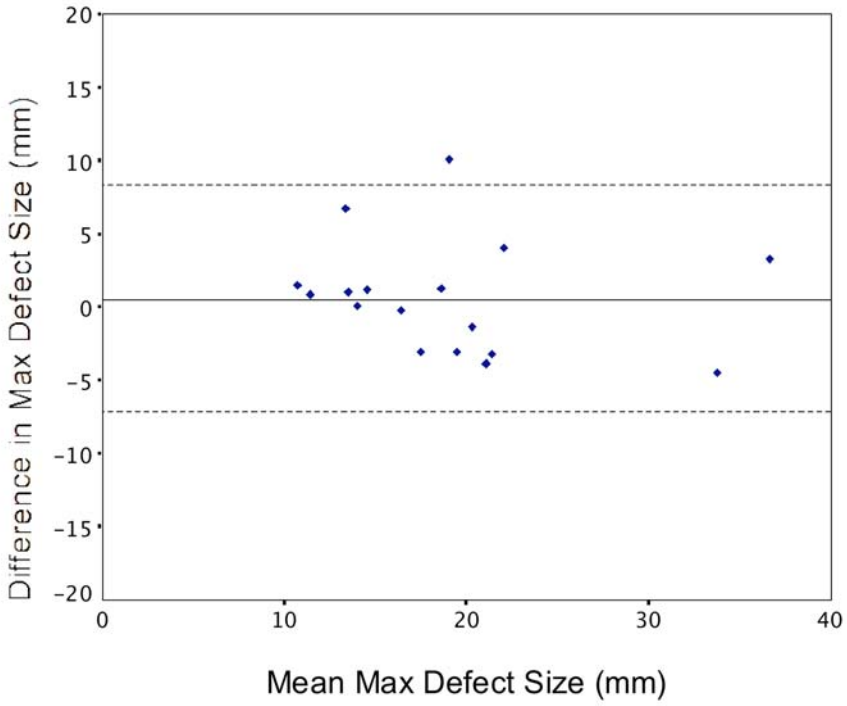

Figure 2 A

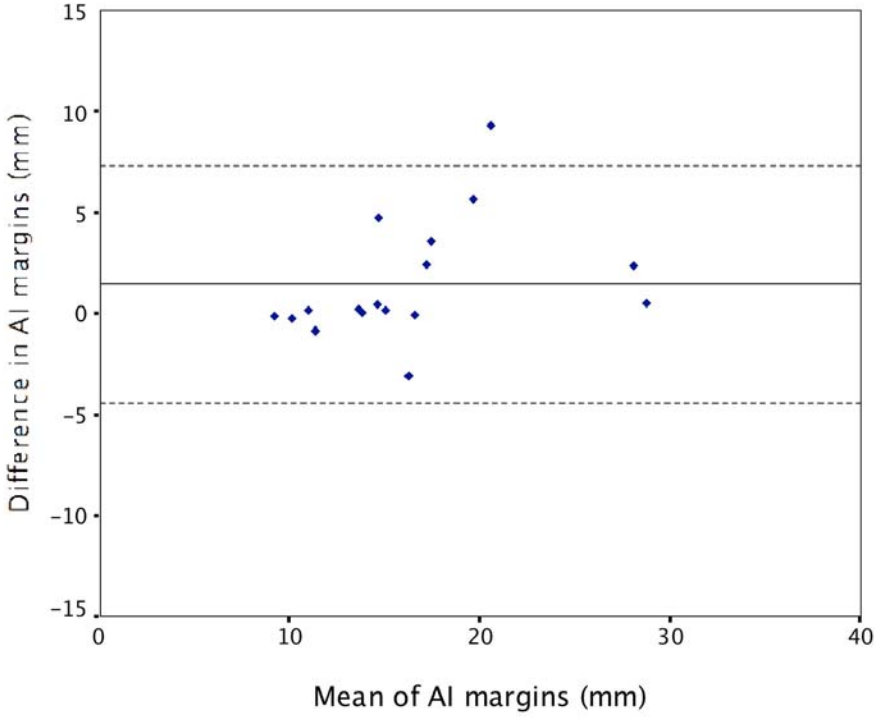

Figure 2 B

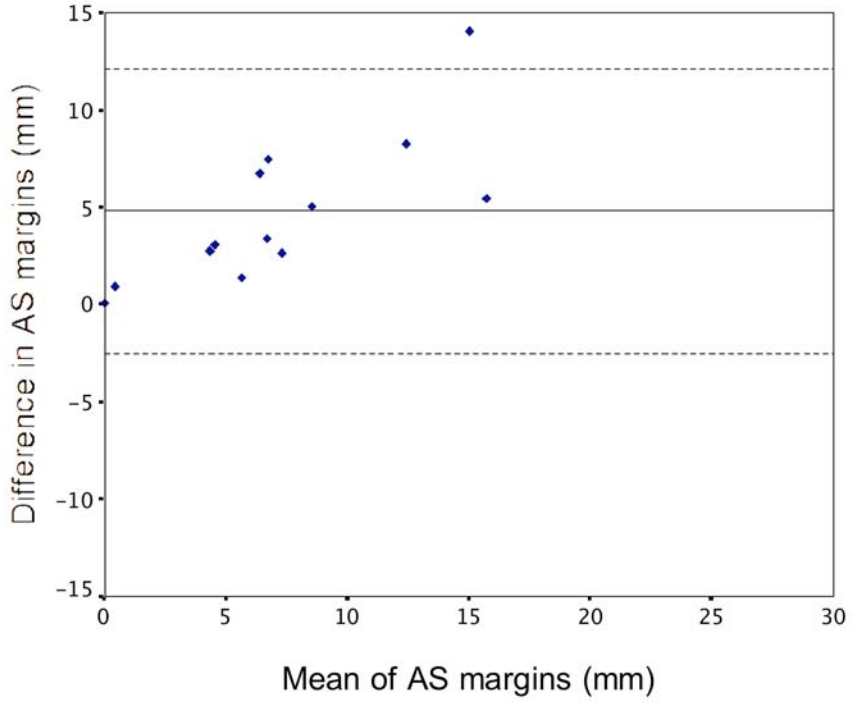

Figure 2 C

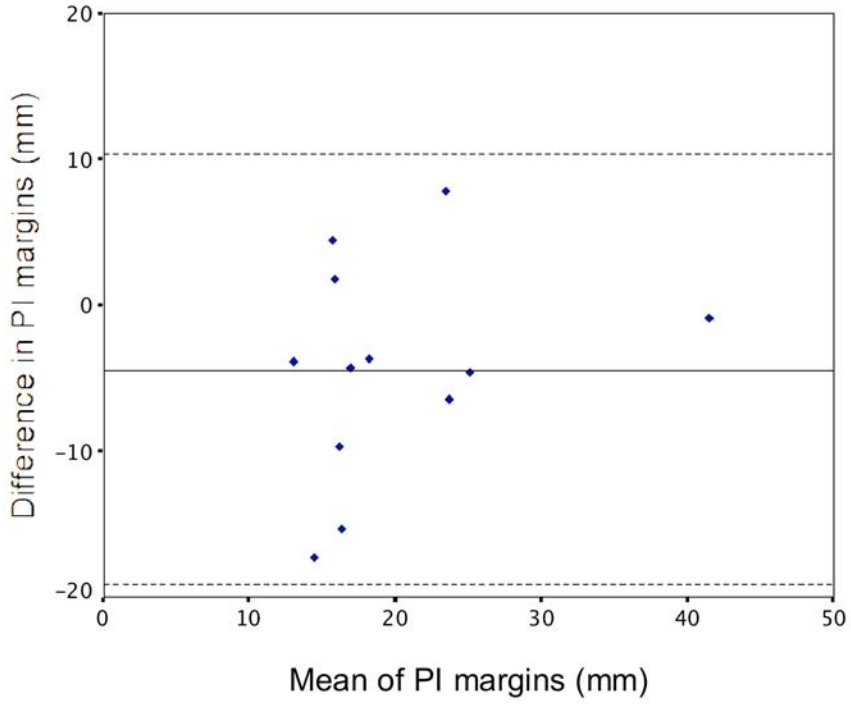

Figure 2 D

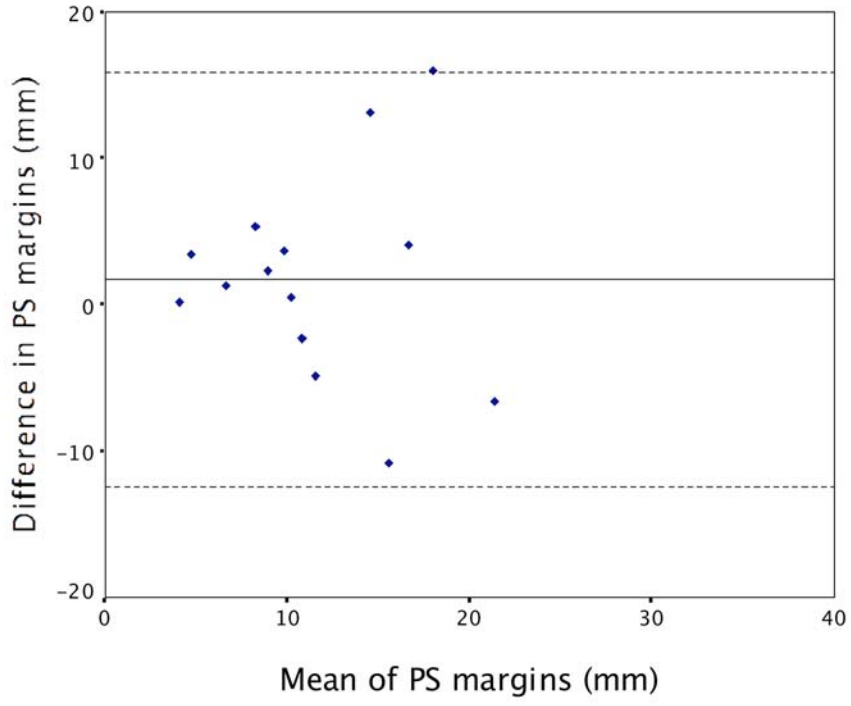

Figure 2 E

4. 4. DISCUSSION

Many adults with secundum atrial septal defects are now able to have these defects closed percutaneously. The size, location and margins of an atrial septal defect are major determining factors for transcatheter closure. Conventional assessment pre-closure has been with transoesophageal echocardiography (TOE) for measurement of ASD dimensions and margins (Cao et al. 2000; Cooke et al. 2001). Inclusion criteria for closure have included ASD maximum diameter of 40 mm and rims of at least 5 mm towards the IVC, SVC, right upper pulmonary vein and mitral valve (Du et al. 2002; Harper et al. 2002). However, more recently, deficiency of the margins has still allowed closure. For example, in patients with a deficient anterior superior (AS) margin, a correctly sized Amplatzer septal occluder can successfully be used with the device moulding itself around the aortic wall with minimal risk of perforation (Du et al. 2002; Harper et al. 2002). There have also been small numbers of patients with small inferior and posterior defect margins (<5mm) who have been successfully closed (Du et al. 2002).

While TOE has been the traditional method for the evaluation and screening for patients who are candidates for transcatheter closure, it is semi-invasive and cannot easily be performed in young children and some adults. Measurements of the ASD can only be obtained from the 4-chamber, short axis and bicaval views on TOE due to the plane on TOE that generally projects the ASD in a relatively fixed direction (Durongpisitkul et al. 2004). In addition, TOE may underestimate the size of the stretched balloon diameter of the ASD, although this has been described to factors associated with choice of plane for maximal diameter in defects that are oval rather than circular in shape, displacement of the interatrial septum from enlarged right

atrium and changes of the shape of the defect during the cardiac cycle (Cooke et al. 2001; Fischer et al. 1999). Three-dimensional echocardiography obtained from TOE images may provide superior anatomic detail (Cao et al. 2000; Zhu et al. 2000), but the accuracy of the reconstructed images is dependent on technical experience of the operator (Harper et al. 2002).

Cardiac magnetic resonance (CMR) imaging has been shown to visualise secundum ASDs (Durongpisitkul et al. 2004; Holmvang et al. 1995). Studies comparing MRI with TOE to assess ASD and suitability for percutaneous closure have mainly been done in paediatric populations (Durongpisitkul et al. 2004), although there are a limited number of small studies with adult patients (Piaw et al. 2006).

In this study, we were able to assess maximal atrial defect size in all patients with both TOE and CMR. In the assessment of atrial septal margins, CMR could assess the posterior inferior margins in all patients compared to approximately 60% that could be assessed with TOE. One recent study in a paediatric population comparing TOE and MRI assessment showed that patients who had successful closure had a significantly smaller major axis of ASD and larger posterior inferior rim compared to those who were excluded from closure procedure. An adequate posterior inferior rim was also best visualised in that study with CMR and showed a better correlation of ASD diameter measurement to balloon sizing compared to TOE (Durongpisitkul et al. 2004). However, a limitation in our study of the measurement of margins using TOE relates to this study being a retrospective study and with the images that were strictly required for measurement of the margins (such as the PI margin) not being available in some patients. Hence the 60% assessibility for the PI margin is not a true reflection of the ability of TOE to define this margin.

Although velocity encoded contrast cine imaging was not performed in this study, this is another CMR technique that can provide further information in the assessment of atrial septal defects. It enables an accurate assessment of shunt magnitude from measuring flow in the systemic and pulmonary circulations (Brenner et al. 1992; Hundley et al. 1995) and provides information about the size and shape of the atrial septal defect (Holmvang et al. 1995). However, this technique has not been used for the assessment of margins due to its limited spatial resolution.

CONCLUSION

CMR agrees closely with TOE assessment of atrial septal defects for percutaneous closure. In addition, it is able to assess the septal margins such as the posterior inferior margin, which is known to be difficult to assess with TOE. Potentially, CMR could be used instead of TOE for the assessment for percutaneous closure.

Chapter 5:

PERCUTANEOUS CLOSURE OF ATRIAL SEPTAL DEFECTS LEADS TO NORMALISATION OF RIGHT ATRIAL, RIGHT AND LEFT VENTRICULAR VOLUMES: VENTRICULAR INTERDEPENDENCE AND CARDIAC MAGNETIC RESONANCE IMAGING

TABLE OF CONTENTS

5. 1. INTRODUCTION

Atrial septal defects (ASDs) are the most common congenital cardiac malformation first diagnosed in adults and account for approximately 10% of all congenital heart lesions (Hoffman and Kaplan 2002; Hoffman et al. 2004). Patients with a significant shunt experience symptoms over time with effort dyspnoea seen in about 30% of patients by the third decade and in over 75% of patients by the fifth decade (Campbell 1970). The natural course of untreated atrial septal defects often leads to a shortened life expectancy compared to healthy subjects (Campbell 1970). Longstanding right heart, pulmonary arterial and venous volume overload and dilatation in the setting of an ASD may lead to the development of right heart failure, arrhythmia, thromboembolic events, pulmonary vascular obstructive disease (Campbell 1970; Jones et al. 1983; Steele et al. 1987). In adults with an ASD and chronic right atrial volume overload, there may be long-term arrhythmias which do not seem to be affected by closure of the defect (Murphy et al. 1990). In patients aged greater than 40 years with atrial septal defects closed surgically, 60% of these patients develop atrial arrhythmias late after surgery (Berger et al. 1999). This may be contributed by chronic right atrial stretch which causes electrophysiological alterations that persist beyond ASD closure (Morton et al. 2003).

Surgical repair of atrial septal defects has previously been shown to have excellent results in both medium and long term studies (Roos-Hesselink et al. 2003). In one retrospective study of patients over 40 years of age with isolated atrial septal defects, surgical repair increased long term survival, with adjusted 10 year survival rate of 95% compared to 84% in the medically treated group (Konstantinides et al. 1995). In addition, surgical treatment prevented functional deterioration due to heart failure.

However, surgical repair is associated with significant morbidity from peri-operative complications such as pleural effusions, sepsis and pericardial tamponade (Galal et al. 1994), although the long-term outcome after surgical ASD closure at a young age is much better than surgical closure at adult age (Roos-Hesselink et al. 2003).

Many adults with secundum ASDs are now able to have these defects closed percutaneously using septal occluder devices such as with the Amplatzer Septal Occluder (ASO), a self-expanding circular double disc that has a conjoint waist containing polytetrafluoroethylene (PTFE) and a nitinol mesh. This device has become an accepted alternative to surgical repair with studies comparing ASO device closure to surgical closure showing decreased complication rates, shorter hospital stays and greater cost-effectiveness (Du et al. 2002). Percutaneous closure of atrial septal defects should reduce right heart volumes by removing left-to-right shunting and thus, lead to symptomatic improvement and increased exercise capacity (Brochu et al. 2002; Du et al. 2002; Giardini et al. 2007). However, the effects on left ventricular volumes and function are less well described. Ventricular interdependence is a described phenomenon and suggests that a left ventricular effect may well be expected post-ASD closure. Furthermore, atrial changes post-ASD closure have been poorly understood and it is unclear whether there is a significant decrease in atrial arrhythmia post-ASD closure. Thus, atrial changes post-closure may be important for understanding the risk of atrial arrhythmia post-ASD closure.

Cardiac magnetic resonance (CMR) imaging is an accurate and reproducible imaging modality for the assessment of cardiac function and volumes. Thus, we sought to use CMR to assess ventricular and atrial volumes directly to document structural changes post-ASD closure.

5. 2. METHODS

5. 2. 1. Subjects

Consecutive patients with secundum atrial septal defects diagnosed on transthoracic and transoesophageal echocardiography with significant left to right shunt (>1.5:1) underwent CMR pre-ASD closure and 6 months post- ASD closure with the Amplatzer Septal Occluder. Only patients in sinus rhythm pre-ASD closure were included.

5. 2. 2. CMR Imaging

All CMR imaging studies were performed with subjects in the supine position using a 1.5 Tesla MRI scanner (Siemens Sonata, Germany) and a phased array surface coil. For the ventricular image set, long-axis reference views were used for positioning 8 to 12 perpendicular ventricular short-axis slices from the level of the mitral valve to the left ventricular apex. Images were obtained during end-expiratory breath-hold (8 to 10 seconds) with retrospectively ECG-gated True-FISP (Fast Imaging with Steady-State Precision) sequences (Image matrix 256 X 150, field of view 380 mm, repetition time 52.05 ms, echo time 1.74 ms and flip angle 70°). Ventricular short axis slice thickness was 6 mm with intersection gaps of 4 mm, based on previous published studies (Alfakih et al. 2003; Lorenz et al. 1999). For the atrial image set, multiple contiguous slices in both short (bi-atrial) and horizontal long axis views (four chamber) were obtained through the ASD, with slice thickness of 6 mm and no intersection gap

5. 2. 3. CMR Image Analysis

Ventricular and atrial analyses were performed off-line with a proprietary software program (Argus software, Siemens Medical Solutions, Germany). For the left ventricular (LV) data set, short-axis endocardial and epicardial contours were manually traced in end-diastole (at start of R-wave) and in end-systole (smallest cavity area). Papillary muscles and trabeculations were excluded from the ventricular volume and were included if contiguous with the myocardial mass. The basal slice was selected as the slice where the blood volume was surrounded by >50% of ventricular myocardium (Alfakih et al. 2003; Lorenz et al. 1999). For the right ventricular (RV) data set, one observer manually traced the endocardial contours at end-diastole and at end-systole. The selection of the RV basal slice was based on published methods where, if the pulmonary valve was seen, only the portion of the volume below the level of the pulmonary valve was included (Alfakih et al. 2003). Both LV and RV end-diastolic and end-systolic cavity surface areas were summed up and volumes: end-diastolic (EDV) and end-systolic (ESV) estimated by multiplying with interslice intervals as per Simpson's rule. Ejection fraction (EF) was calculated as EF = (EDV-ESV)/EDV X 100 (%). LV mass = 1.05 X (epicardial volume – endocardial volume).

A true three-dimensional atrial volume assessment technique in which the endocardial borders were manually traced for both left and right atria in the horizontal long axis (four chamber) views in ventricular end-systole when atrial volume is maximal (Hauser et al. 2004). Borders of left atrium were defined as the plane of the mitral valve and the visually apparent juncture of left atrium with pulmonary veins. Borders of right atrium were defined as the plane of the tricuspid

valve and the juncture with the vena cavae. The atrial appendage was included if present on the images. Atrial volumes were calculated as a sum of atrial cavity areas with interslice intervals using a modification of Simpson's rule.

5. 2. 4. ASD device implantation

All ASDs were closed with the Amplatzer Septal occluder (AGA medical corporation). Procedures were performed under general anaesthesia with transoesophageal echocardiographic guidance and fluoroscopy. A sizing balloon was used to determine the stretched diameter of the ASD before selection and deployment of ASO device, as previously described (Harper et al. 2002). In brief, a Meditech balloon (Boston Scientific, Watertown, MA) sized 20 or 27 mm in this series is used. This balloon is inflated within the left atrium and firm continuous pressure applied to pull it into the atrial septum, using TOE guidance. The diameter at which the balloon just gets through the atrial septal defect is the stretched balloon diameter (SBD).

5. 2. 5. Follow-up MRI

Cardiac MRI was repeated at 6 months from the time of the ASD closure, with the full dataset obtained to re-assess cardiac volumes and function (see Figure 1).

5. 2. 6. Reproducibility

Intra- and inter- observer variability was assessed for the left and right atrial and ventricular parameters.

5. 2. 7. Statistical Analysis

Data is presented as mean ± standard deviation. Comparison of cardiac volumes pre- and 6 months post-ASD closure was performed with paired t testing between groups. Statistical significance was taken as $p<0.05$. Inter and intraobserver variability was assessed using the Bland and Altman method (Bland and Altman 1986) as well as intraclass correlation coefficients. The correlation calculation is a statistical method to quantify the relationship between two variables measured independently and where r=1 is taken as a perfect correlation.

5. 3. RESULTS

A total of 23 patients were included in the study with pre-ASD closure MRI studies performed (mean age 51.2 ± years, 20 females and 3 males). Two patients went on to surgical closure of their ASDs due to size of the defect and were excluded from the analysis. Follow up cardiac MRI studies were obtained in 20 patients (see Figures 1 and 2).

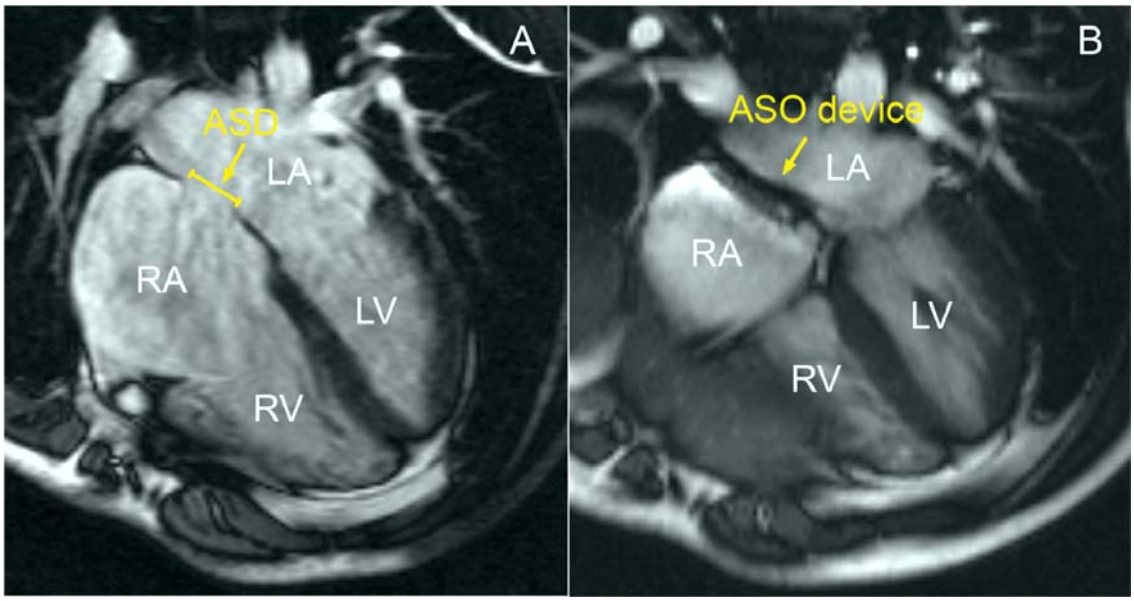

Figure 1. Four chamber CMR views showing the ASD pre- (panel A) and post-closure with the Amplatzer Septal Occluder (ASO) device (panel B). RA=right atrium, LA=left atrium, RV=right ventricle and LV=left ventricle.

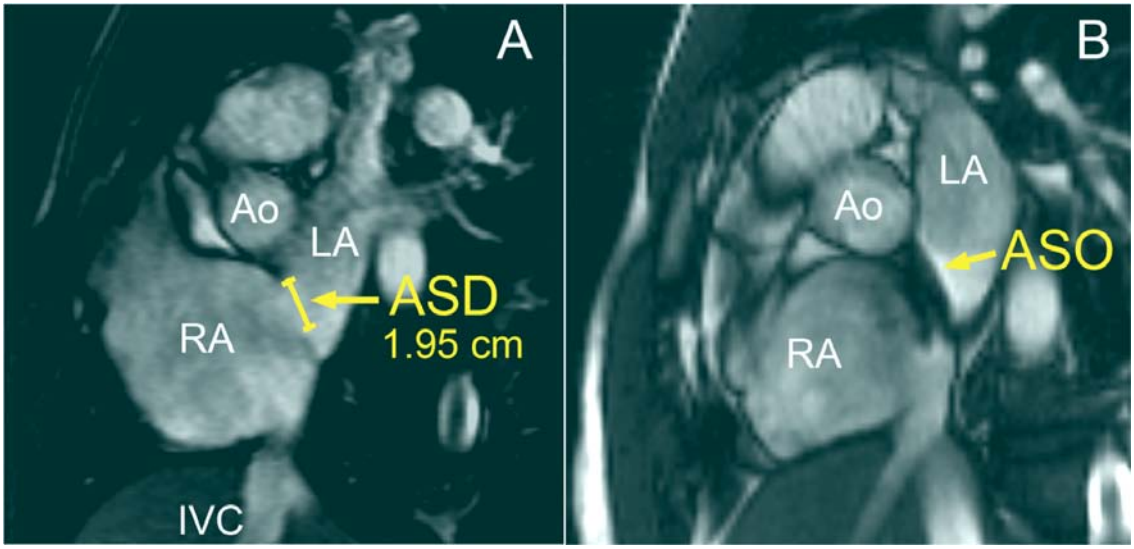

Figure 2. Bi-atrial short axis views showing the ASD (same patient as Figure 1) pre- (panel A) and post-closure with the ASO (panel B). RA=right atrium, LA=left atrium, Ao=aorta and IVC = inferior vena cava)

5. 3. 1. Atrial changes

There was a significant reduction in right atrial volumes at 6 months post-ASD closure (pre-closure 110.5 ± 55.7 vs. post-closure 90.7 ± 69.3 mls, p=0.019). There was no significant difference in left atrial volumes post-ASD closure.

5. 3. 2. Ventricular changes

There was a significant reduction in right ventricular volumes at 6 months post-ASD closure (RVEDV: 208.7 ± 76.7 vs. 140.6 ± 60.4 mls, p< 0.0001) and RVEF was significantly increased (RVEF 35.5 ± 15.5 vs. 42.0 ± 15.2 %, p= 0.025). Left ventricular volumes were significantly increased (LVEDV 84.8 ± 32.3 vs. 106.3 ±

38.1 mls, p= 0.003 and LVESV 37.4 ± 20.9 vs. 46.8 ± 18.5 mls, p=0.016). There was no significant difference in LVEF and LV mass post-ASD closure. See Table 1.

Table 1. CMR data pre and post- percutaneous ASD closure.

	Pre-closure	**Post-Closure**	**Change (%)**	**P-value**
RV EDV (mls)	208.7 ± 76.7	140.6 ± 60.4	↓ 32.6	< 0.0001
RV ESV (mls)	134.0 ± 63.7	81.6 ± 41.5	↓ 39.1	< 0.0001
RV EF (%)	35.5 ± 15.5	42.0 ± 15.2	↑18.3	0.025
LV EDV (mls)	84.9 ± 32.3	106.3 ± 38.1	↑ 25.2	0.003
LV ESV (mls)	37.3 ± 20.9	46.8 ± 18.5	↑ 25.4	0.016
LV EF (%)	61.7 ± 12.8	58.2 ± 9.0	↓ 5.7	NS
LV mass (g)	91.2 ± 29.5	103.0 ± 48.0	↑ 12.9	NS
RA vol. (mls)	110.5 ± 55.7	90.7 ± 69.3	↓ 17.9	0.019
LA vol. (mls)	84.5 ± 34.8	81.8 ± 44.2	↓ 3.2	NS

RV= right ventricle, LV = left ventricle, RA= right atrial, LA = left atrial, EDV = end-diastolic volume, ESV = end-systolic volume, EF = ejection fraction, vol.=volume, NS = non-significance.

Figure 3. shows an illustration of a reduction in RV volumes post-ASD closure associated with normalisation of LV volumes.

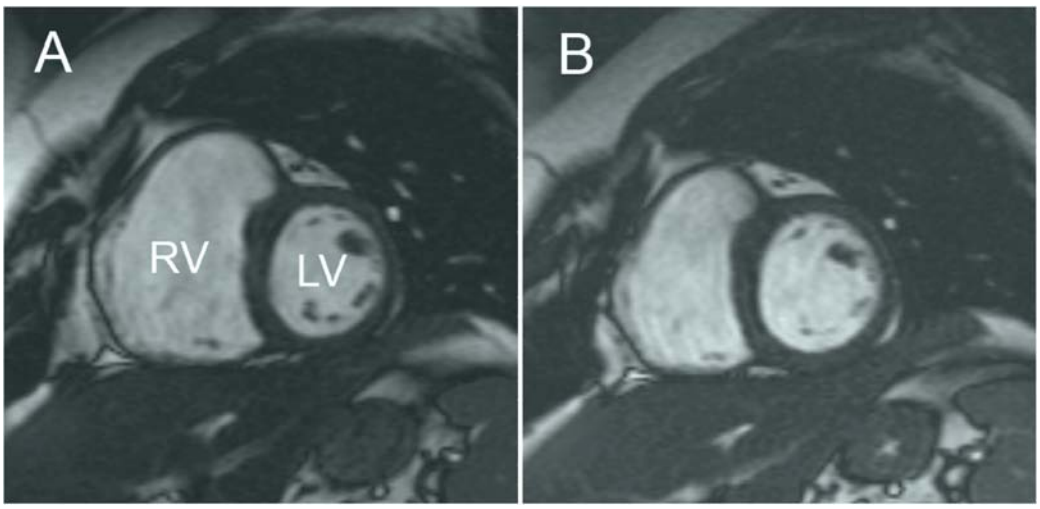

Figure 3. Short axis views of the left (LV) and right (RV) ventricles pre- (panel A) and post-ASD closure (panel B). There was a significant reduction in RV volumes post-ASD closure associated with normalisation of LV volumes.

Indexed right ventricular volumes (to body surface area) pre-ASD closure were greater than aged-matched controls at baseline (RV EDV/BSA 130.1±23.8 vs. 65.9 ±15.9, p<0.0001 and RV ESV/ BSA 77.7±31.1 vs. 33.9±24.1, p<0.0001), but were not significantly different to aged-matched controls post-ASD closure (RV EDV/BSA 84.6±36.3 vs. 65.9±15.9, p=0.06 and RV ESV/BSA 47.6±24.1 vs. 33.9± 16.5, p=0.07). Indexed left ventricular volumes and mass were not significantly different to aged-matched controls pre- or post- ASD closure. See Table 2.

Table 2. Comparison of indexed RV and LV volumes to aged-matched controls

	Pre-closure (ml/m^2)	**Post-closure (ml/m^2)**	**Aged-match (ml/m^2)**	**Unpaired t-test (vs. post-closure)**
RV EDV/ BSA	130 ± 32.8	84.6 ± 36.3	65.9 ± 15.9	0.07
RV ESV/ BSA	77.7 ± 31.1	47.6 ± 24.1	33.9 ± 16.5	0.07
LV EDV/ BSA	51.8 ± 12.6	64.8 ± 16.1	59.6 ± 14.3	NS
LV ESV/ BSA	21.0 ± 10.8	26.4 ± 10.2	25.9 ± 8.1	NS

LV mass/ BSA	50.6 ± 13.4	58.6 ± 29.5	49.8 ± 9.1	NS

5. 3. 3. Reproducibility

5. 3. 3. 1. Interobserver variability

Intraclass correlation coefficients between 2 independent observers for RV and LV parameters were: RV EDV 0.93, RV ESV 0.89, LV EDV 0.96, LV ESV 0.89, LV mass 0.84, RA vol 0.92, LA vol 0.87, RV EF 0.70, LVEF 0.94. Results from the Bland and Altman analyses for interobserver variability for LV and RV are presented as mean, the difference between the means ± 2 SD (Figures 4A to F).

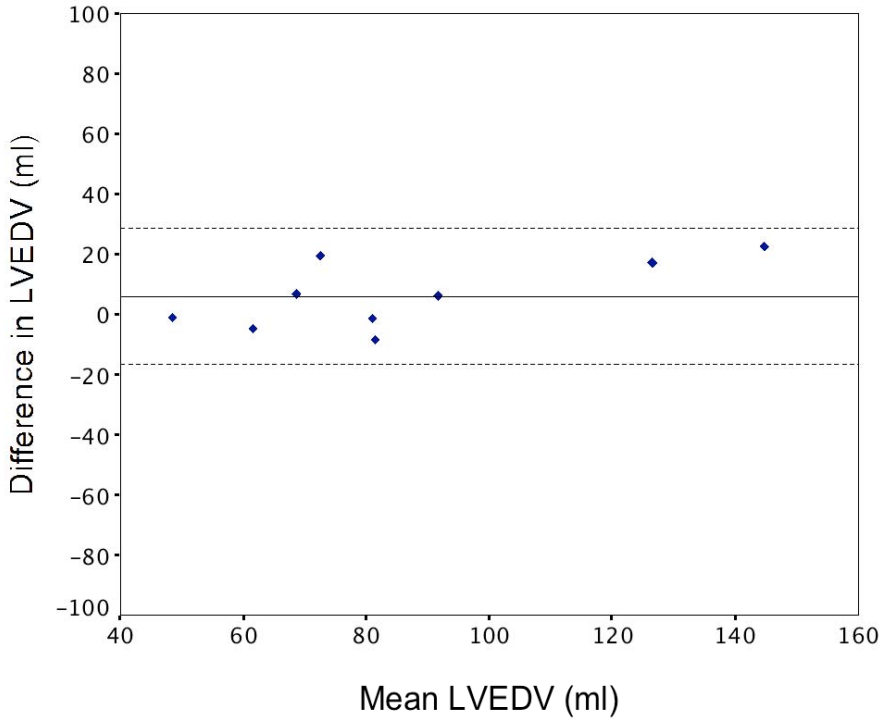

Figure 4 A. Bland Altman Analysis for interobserver LVEDV.

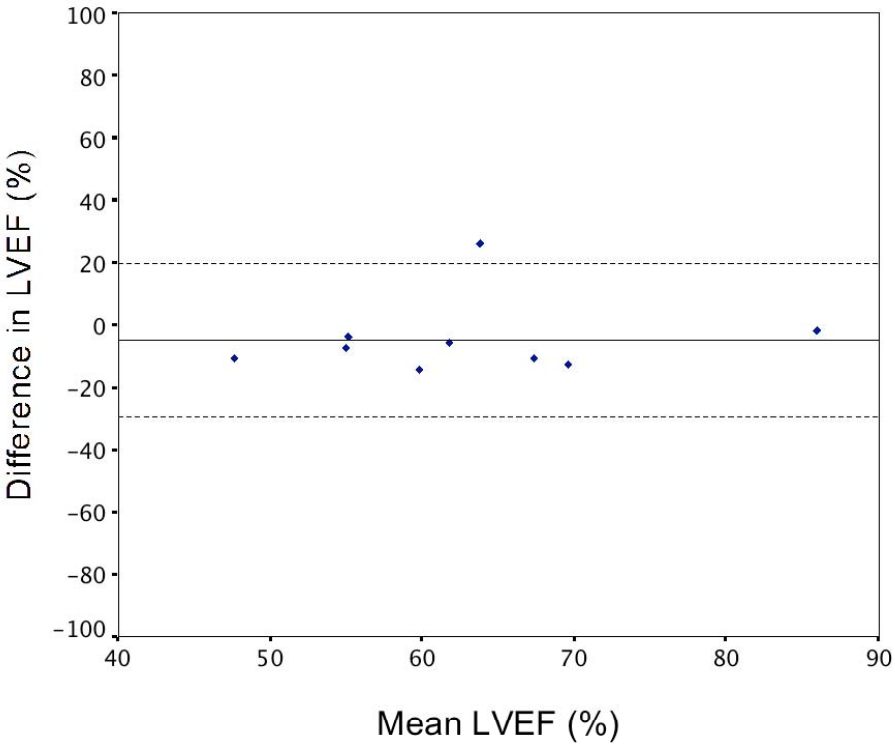

Figure 4 B. Bland Altman Analysis for interobserver LVEF.

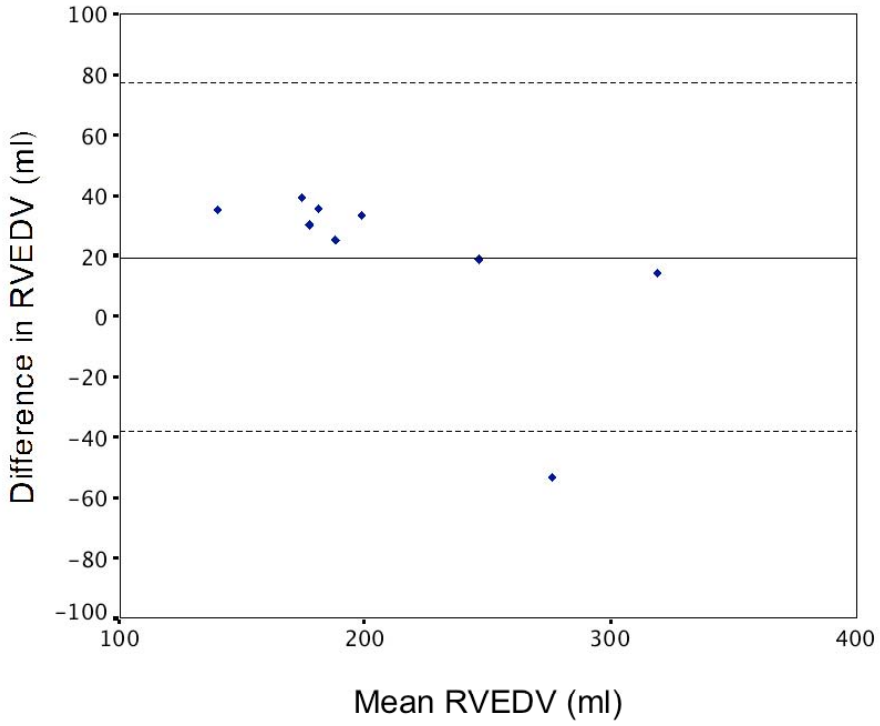

Figure 4 C. Bland Altman Analysis for interobserver RVEDV.

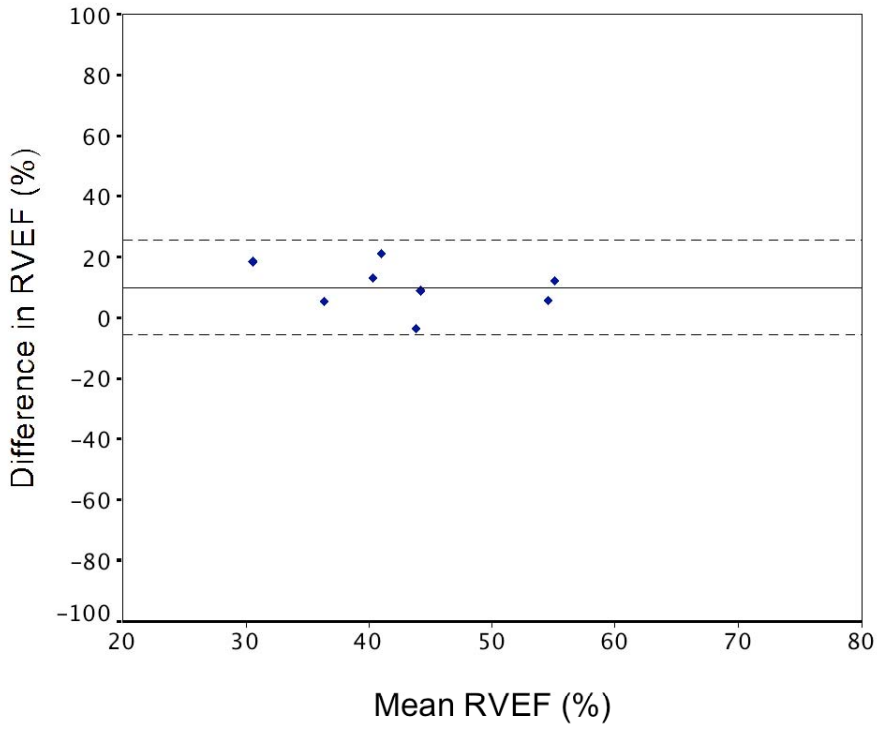

Figure 4 D. Bland Altman Analysis for interobserver RVEF.

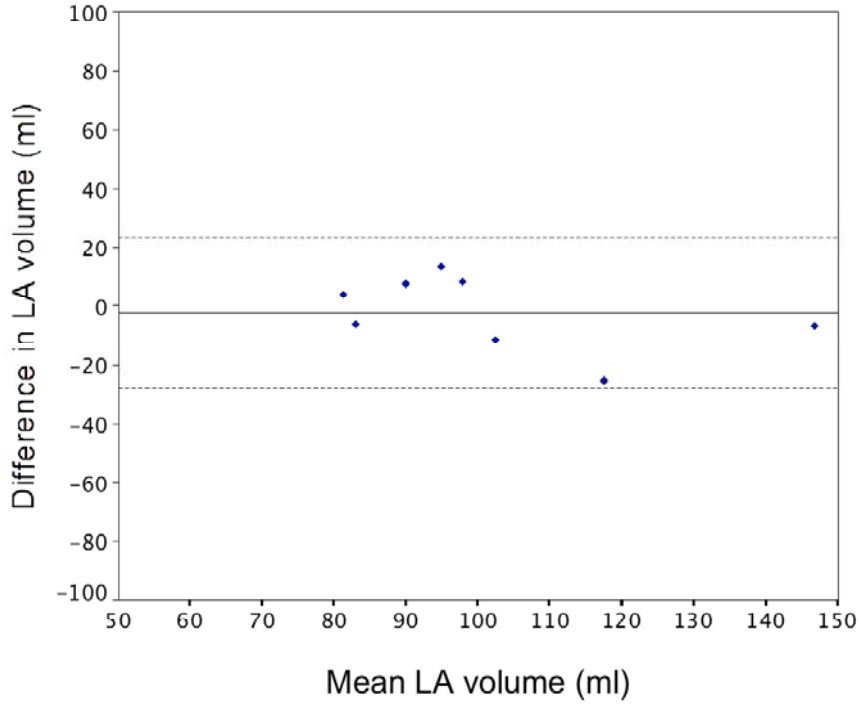

Figure 4 E. Bland Altman Analysis for interobserver LA volume.

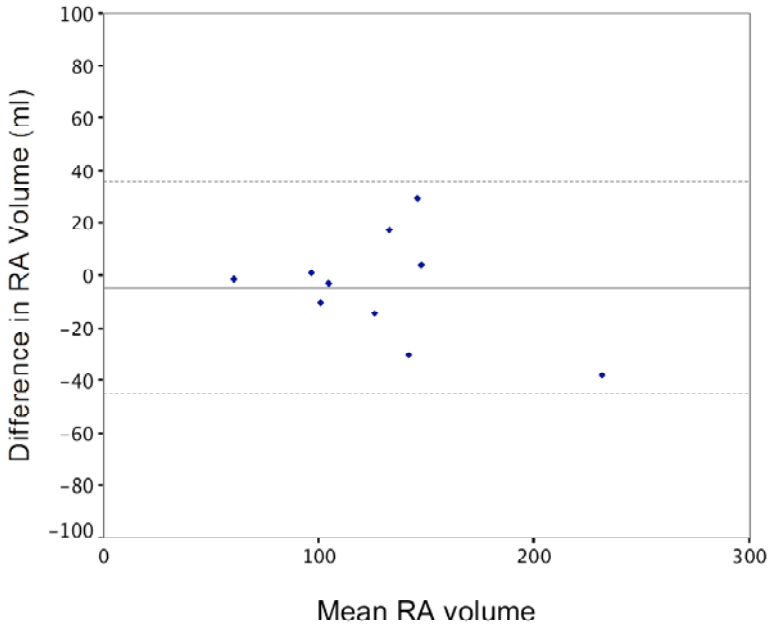

Figure 4 F. Bland Altman Analysis for interobserver RA volume.

5. 3. 3. 2. Intraobserver variability

Intraclass correlation coefficients for intraobserver variability for RV and LV parameters were RV EDV 0.89, RV ESV 0.85, LV EDV 0.95, LV ESV 0.98, RA vol 0.98, LA vol 0.84, RV EF 0.77, LV EF 0.91.

5. 4. DISCUSSION

We have shown that percutaneous ASD closure leads to a reduction in RV volumes, in association with an increase in LV volumes by CMR imaging. This was associated with an improvement in RVEF, but no change in LVEF. Furthermore, for the first time, we have seen a significant decrease in right atrial volumes post-ASD closure by CMR, but a non-significant change in left atrial volumes.

In our study, we have used cardiac magnetic resonance (CMR) imaging to obtain a full volume data set for both ventricles and atria. CMR has been shown to be safe post-cardiovascular implants (Prasad and Pennell 2004) and has become the gold standard in the assessment of left and right ventricular volumes, function and mass with excellent accuracy and reproducibility (Alfakih et al. 2003; Grothues et al. 2004; Grothues et al. 2002; Lorenz et al. 1999). Furthermore, compared to echocardiography, CMR has the advantage in the assessment of right ventricular volumes, given the non-geometric shape of the right ventricle, which makes quantification of right ventricular volume difficult by echocardiography. Previous studies on the effect of ASD closure on chamber volumes have mainly been performed using echocardiography although more recently, there have been a couple of studies that have looked at atrial and ventricular changes using CMR (Burgstahler et al. 2007; Schoen et al. 2006).

Atrial assessments of atrial dimensions using a one or two-dimensional parameter or estimation of atrial volume based on two-dimensional image algorithms have limitations. Echocardiography M-mode atrial dimension as a measure of atrial size assumes that a direct relationship between this one-dimensional measurement and atrial volume. Biplane two-dimensional echocardiography assumes an elliptical geometry of the atria (Kircher et al. 1991). These clearly are not exact, due to the variable and non-uniform geometry of the atria with significant differences demonstrated in the measurement of atrial volumes using biplane area length and biplane modified Simpson methods (Jiamsripong et al. 2007). Atrial enlargement may also be asymmetrical. CMR volume assessment of the atrium with cine imaging requires no assumptions about the geometry of the atria and has become an accepted standard for the determination of atrial volumes (Jarvinen et al. 1994; Jarvinen et al.

1996; Sievers et al. 2004). We therefore obtained a true three-dimensional atrial volume assessment technique in which the atrial borders were traced for both left and right atria in the horizontal long axis (four chamber) views in ventricular end-systole when atrial volume is maximal (Hauser et al. 2004).

ASD Closure

Echocardiography studies in adult and paediatric patients with closure of atrial septal defects have shown a reduction in right atrial areas and ventricular volumes after ASD closure both surgically (Shaheen et al. 2000) and percutaneously (Du et al. 2001; Kort et al. 2001; Schoen et al. 2006; Schussler et al. 2005; Thilen and Persson 2006; Veldtman et al. 2001). However, there is a subgroup of patients where right atrial and right ventricular sizes do not normalize. This has been reported in adult patients of 28% for RA (Thilen and Persson 2006) and 29% for RV 1 year after percutaneous closure (Veldtman et al. 2001). Persistent right atrial and ventricular enlargement is associated with higher age at closure (Du et al. 2001; Kort et al. 2001; Thilen and Persson 2006; Veldtman et al. 2001). However, even in the group of patients who had ASD closure during childhood, there was a group (>20%) with persistent RV dilatation and RA enlargement (Roos-Hesselink et al. 2003).

RV ejection fraction has been shown to decrease after surgical ASD repair. The possible causes of this were thought to include a true reduction in RV ejection fraction post-operatively, less volume overload of the right ventricle, less paradoxical septal motion or an inaccuracy in echocardiography methods for evaluating RV ejection fraction (Shaheen et al. 2000). RV systolic and diastolic function may be supra normal due to the increased pulmonary blood flow, while those of the left ventricle may be within normal range (Dhillon et al. 2002). No changes were found

in left ventricular (LV) volumes and ejection fraction in this study (Shaheen et al. 2000). Global LV function has been shown to improve after percutaneous ASD closure. In a recent study, myocardial performance index (MPI), a measure of combined systolic and diastolic function (Eidem et al. 1998) was significantly improved for both RV and LV (Salehian et al. 2005) in patients who underwent percutaneous ASD closure. The same index measured post-surgical ASD closure has been shown to be not significantly different (Eidem et al. 1998) and previous investigators have indicated that this may be contributed to by cardiopulmonary bypass (Dhillon et al. 2002; Shaheen et al. 2000), which is avoided by percutaneous closure.

Percutaneous ASD Closure

Cardiac remodelling post-ASD closure has been shown to be an early event, with reduction in right ventricular and atrial sizes occurring in the first week post-closure and that after 4 months no changes were observed (Thilen et al. 2000). Significant changes also occurred in the left ventricle, with increase in LV dimensions post-closure, but without changes in LA dimensions.

Because of its shape, quantitative echocardiographic methods to evaluate RV volumes have been difficult and thus limited to 2-D measurements. Right-sided cardiac parameters measured have included RV and RA diameters, RVOT diameters and the assessment of paradoxical septal motion (Brochu et al. 2002; Du et al. 2001; Salehian et al. 2005; Veldtman et al. 2001). Even at one month post-ASD closure, mean RV size and mean RVOT diameter was significantly reduced to within normal limits while mean right atrial length showed a trend toward shortening at one month and reached significance at 6 months (Veldtman et al. 2001). At one year, a third of

patients demonstrated persistent RV enlargement (Veldtman et al. 2001). Our data with more accurate assessment of right atrial dimensions clearly shows a volume reduction in all patients.

Closure of secundum ASD results in decreased indexed RV volume (as measured by transthoracic echocardiography) comparable to that in control subjects at 24 months following closure. However indexed RA area remained greater than in the control group. Decrease in indexed RA area over the first 12 months of follow-up was related to young age at time of closure (Kort et al. 2001).

Global LV function has been shown to improve after percutaneous ASD closure. In a recent study, myocardial performance index (MPI), a measure of combined systolic and diastolic function (Eidem et al. 1998) was significantly improved for both RV and LV (Salehian et al. 2005) in patients who underwent percutaneous ASD closure. The same index measured post-surgical ASD closure has been shown to be not significantly different (Eidem et al. 2000) and previous investigators have indicated that this may be contributed to by cardiopulmonary bypass (Dhillon et al. 2002; Shaheen et al. 2000), which is avoided by percutaneous closure. In our data set however, there was no significant change in LVEF although both LVEDV and LVESV increased.

Interventricular dependence

Ventricular interdependence has been well described in echocardiography studies and highlights the important role of the inter-ventricular septum in RV and LV function. In RV volume overload, the septum bulges into and encroaches on the LV cavity and leads to impairment of LV filling. The right ventricle is also more

compliant than the left ventricle so the left ventricle is relatively under filled. The mechanisms for decreased LV performance associated with RV volume overload include the mechanical disadvantage of a non-circular short axis configuration and changes in chamber and myocardial preload (Walker et al. 2004).

Reduced LV systolic function associated with RV volume overload has been described (Davies et al. 1970; Popio et al. 1975; Weyman et al. 1976). One echocardiographic study has reported the occurrence of adverse ventricular interdependence associated with RV volume overload in patients with ASDs (Walker et al. 2004) in which the septum bulges into and encroaches on the LV cavity and leads to impairment of LV filling. Since the right ventricle is also more compliant than the left ventricle, the left ventricle is relatively under filled. However, the reversibility of this ventricular dysfunction after elimination of the RV volume overload with surgical closure has not been consistently demonstrated (Davies et al. 1970). This may reflect surgical confounding factors that affect LV function, including pericardectomy, cardiopulmonary bypass and postoperative alterations in preload, afterload and heart rate (Walker et al. 2004).

Percutaneous device closure of the ASD avoids the confounding factors caused by surgery. In a study of 34 patients, LV ejection fraction obtained by echocardiography improved significantly from 54.9 to 62.1% ($P < 0.001$) (Walker et al. 2004).

In our study, left ventricular volumes were reduced as compared to normal values, but increased 6 months post-closure of the ASD. This is similar to a recent study which looked at left ventricular dimensions with CMR post-ASD closure (Weber et al. 2006). In addition, they found NT-proBNP concentrations were within the normal

range pre-ASD closure, but increased early after interventional closure and was associated with the increase in left ventricular dimensions as assessed by MRI (Weber et al. 2006).

5. 5. CONCLUSIONS

Percutaneous ASD closure leads to normalisation of both RV and LV volumes using CMR. With a true volumetric CMR technique, we note that RA volume reduces significantly although the small LA volume reduction was not significant. This may have important implications for future risk of atrial arrhythmogenicity.

Chapter 6

COMBINATION HIGH-DENSITY LIPOPROTEIN INFUSION AND ATORVASTATIN SIGNIFICANTLY REDUCES EXPERIMENTAL ATHEROSCLEROSIS COMPARED TO EITHER THERAPY ALONE: SERIAL ANALYSIS WITH HIGH-RESOLUTION MRI

TABLE OF CONTENTS

6. 1. INTRODUCTION

Atherosclerotic diseases and its thrombotic cardiovascular complications continue to be a leading cause of mortality (Worthley et al. 2000). Lipid lowering therapy with statins has significant benefit on cardiovascular diseases and mortality in both primary and secondary prevention clinical trials (Group 1998; Group 1994; Sacks et al. 1996). Statins reduce both cardiovascular events and the progression of atherosclerosis through a reduction in low density lipoprotein (LDL) cholesterol (2002; LaRosa et al. 2005; Nissen et al. 2004). In addition to its LDL cholesterol lowering properties, statins have been postulated to have pleiotropic effects such as reduction of the inflammatory burden (Libby 2001; Nissen et al. 2005; Sukhova et al. 2002), improved endothelial function (Hernandez-Perera et al. 1998; Jarvisalo et al. 1999) and reduced thrombogenecity (Dangas et al. 1999; Rauch et al. 2000). In human studies, statin therapy also results in the regression and stabilization of lipid-rich plaques (Callister et al. 1998; Corti et al. 2001; Crisby et al. 2001). The ASTEROID trial, a multicenter, intravascular ultrasound (IVUS) study assessed coronary atheroma at baseline and after 2 years of very high-intensity statin therapy with rosuvastatin achieved a mean reduction of 53% of LDL-cholesterol from baseline and increased HDL-C by 15% and resulted in significant regression of atherosclerosis (Nissen et al. 2006).

There is evidence that increasing HDL cholesterol levels is beneficial with an inverse relationship seen between levels of HDL cholesterol (HDL-C) and the risk of cardiovascular events (Gordon et al. 1989; Manninen et al. 1988; Rubins et al. 1999). Animal studies of increasing plasma HDL-C have shown a beneficial effect (Badimon et al. 1990; Corti et al. 2004). Even a short-term infusion of HDL with apolipoprotein A-I reduced atherosclerotic lesion size (Nicholls et al. 2005) and

infusion of recombinant ApoA-I Milano produced rapid regression of atherosclerosis (Shah et al. 2001) (Soma et al. 1995). Recombinant ApoA-I Milano is a variant of apolipoprotein A-I and mimics the properties of nascent HDL (Nissen et al. 2003). In humans after an acute coronary syndrome, short-term recombinant ApoA-1 Milano infusion resulted in significant regression of atheroma burden as assessed by intravascular ultrasound (Nissen et al. 2003).

Fibric acid derivatives are proliferator-activated receptor alpha (PPAR-α) agonists that decrease triglyceride concentrations and raise HDL-cholesterol. Pre-clinical data in a rabbit model of atherosclerosis using high resolution MRI showed fenofibrate regressed atherosclerosis when compared to placebo (Corti et al. 2007). The Helsinki Heart Study, a primary prevention trial with gemfibrozil provided the first evidence of benefit of fibrate therapy and showed a 34 percent reduction in the incidence of coronary heart disease in the gemfibrozil treated group (Frick et al. 1987). This has been confirmed in VA-HIT **(**the Veterans Affairs Cooperative Studies Program High-Density Lipoprotein Cholesterol Intervention Trial), where gemfibrozil decreased the risk of coronary heart disease in patients with normal LDL-cholesterol and low HDL-cholesterol (Rubins et al. 1999).

Cholesteryl ester transfer protein (CETP) is a glycoprotein that promotes the transfer of cholesteryl esters from antiatherogenic HDLs to proatherogenic apolipoprotein B (apo B)–containing lipoproteins such as VLDLs, VLDL remnants, IDLs and LDLs. CETP inhibition may provide a powerful therapeutic approach to raising HDL levels, lowering LDL levels and reducing the development of atherosclerosis. Animal studies in rabbits, a species with naturally high levels of CETP have demonstrated that inhibiting CETP results in a marked reduction of atherosclerosis (Sugano et al.

1998). However, expression of CETP in transgenic mice, a species that is naturally deficient in this protein has shown both an increased susceptibility and protection against atherosclerosis in different models (Berard et al. 1997; Foger et al. 1999). In humans, a previous single-blind placebo-controlled study found that in subjects with low-HDL levels, CETP inhibition with torcetrapib markedly increased HDL-C levels by 61% in those also treated with atorvastatin and 46% in the non-atorvastatin group (Brousseau et al. 2004).

High-resolution magnetic resonance imaging is a safe, non-invasive technique that can be used to serially monitor the vessel wall and document atherosclerotic burden. It has been validated in animal models including rabbit models for the measurement of atherosclerotic burden and composition (Helft et al. 2001; Worthley et al. 2000; Worthley et al. 2000; Worthley et al. 2000).

The aim of this study was to analyse the effect of a statin (atorvastatin) alone and in combination with HDL infusion and compared with controls in a rabbit model of atherosclerosis using MRI of the aortic atherosclerosis as the end-point.

6. 2. METHODS

6. 2. 1. Animal Model

Aortic atherosclerosis was established in male New Zealand white rabbits (Institute of Medical and Veterinary Science, Gilles Plains, Australia) aged 12 weeks (n=12) over 17 weeks by balloon denudation (from the renal arteries to the iliac bifurcation) and cholesterol feeding with 0.2% cholesterol enriched chow (Glen-Forest Stock Feed, Western Australia). Balloon denudation was performed 1 week after

commencing the cholesterol-enriched diet. All animals consumed the high cholesterol diet for a further 16 weeks to establish extensive atheroma. The Institute of Medical and Veterinary Science Animal Ethics Committee approved the study protocol.

6. 2. 2. Isolation of HDL

HDL were isolated from pooled samples of rabbit plasma (Quality Farms of Australia, Lara, VIC, Australia) and from samples of pooled human plasma (Gribbles Pathology, Adelaide, SA, Australia) by sequential ultracentrifugation in the 1.06 to 1.21 g/ml density range as previously described (Nicholls et al. 2005). HDL was dialyzed against endotoxin free phosphate buffered saline before use.

6. 2. 3. Establishment of Experimental Atherosclerosis

Atheroma was induced in 12 rabbits by a combination of a diet containing 0.2% cholesterol-enriched chow and balloon denudation of the abdominal aorta. Balloon denudation was performed 1 week after commencing the cholesterol-enriched diet. All animals consumed the high-cholesterol diet for a further 16 weeks to establish extensive atheroma.

6. 2. 4. Experimental Protocol

At the end of the 16 weeks of cholesterol feeding, the animals entered a 12-week treatment (3 in each group) of:

1. No treatment;
2. Oral atorvastatin (Pfizer, Groton, Conn) 5 mg/kg/day mixed in the cholesterol enriched chow with 3% peanut oil; or

3. Infusions of HDL (8 mg/kg apolipoprotein A-I) twice per week; or
4. Both, oral atorvastatin and infusion of HDL.

The high cholesterol diet was continued throughout the 12-week treatment phase.

6. 2. 5. MR imaging of the abdominal aorta

The MRI protocol used was based on previously validated work (Worthley et al. 2000). The rabbits were imaged using a knee coil in a 1.5T cardiac MRI system (Siemens Sonata, Germany). Sequential axial images (3mm thick) of the aorta from the arch to the iliac bifurcation were obtained using a turbo spin echo sequence with an in-plane resolution of 350 x 350 μm (proton density weighted: TR/TE 2000/11ms; matrix 256 x 256, echo train length 9, signal averages 4, field of view 90 mm, flip angle 180°). Fat suppression and flow saturation pulses were used.

High-resolution vessel wall MR imaging of the aorta allowed analysis of the vessel wall area (VWA) and maximal wall thickness (MWT), both well validated markers of atherosclerosis (Worthley et al. 2000; Worthley et al. 2000; Worthley et al. 2000), and abdominal aortic slices (n=8 per rabbit) were compared pre and post treatment. Data is presented as mean±SEM (mm^2) and paired t testing performed.

6. 2. 6. MR imaging analysis

All images were analysed by an investigator who was blinded to the treatment status of the animals. The MR images from the same animals were matched by use of distance from the renal arteries and the iliac bifurcation for registration as previously validated (Helft et al. 2002; Helft et al. 2001; Worthley et al. 2000). Cross sectional areas of the lumen and the outer boundary of each aortic section were determined by

manual tracing with Image-Pro Plus (Media Cybernetics) by an observer who was blinded to the treatment status of the animals. From these measurements, lumen area, outer vessel area and vessel wall area (outer vessel area minus lumen area) were calculated. The outer wall was defined as the vessel wall-epicardial fat interface. The vessel wall areas of 8 contiguous abdominal aortic slices per animal were consecutively averaged.

6. 2. 7. Statistical Analysis

Paired Student's t tests were used to compare MR image-derived parameters from the same sites in the abdominal aorta at the 2 time points. To account for multiple samplings at different sites from the same rabbit, the svy;regress procedure was used (STATA 9.1, College Station TX) for each of the 2 time-points modelling atorvastatin and atorvastatin + HDL infusion. All probabilities are 2-sided and statistical significance taken as a value of $p<0.05$. All values are assessed as mean ± SEM (mm^2).

6. 3. RESULTS

Matched MR images of the abdominal aorta (8 slices per rabbit) in the same rabbits at the 2 time points were compared to assess changes in the lumen and outer vessel wall areas over time (Figure 1). Thus atherosclerotic burden using VWA and MWT were assessed.

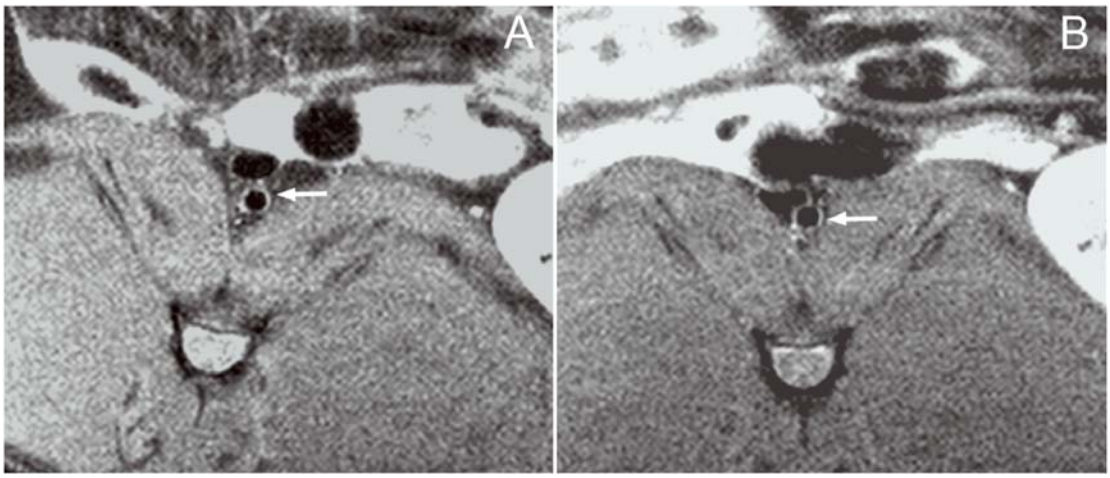

Figure 1. MRI of atherosclerotic rabbit aortas pre- (panel A) and post-treatment (panel B) with combination HDL infusion and oral atorvastatin (for 12 weeks). The post-treatment aorta is less thickened than the pre-treatment aorta (arrowed in panels B and A respectively).

6. 3. 1. Changes in vessel wall area (VWA)

There was a small, non-significant increase in VWA over the 12 weeks in the control group (6.10 ± 0.16 vs. 6.36 ± 0.72, p=NS). There were non-significant decreases in VWA in both the atorvastatin only (4.69 ± 0.14 vs. 4.45 ± 0.14, p=NS) and HDL only (5.54 ± 0.19 vs. 5.22±0.28, p=NS) groups. However, there was a significant decrease in VWA in the combination group (5.09±0.14 vs. 4.60 ± 0.15, p=0.03). See Figure 2.

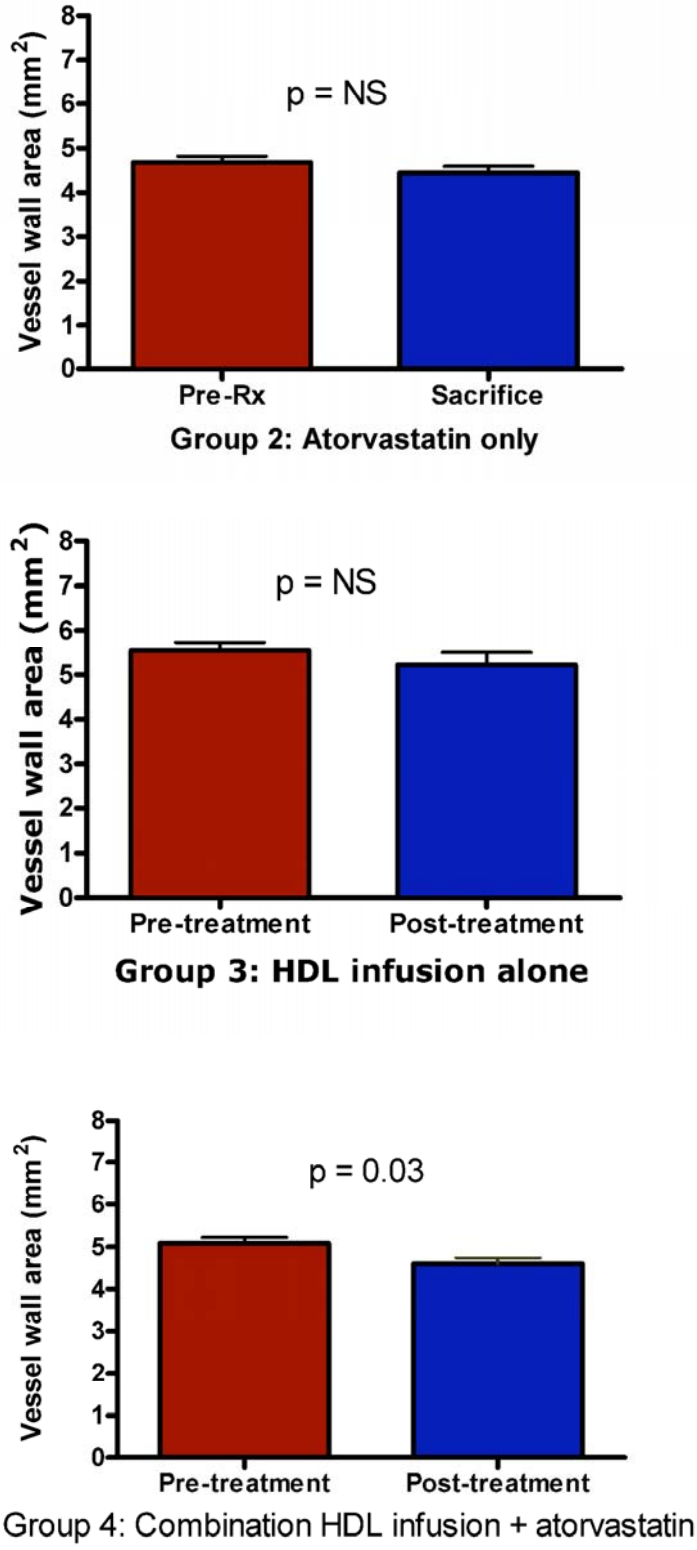

Figure 2. Graphical representation of changes in vessel wall area in the 3 treatment groups (Group 2: Atorvastatin only, Group 3 HDL infusion alone and Group 4: Combination HDL infusion plus atorvastatin). There is a non-significant decease in VWA in the atorvastatin only and HDL only groups, but there was a significant decrease in the combination group.

6. 3. 2. Changes in Maximal wall thickness

There was a significant increase in maximal wall thickness in the control group (0.86 mm ± 0.02 vs. 1.02 ± 0.04, p=0.01). There were no significant changes in maximal wall thickness in the atorvastatin only and HDL only groups. There was a significant decrease in maximal wall thickness in the groups treated with a combination of atorvastatin and HDL (0.74 ± 0.02 vs. 0.67 ± 0.02, p=0.03).

6. 4. DISCUSSION

In this study, we have compared the effects of statin therapy alone, HDL infusion alone and a combination of statin and HDL infusion on an experimental model of atherosclerosis using MRI assessment of aortic atherosclerosis. We have shown that the combination of HDL infusion and a statin (atorvastatin) is able to prevent progression and induce regression of established atherosclerotic lesions as assessed by serial MR imaging in this animal model. As expected, the control group showed a significant progression of the atherosclerotic plaque in the 12-week period. Atorvastatin or HDL infusion alone halted the progression of atherosclerosis, but did not induce regression in this study. This is most likely related to the small number of study animals and also relatively short duration of treatment. However in our study, the combination of infusion of HDL in addition to atorvastatin resulted in significant atherosclerotic plaque regression.

Lipid lowering therapy with statins has a significant beneficial effect on the incidence of cardiovascular events (Downs et al. 1998; Group 1998; Group 1994; Investigators 2002; Sacks et al. 1996; Shepherd et al. 1995) and reduces

cardiovascular mortality by 30 to 35% (Gotto 2001). Statin therapy not only results in stabilization, but also regression of previously documented human atherosclerotic lesions (Corti et al. 2001; Crisby et al. 2001; Zhao et al. 2001). There is epidemiologic evidence of strong inverse relationship between HDL cholesterol levels and cardiovascular risk (Gordon et al. 1989). The favourable effects of HDL and apoA-I have been attributed to the promotion of reverse cholesterol transport in which cholesterol from peripheral tissues including the arterial wall is transported back into the liver for reuse or excretion (Hill and McQueen 1997). HDL has also been suggested to have anti-inflammatory and anti-oxidant effects (Mackness et al. 1993). Strategies to increase HDL cholesterol have included fibric acid derivatives, HDL infusion, CETP inhibition and statin therapy. Fibric acid derivatives such as gemfibrozil and fenofibrate increase HDL cholesterol levels by 7 to 15 %. The Helsinki Heart Study (Frick et al. 1987), and the VA-HIT study (Rubins et al. 1999), demonstrated increases in HDL levels and significant reduction in cardiovascular events with gemfibrozil therapy (34% in the Helsinki Heart Study and 22% in the VA-HIT study). VA-HIT also showed a clinical benefit from raising HDL-C and reducing triglycerides without reducing LDL-cholesterol. The FIELD study is a multinational randomized controlled trial that evaluated the long-term effects of fenofibrate in patients with type 2 diabetes mellitus (Keech et al. 2005). Fenofibrate reduced total cardiovascular events from 13.9% to 12.5% or a 10% relative reduction and included a 21% reduction in coronary revascularisation. However, fenofibrate did not significantly reduce the risk of primary outcome of coronary events.

Infusion of reconstituted apoA-I Milano has been shown to promote regression of coronary atherosclerosis in humans following an acute coronary syndrome (Nissen et al. 2003). In a recent study of combined data from 4 prospective randomized

intravascular ultrasound trials of patients with coronary artery disease and on statin therapy, regression of coronary atherosclerosis was found when LDL-C was substantially reduced and HDL-C increased by greater than 7.5% suggesting that statin benefits were derived from both reductions in atherogenic lipoprotein levels and increases in HDL-C (Nicholls et al. 2007).

A previous study with a similar animal model and therapy with simvastatin and a PPAR-gamma agonist alone and in combination, but for a longer period of 6 months demonstrated that there was significant plaque regression in the group treated with simvastatin and simvastatin plus PPAR-gamma agonist, while the PPAR-gamma agonist alone resulted in a non-significant reduction in vessel wall area (Corti et al. 2004).

CETP inhibition may provide a powerful therapeutic approach to raising HDL levels, lowering LDL levels and reducing the development of atherosclerosis. The CETP inhibitor torcetrapib is effective at raising HDL cholesterol levels, however, there has been concern about the benefits and risks of torcetrapib, with a dose-dependent significant increase in blood pressure of about 3% seen in initial clinical trials (McKenney et al. 2006). The Investigation of Lipid Level Management to Understand Its Impact in Atherosclerotic Events (ILLUMINATE) study, a randomised double-blind evaluation of the effect of torcetrapib/ atorvastatin vs. atorvastatin alone on the occurrence of major cardiovascular events in subjects with coronary heart disease or risk equivalents was prematurely terminated due to an increase in observed adverse cardiovascular events (death, myocardial infarction, angina and revascularisation procedures)(Barter et al. 2007). The results of an independent parallel study, the Investigation of Lipid Level Management Using

Coronary Ultrasound to Assess Reduction of Atherosclerosis by CETP inhibition and HDL Elevation (ILLUSTRATE) trial evaluated the effect of torcetrapib-atorvastatin therapy versus atorvastatin alone on atherosclerotic burden in coronary arteries and was recently reported (Nissen et al. 2007). There was a significant increase in HDL cholesterol compared to atorvastatin monotherapy (60% relative increase) and decrease in LDL-cholesterol (20% relative decrease) after 24 months of therapy. However, there was an increase in systolic blood pressure of 4.6 mmHg and there was no significant difference in the primary end point assessing the change in percent atheroma volume in the two groups. The potential mechanisms suggested by the authors for the lack of antiatherosclerotic efficacy include the counterbalancing of beneficial effects from the increase in blood pressure, the HDL cholesterol produced by torcetrapib may be dysfunctional and that the possibility remains that CETP inhibition will not provide antiatherosclerotic benefits (Nissen et al. 2007).

6. 5. CONCLUSION

The infusion of small amounts of HDL provided incremental regression of atherosclerosis to atorvastatin using MRI in this rabbit model. This confirms the added benefits of HDL modification atop statin therapy in atherosclerotic disease. This provides further support to the role of HDL modification in the setting of current best management of patients with and at risk of coronary heart disease, and further work is required to better understand the type of HDL modifications that provide the best atheroprotection.

Chapter 7:

MULTI-DETECTOR CT IMAGING FAILS TO ACCURATELY QUANTIFY VESSEL WALL CALCIFICATION: ANALYSIS OF MULTIPLE ALGORITHMS AND COMPARISON WITH MICRO-CT

TABLE OF CONTENTS

7. 1. INTRODUCTION

Atherosclerotic diseases and its thrombotic cardiovascular complications continue to be a leading cause of mortality (Worthley et al. 2000). The high-risk or vulnerable coronary plaque that is prone to rupture has been described in several pathological studies as having a large atheromatous lipid core that is rich in inflammatory cells including macrophages with an overlying thin fibrous cap (Burke et al. 1997; Falk 1983; Virmani et al. 2006; Virmani et al. 2003).

Vascular calcification is a strong indicator of atherosclerosis, and its extent directly relates to the overall burden of atherosclerotic disease (Rumberger et al. 1995), but its effect on plaque instability is less evident (Virmani et al. 2006). It represents a potential predictor of risk for acute coronary events in selected patient populations. In addition, patients with more plaque calcification have been shown to be less likely to undergo changes in the amount of atheroma in response to medical therapies (Nicholls et al. 2007). However, not only is the extent of calcification a factor, but also the location and morphologic appearance (Nicholls et al. 2007). Calcium has been reported to be common in plaque rupture and less common in plaque erosion in histopathological studies. Non-calcified atherosclerotic plaque, which may have microcalcification below the threshold of detection with calcium scoring techniques on Computed Tomography (CT), may be unstable and more prone to rupture. Microcalcification deposits in the shoulder region of atheroma are associated with an increased risk of fibrous cap rupture and subsequent ischaemic events (Ehara et al. 2004; Fujii et al. 2005; Nicholls et al. 2007). Ehara et al. in their study with intravascular ultrasound, found that the average length of each calcium deposit in patients with either acute myocardial infarction or unstable angina pectoris was significantly smaller than in stable angina pectoris with a significant difference in the

pattern of coronary calcifications at the culprit lesion segment (Ehara et al. 2004). One hypothesis for the rupture of thin fibrous cap atheroma is that microcalcification (10 μm in diameter) in the cap, which has been undetected by in vivo imaging techniques causes local stress-induced debonding (Vengrenyuk et al. 2006).

Multi-detector CT (MDCT) has been used to quantify coronary calcification, but is limited by partial volume effects or blooming artifacts from excessive calcification which limit the diagnostic accuracy of the technique for assessing stenotic severity. The apparent volume of calcific areas is larger on CT and calcification has been identified as the underlying reason for overestimation of coronary lumen obstruction in false positive findings with 16-detector MDCT (Hoffmann et al. 2004). Even with the newer 64-detector MDCT scanners, the ability to quantify the grade of luminal obstruction is limited (Leber et al. 2005; Leschka et al. 2005). Despite several algorithms and kernels (Busch et al. 2007; Seifarth et al. 2005), the blooming artifact associated with calcification remains an issue.

In this study, we assessed the accuracy of quantification of atherosclerotic calcification with MDCT in the carotid arteries of patients undergoing carotid endarterectomy, and sought to identify algorithms or techniques that may improve quantification of calcification. This would potentially lead to an improvement in the ability of MDCT techniques to quantify stenotic severity in coronary arteries that were calcified. To achieve this, we utilised MDCT in vivo and in comparison with carotid endarterectomy specimen micro-CT. As the carotid arteries are larger and subject to less motion than the coronary circulation, we sought to evaluate the burden of calcification in carotid atherosclerotic lesions using in vivo carotid MDCT. In addition, we compared the findings on MDCT with endarterectomy specimen micro-

CT to assess the frequency of microcalcification. We sought to identify algorithms or techniques that may improve quantification of calcification. This would potentially lead to an improvement in the ability of MDCT techniques to quantify stenotic severity in coronary arteries that were calcified.

7. 2. METHODS

7. 2. 1. Subjects

Patients (n=24) scheduled for carotid endarterectomy underwent clinical carotid MDCT (Siemens Sensation-16). The endarterectomy specimens were then imaged *ex vivo* with micro-CT (Skyscan) with an in-plane resolution of 5 microns. MDCT images were analysed for calcium volume with 3 different methods (1) coronary calcium software (2) Hounsfield unit threshold-based editing software (Siemens) and (3) manual tracing with Image Pro Plus. Micro-CT images were analysed with CT-An (Skyscan). Data is presented as mean calcium volume (mm^3±SD) and simple linear regression and Bland-Altman analysis performed between the different methods.

7. 2. 2. MDCT image acquisition

MDCT data were acquired with a 16-detector MDCT scanner (Sensation 16, Siemens Medical Solutions, Germany). MDCT imaging parameters were tube current 550 mA; tube voltage 120 kV; collimation 16 x 0.75mm, 130 effmAs and 0.5 second rotation time. A fixed kernel (B40f) and field of view of 130 mm was used.

A localising anterior/posterior tomogram was first acquired with bolus monitoring over the aortic arch used to trigger the scan. Images were obtained from the aortic arch to the circle of Willis. 100 mls of contrast agent (Isovue 370) was injected at 4

mls/second. The time to obtain each scan was 17 seconds and images were reconstructed at 1mm slices at 1 mm increment.

7. 2. 3. MDCT image analysis

MDCT images were analysed for calcium volume with 3 different methods:

7. 2. 3. 1. Traditional calcium scoring using coronary calcium software

This was calculated according to the method described by Agatston (Agatston et al. 1990) where the score was derived by placing an area of interest over each calcified carotid artery focus that had a minimal attenuation of 130 HU. The areas of calcification and the maximal attenuation within each region of interest were then measured using the coronary calcium software (Siemens Medical Solutions). A score was then calculated by multiplying the measured area by an attenuation coefficient. Images were initially analysed at a predefined window and level setting (window 700 HU and level 200 HU).

7. 2. 3. 2. Hounsfield unit threshold-based editing software

Images were loaded into 3D mulitplanar reconstruction using proprietary Hounsfield unit threshold-based editing software (Siemens, Germany) and thresholds were manually adjusted for each individual patient to obtain “seed” points for areas of calcification. The lower Hounsfield unit thresholds thus were different for each patient.

7. 2. 3. 3. Manual tracing with Image Pro Plus.

Axial CT images (reconstructed to 1mm contiguous slices) of the carotid arteries were converted off-line from DICOM to TIFF format using software (OsiriX Dicom

viewer). These images were then transferred to Image Pro Plus (MediaCybernetics) and calcified regions in both the internal carotid arteries were manually traced to obtain calcium areas. Calcium volumes were then calculated from this. Calcified areas were able to be distinguished from the contrast-filled carotid lumen due to differences in “brightness”.

7. 2. 4. Micro-CT Image acquisition

A desktop micro-CT (Skyscan 1072; Aartselaar, Belgium) was used. Carotid endarterectomy specimens, fixed in formalin were place in sealed polypropylene tubes. The carotid specimens were held in place in the tubes with polystyrene, which has X-ray absorption equivalent to air. Samples were then imaged using an unfiltered tungsten x-ray source, which was run at 80kV and 120μA. Images were collected at 0.675-degree steps through a total angle of approximately 180 degrees. Total imaging time per sample was 1 hour. Although the maximum resolution for the Skyscan 1072 is approximately 4 μm, however due to the size of carotid endarterectomy specimens, the resolution ranged from 10 to 18 μm.

7. 2. 5. Micro-CT Image analysis

Projection images were converted to tomogram using proprietary software (Skyscan ConeRec). Three-dimensional rendering of the images and data analysis was performed using CT-Analyser software (Skyscan). Non-calcified areas could not be distinguished from surrounding tissues because of comparable X-ray absorption, while calcified areas were able to be easily distinguished (figure 2).

Density histograms were generated which provided quantitative results. The lower limit for threshold was selected to exclude non-calcified tissue, while the upper limit

corresponded to the densest calcified part. The 3-D models rendered from the reconstructed cross-sections were analysed to determine calcium volume (figure 3).

7. 2. 6. Statistical analysis

All data was assessed for normality using the Kolmogorov-Smirnov statistic. Data is presented as mean calcium volume (mm^3±SD) and simple linear regression performed for normally distributed data. Bland-Altman analyses were performed between the different methods, as the most appropriate comparison of different techniques assessing the same entity (i.e. amount of vascular calcification).

7. 3. RESULTS

7. 3. 1. Subject Demographics

All 24 patients (17 males, 7 females, mean age 69 ± 8 years) completed the MDCT imaging protocol without complication. Subject demographics are shown in Table 1.

Table 1. Subject demographic information.

Age	69 ± 8 years
Gender	17 males, 7 females
Diabetes	n = 2
Non-smoker	n = 6
Smoker (current)	n = 2
Smoker (past > 1 year)	n = 16
Hypertension	n = 13
Hypercholesterolaemia	n = 18

7. 3. 2. MDCT data

Good quality carotid artery MDCT imaging was possible in all cases, and it was possible to identify the atherosclerotic process in all patients (Figures 1 and 2).

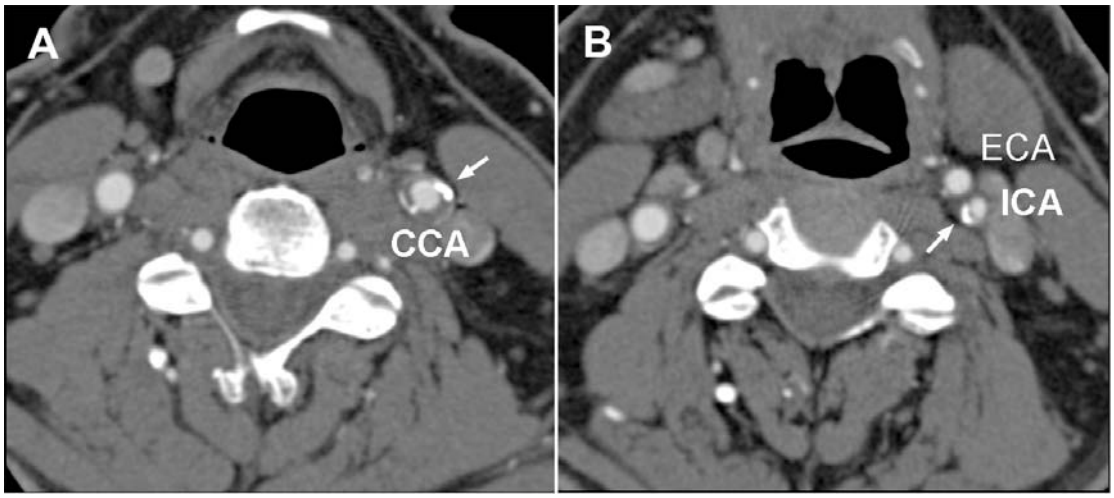

Figure 1. MDCT axial images of a patient with severe internal carotid stenosis, with calcification in the atherosclerotic lesion (arrowed). Panel A shows the calcification in the left common carotid artery (CCA) and panel B the internal (ICA) and external (ECA) carotid arteries.

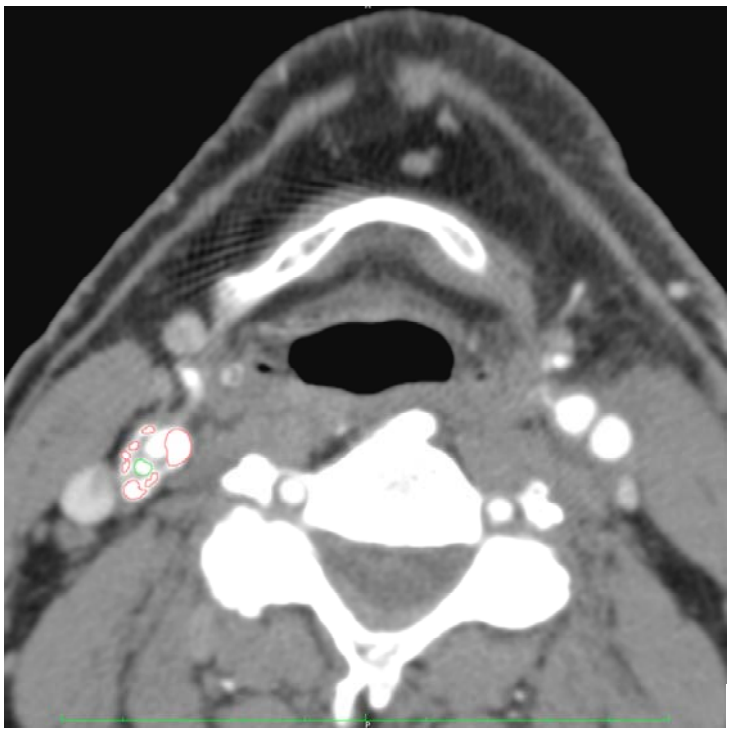

Figure 2. MDCT axial image of a patient with severe ICA stenosis. Extensive calcification (traced in red, ICA lumen traced in green) and associated "blooming" artefact of the calcification resulted in a calcium volume that was much greater than with micro-CT.

Due to inability to exclude lumen from the calcification, analysis with the coronary calcium software failed in all cases. Varying the Hounsfield unit threshold with proprietary software showed no significant relationship to calcium estimation by manual tracing, although mean values of the data set were similar (106.3±117.4 vs 122.6±146.8).

7. 3. 3. Micro-CT data

The burden of calcification by micro-CT was much less (65.9±70.11). All patients except one had significant micro-calcification by micro CT that was not discernible with *in vivo* imaging (figures 3 and 4).

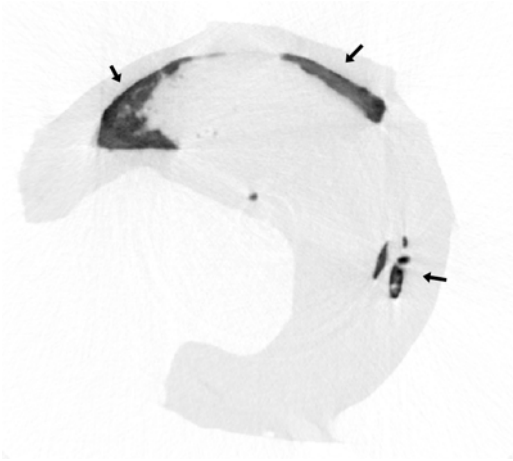

Figure 3. Example of an *ex vivo* raw axial micro-CT image of internal carotid plaque with areas of calcification (arrowed).

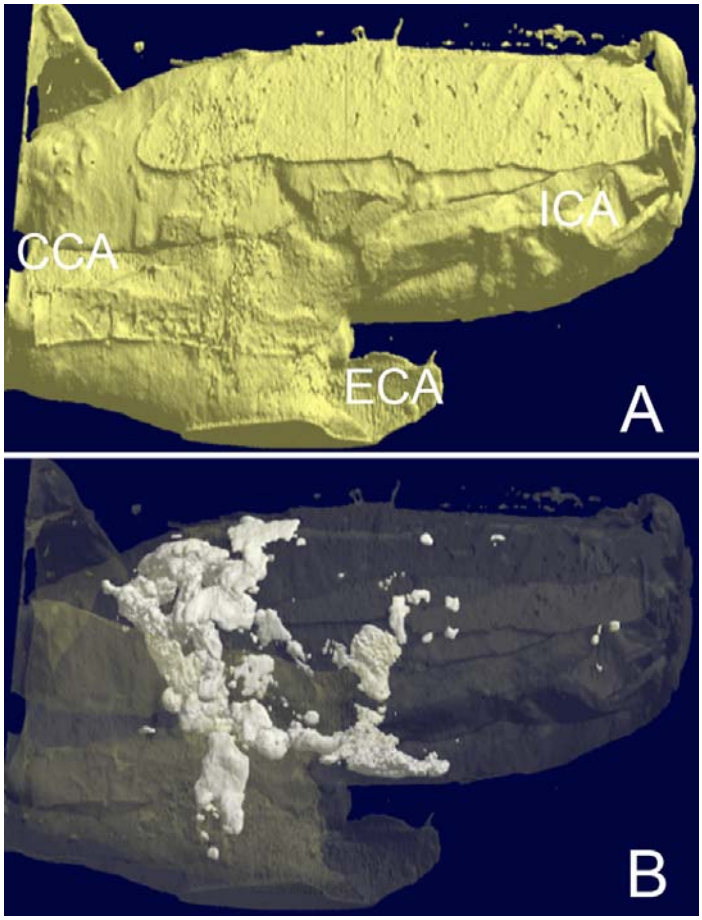

Figure 4. Panel A shows a surface-rendered 3-D reconstruction from *ex vivo* Micro-CT images of an atherosclerotic plaque with ICA (internal carotid artery), ECA (external carotid artery) and CCA (common carotid artery) shown. Panel B shows

the same plaque with the soft tissue rendering removed to reveal the extensive microcalcification.

7. 3. 4. Comparison of MDCT versus Micro-CT data

The sample data was normally distributed when assessed for normality with the Kolmogorov-Smirnov statistic test for all methods of assessing vascular calcification. Therefore, parametric testing with simple linear regression was assessed between the different methods. There was a modest but significant relationship between the *in vivo* techniques and micro-CT (Hounsfield unit threshold analysis vs. micro-CT R= 0.63, R^2= 0.40, p= 0.007; manual calcium volumes vs. micro-CT R= 0.45, R^2= 0.20, p= 0.046). However, when the more appropriate Bland Altman analyses were also performed (figure 2), it is clear that at higher calcification volumes, there is a tendency to overestimate the volume of calcification with the *in vivo* CT techniques.

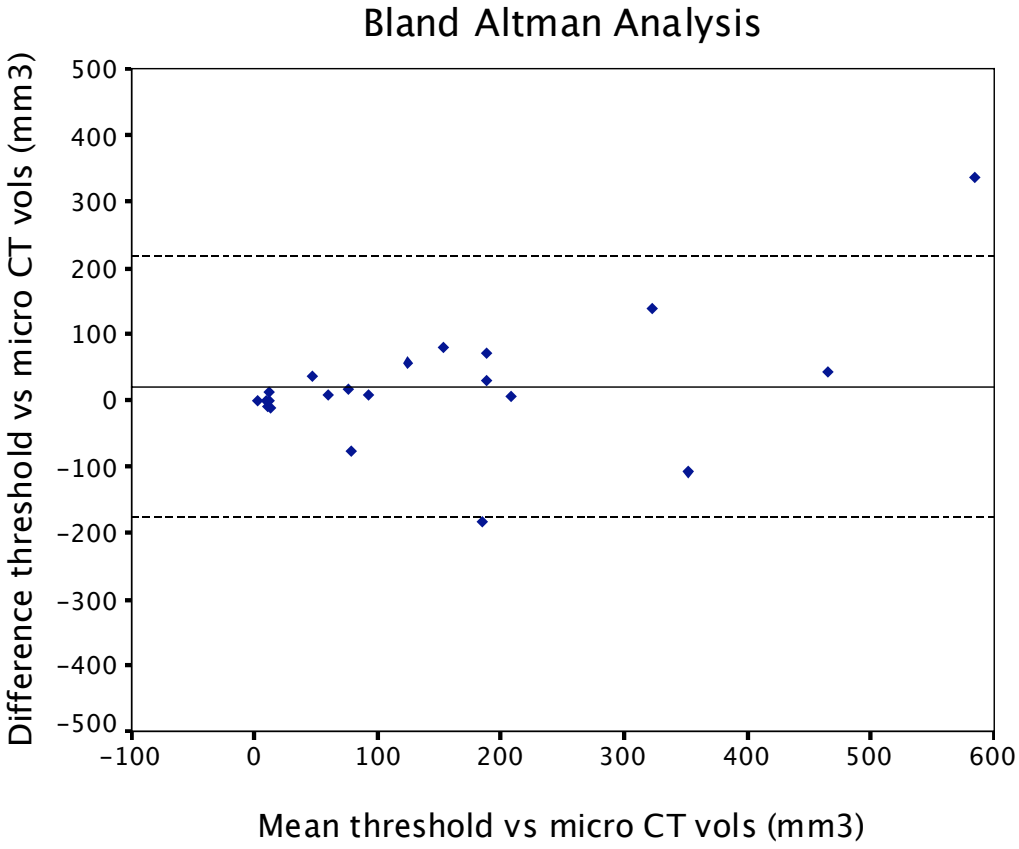

Figure 2 A

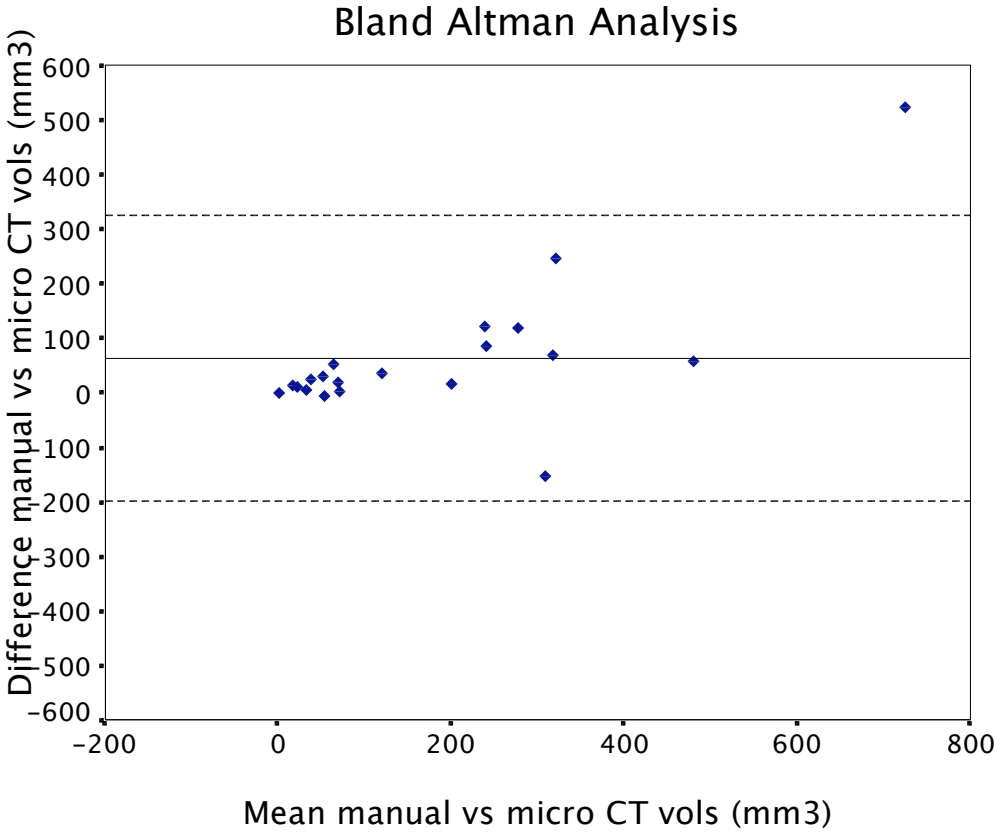

Figure 2 B

Figure 2: Bland and Altman analyses of MDCT Hounsfield unit calcium threshold (Figure 2A) and MDCT manual CT calcium volume vs micro-CT calcium volumes. Solid line indicates the mean difference and dashed lines ± 2 standard deviations (SD).

7. 4. DISCUSSION

We assessed the accuracy of quantification of atherosclerotic calcification with MDCT in the carotid arteries of patients undergoing carotid endarterectomy. We have shown that using micro-CT as a gold standard for the degree of vascular calcification, that all image analysis techniques using in vivo MDCT data overestimate the true amount of calcification, and that this over-estimation tends to be more evident with greater levels of calcification.

Vascular calcification is an important manifestation of atherosclerosis and represents a potential predictor of risk for acute coronary events in selected patient populations. Its presence is a strong indicator of atherosclerosis, and its extent directly relates to the overall burden of atherosclerotic disease (Rumberger et al. 1995). However, non-calcified atherosclerotic plaque, which may have microcalcification below the threshold of detection with calcium scoring techniques on CT, may be more unstable and more prone to rupture Microcalcification deposits in the shoulder region of atheroma are associated with an increased risk of fibrous cap rupture and subsequent ischaemic events (Ehara et al. 2004; Nicholls et al. 2007). Ehara et al. in their study with intravascular ultrasound, found that the average length of each calcium deposit in patients with either acute myocardial infarction or unstable angina pectoris was significantly smaller than in stable angina pectoris with a significant difference in the

pattern of coronary calcifications at the culprit lesion segment (Ehara et al. 2004). Small calcium deposits were significantly more frequent in the culprit lesion segments in acute coronary syndrome than in stable angina pectoris patients. Their qualitative analysis of calcifications demonstrated that the culprit segments of AMI patients were mostly characterised by small calcium deposits, associated with fibrofatty plaques and positive remodelling.

We used 3 different methods to analyse calcium volumes from the MDCT images of the carotid arteries. We found that due to inability to exclude lumen from the calcification analysis, the coronary calcium software using Agatston score and a threshold of 130 units HU for calcification, failed in all cases. With traditional calcium scoring described by Agatston (Agatston et al. 1990), software multiplies the area of a calcified plaque by an assigned coefficient selected on the basis of the highest attenuation measured in the area. There is substantial measurement variability (up to 30%) of the conventional Agatston score, which is a semi quantitative measure, and of the volume score of coronary vascular calcium (Agatston et al. 1990). There can be variation in score calculation caused by minimal variations in estimated plaque attenuation or area on serial studies and volumetric scoring has been shown to have better reproducibility (Callister et al. 1998). In addition, in our study, quantification of calcium in the carotid arteries was performed in contrast-enhanced images compared to traditional coronary artery calcium scoring that is non-contrast. A previous study has shown that after the intravenous administration of a contrast agent, noncalcified plaques can also be detected and that CT attenuation correlates well with the plaque echogenicity of ultrasound (Schroeder et al. 2001). Although there are limitations with this, combined imaging and assessment of coronary artery calcium and coronary artery stenosis (using contrast-

enhanced scan) is an attractive diagnostic approach for the management of patients with suspected coronary artery disease with reduction in radiation exposure.

The second method to quantify calcium in this study was to vary the Hounsfield unit threshold for calcification using threshold-based editing software (Siemens). This showed no significant relationship to the third method of calcium estimation by manual tracing. However, mean values of both data sets were similar.

An important factor to consider is the selection of the threshold value for calcification. A previous study by Hong et al. used a threshold of 130 HU for images obtained without contrast and used a threshold of 350 HU for CT angiography to ensure that the attenuation threshold used for calcium quantification was higher than the attenuation levels in the enhanced coronary vessels. They also used a phantom study and found that 350 HU was the lowest threshold at which actual calcium hydroxyapatite masses greater than 10 mg could be reliably detected in the phantom study (Hong et al. 2002). Nandalur et al. defined soft plaque with lipid-rich cores less than or equal to 50 HU, intermediate plaques associated with large amounts of fibrous tissue 51 to 130 HU and calcified plaques >130 HU (Nandalur et al. 2005). Leber et al. defined coronary plaques as structures >1mm^2 within the coronary artery whose density differed from that of the contrast-enhanced vessel lumen. Plaques were divided into calcified (>130 HU), non-calcified (<130 HU) and mixed lesions (if plaque area consisted of >50% of non-calcified plaque tissue). The authors rationale for choosing this definition of mixed plaques was that calcium causes blooming artifacts due to the partial volume effects that may occur in the immediate vicinity of calcium and may be confused with small areas of non-calcified tissue (Leber et al. 2003).

As calcium is decalcified during histological processing, we used micro-CT quantification of calcium as the gold standard for identifying calcium deposits within the atherosclerotic plaque (Clarke et al. 2003; Langheinrich et al. 2004). We found that the burden of calcification by micro-CT was much less compared to the calcium volumes on the MDCT images with both the manual method and the threshold-based method. However, there was no relationship between the *in vivo* techniques and micro CT. All patients except one had significant micro-calcification by micro CT that was not discernible with invivo imaging.

In a histopathological study of coronary arteries that were scanned with EBCT, the sums of histopathological plaque areas versus the sums of calcium were highly correlated for each heart and for each artery. However, coronary plaque area was five times greater than calcium area. In addition, minimal diffuse segmental coronary plaque could be present despite the absence of coronary calcium detectable by EBCT. Thus, this study confirmed the relation between whole heart, coronary artery and segmental coronary atherosclerotic plaque area and EBCT coronary calcium area, but suggested that there is a threshold value for plaque area below which calcium is either absent or not detectable by this method (Rumberger et al. 1995).

With a standard 512 x 512 matrix, pixel areas are approximately 0.34 mm^2. Criterion of 2 contiguous pixels with a CT density of >130 HU have been used in previous clinical studies. This minimal calcium area may however be too small for a consistently reproducible result in patients. Therefore, using a requirement of 3 or 4 contiguous pixels may be more reliable for clinical studies. Using these minimal amounts of discrete calcification in patients is most consistently associated with atherosclerotic plaques of >5mm^2 or larger, but cannot reliably detect plaques of smaller segmental areas.

The high-risk or vulnerable coronary plaque that is prone to rupture has been described in several pathological studies as a having a large atheromatous core with and an overlying thin fibrous cap infiltrated by macrophages (Burke et al. 1997; Falk 1983)

7. 5. CONCLUSIONS

In vivo MDCT imaging of carotid atherosclerotic calcification remains limited by spatial resolution with resulting difficulties in accurate quantification of calcification, particularly in the presence of contrast-enhanced images.

Chapter 8

DISCUSSION AND SUMMARY

In this thesis we have addressed numerous issues related to cardiac magnetic resonance and its role in both congenital and atherosclerotic cardiovascular disease. We began by defining normal ranges and reproducibility in chapter 3, and using these techniques we were able to document the ability of CMR to accurately identify cardiovascular anatomical abnormalities in atrial septal defects in Chapter 4. We have shown that these same CMR techniques provide important insights into the cardiovascular anatomical changes after percutaneous atrial septal defect closure in Chapter 5, and extends previous data in this area that has shown a normalisation of right ventricular dilatation after ASD closure, by describing the atrial remodelling that occurs. Chapter 6 moves into the field of atherosclerosis imaging, where CMR techniques have provided unique insights into the processes of atherosclerosis progression and regression, and shows us the added utility of HDL modification over statin therapy alone in regressing established atherosclerosis in a rabbit model. Finally, in Chapter 7, we move further in the field of atherosclerosis imaging to investigate an important limitation of atherosclerosis imaging with multi-detector CT imaging, namely vascular calcification. Here we show that *in vivo* carotid atherosclerosis imaging with MDCT is unable to accurately quantify the amount of calcification, especially at high calcific burdens, and by comparing this to a very high resolution CT technique (micro-CT) come to understand that this limitation is essentially one of inadequate spatial resolution. I will go over each of these findings in more detail below, and finish with the implications of the findings of this thesis, and what this leads to in the future.

In Chapter 3, we validated the accuracy and reproducibility of CMR, the main imaging modality we utilised. To achieve this, we assessed MR imaging of cardiac volumes and function in a normal adult Australian population with a specific focus on the reproducibility of the technique. In confirming that this technique in our hands is both accurate and reproducible, we are able to confidently use this technique in our future chapters. However, more than this, we established some normal ranges for left and right atrial and ventricular parameters in our local population. This is crucial background information for us in making comparisons with future studies in patients with congenital heart disease.

In Chapters 4 and 5, we explored two specific issues in one area of congenital heart disease, atrial septal defect. Atrial septal defect is the most common congenital heart defect first diagnosed in adults. The traditional method of assessment of these patients and for suitability for ASD closure involves semi-invasive investigation with transoesophageal echocardiography (TOE) for measurement of the defect size and atrial septal margins. In Chapter 4, MRI assessment of patients prior to percutaneous device closure compared to TOE assessment confirms the utility of cardiac MRI as an alternative to TOE for the work-up of these patients prior to ASD closure.

In Chapter 5, we utilised CMR to understand the effects of percutaneous ASD closure on cardiac chamber volumes. We achieved this by assessing with cardiac MRI pre-closure and post-closure atrial and ventricular cardiac volumes. Longstanding right heart dilatation in the setting of an ASD may lead to complications including right heart failure, pulmonary hypertension and arrhythmia. Closure of the ASD leads to a reduction in right heart volumes by removing left-to-right shunting and lead to normalisation of ventricular volumes. This also included

an increase in left ventricular volumes, a phenomenon related to ventricular inter-dependence. The normalisation of right atrial volume changes with ASD closure may be important in furthering our understanding in its contribution to arrhythmia, and whether or not percutaneous closure leads to a reduction in future atrial arrhythmias.

Having assessed the ability of CMR to assess both the ASD dimensions, and therefore suitability for percutaneous closure, as well as the effects of ASD closure on cardiac chamber size, in the final two original research chapters 6 and 7, we looked at another area of research development with these high-resolution imaging technologies, atherosclerosis imaging. Two particular areas we focused on included the potential of high-resolution MR imaging to monitor effects of HDL infusion on atherosclerosis, and secondly to explore mechanisms behind limitations in MDCT imaging of atherosclerosis, specifically calcification and blooming artefacts.

For assessing the effects of HDL infusion on atherosclerosis, we utilised a cholesterol-fed rabbit model of atherosclerosis. The abdominal aorta of the rabbit is comparable in size to the human coronary artery. Previous work with the rabbit model of atherosclerosis and magnetic resonance imaging of the aortic wall has shown that it can provide information about atherosclerotic composition as well as provide serial data of the arterial wall. While high intensity lipid lowering with statins remains the first line management of at risk individuals, modest manipulations of serum HDL levels are associated with a significant impact on cardiovascular risk. We showed that HDL infusion, in combination with atorvastatin, was superior to either therapy alone in a rabbit model of using MRI of aortic atherosclerosis as the end-point. This highlights the importance of modifying more than just the LDL-cholesterol in patients with and at risk of cardiovascular events.

In our fifth and final original research chapter, we assessed the accuracy of quantification of atherosclerotic calcification with MDCT in the carotid arteries of patients undergoing carotid endarterectomy, and sought to identify algorithms or techniques that may improve quantification of calcification. This would potentially lead to an improvement in the ability of MDCT techniques to quantify stenotic severity in coronary arteries that were calcified. To achieve these we utilised MDCT in vivo and in comparison with carotid endarterectomy specimen micro-CT and of course histopathology. Importantly, as part of this study, we undertook a thorough assessment of reproducibility of these techniques. We however, confirmed the inability of MDCT to accurately estimate the burden of calcification in the carotid arteries of these patients, especially those with a higher calcific burden. Thus future improvements in spatial resolution will be required in order to improve atherosclerosis imaging with MDCT.

Thus, in summary, we have been able to confirm the accuracy and reproducibility of CMR and MDCT in the areas of a specific congenital defect (ASD) and atherosclerosis imaging, and utilised these techniques to advance our understanding of these disease states. This thesis identifies strengths and weaknesses of these techniques that will allow us to more appropriately use them for future purposes in cardiovascular disease. Future work directly stemming from this thesis has already begun, and now looks to address issues of whether CMR and MDCT may provide complimentary information about atherosclerotic lesions that may benefit outcomes in certain conditions. Specifically the work in this thesis has led to studies commencing in carotid atherosclerosis and saphenous vein graft atherosclerosis and using these imaging techniques to potentially predict adverse future outcomes.

REFERENCES

Agatston, A. S., Janowitz, W. R., Hildner, F. J., et al. Quantification of coronary artery calcium using ultrafast computed tomography. J Am Coll Cardiol. 1990: 15(4): 827-32.

Alfakih, K., Plein, S., Thiele, H., et al. Normal human left and right ventricular dimensions for MRI as assessed by turbo gradient echo and steady-state free precession imaging sequences. J Magn Reson Imaging. 2003: 17(3): 323-9.

Anderson, K. M., Odell, P. M., Wilson, P. W., et al. Cardiovascular disease risk profiles. Am Heart J. 1991: 121(1 Pt 2): 293-8.

Arad, Y., Spadaro, L. A., Goodman, K., et al. Prediction of coronary events with electron beam computed tomography. J Am Coll Cardiol. 2000: 36(4): 1253-60.

Arad, Y., Spadaro, L. A., Roth, M., et al. Treatment of asymptomatic adults with elevated coronary calcium scores with atorvastatin, vitamin C, and vitamin E: the St. Francis Heart Study randomized clinical trial. J Am Coll Cardiol. 2005: 46(1): 166-72.

Assmann, G., Cullen, P. and Schulte, H. Simple scoring scheme for calculating the risk of acute coronary events based on the 10-year follow-up of the prospective cardiovascular Munster (PROCAM) study. Circulation. 2002: 105(3): 310-5.

Australian Institute of Health and Welfare., National Heart Foundation of Australia. and National Stroke Foundation (Australia) 2004. Heart, stroke and vascular diseases: Australian facts 2004. Canberra, ACT, Australian Institute of Health and Welfare National Heart Foundation of Australia National Stroke Foundation of Australia.

Axel, L., Goncalves, R. C. and Bloomgarden, D. Regional heart wall motion: two-dimensional analysis and functional imaging with MR imaging. Radiology. 1992: 183(3): 745-50.

Badimon, J. J., Badimon, L. and Fuster, V. Regression of atherosclerotic lesions by high density lipoprotein plasma fraction in the cholesterol-fed rabbit. J Clin Invest. 1990: 85(4): 1234-41.

Bart, B. A., Shaw, L. K., McCants, C. B., Jr., et al. Clinical determinants of mortality in patients with angiographically diagnosed ischemic or nonischemic cardiomyopathy. J Am Coll Cardiol. 1997: 30(4): 1002-8.

Barter, P. J., Caulfield, M., Eriksson, M., et al. Effects of torcetrapib in patients at high risk for coronary events. N Engl J Med. 2007: 357(21): 2109-22.

Baumgart, D., Schmermund, A., Goerge, G., et al. Comparison of electron beam computed tomography with intracoronary ultrasound and coronary angiography for detection of coronary atherosclerosis. J Am Coll Cardiol. 1997: 30(1): 57-64.

Beach, K. W., Hatsukami, T., Detmer, P. R., et al. Carotid artery intraplaque hemorrhage and stenotic velocity. Stroke. 1993: 24(2): 314-9.

Becker, C. R., Kleffel, T., Crispin, A., et al. Coronary artery calcium measurement: agreement of multirow detector and electron beam CT. AJR Am J Roentgenol. 2001: 176(5): 1295-8.

Becker, C. R., Knez, A., Ohnesorge, B., et al. Imaging of noncalcified coronary plaques using helical CT with retrospective ECG gating. AJR Am J Roentgenol. 2000: 175(2): 423-4.

Becker, C. R., Nikolaou, K., Muders, M., et al. Ex vivo coronary atherosclerotic plaque characterization with multi-detector-row CT. Eur Radiol. 2003: 13(9): 2094-8.

Beckman, J. A., Ganz, J., Creager, M. A., et al. Relationship of clinical presentation and calcification of culprit coronary artery stenoses. Arterioscler Thromb Vasc Biol. 2001: 21(10): 1618-22.

Bellenger, N. G., Burgess, M. I., Ray, S. G., et al. Comparison of left ventricular ejection fraction and volumes in heart failure by echocardiography, radionuclide ventriculography and cardiovascular magnetic resonance; are they interchangeable? Eur Heart J. 2000: 21(16): 1387-96.

Bellenger, N. G., Davies, L. C., Francis, J. M., et al. Reduction in sample size for studies of remodeling in heart failure by the use of cardiovascular magnetic resonance. J Cardiovasc Magn Reson. 2000: 2(4): 271-8.

Berard, A. M., Foger, B., Remaley, A., et al. High plasma HDL concentrations associated with enhanced atherosclerosis in transgenic mice overexpressing lecithin-cholesteryl acyltransferase. Nat Med. 1997: 3(7): 744-9.

Berger, F., Vogel, M., Kramer, A., et al. Incidence of atrial flutter/fibrillation in adults with atrial septal defect before and after surgery. Ann Thorac Surg. 1999: 68(1): 75-8.

Bland, J. M. and Altman, D. G. Statistical methods for assessing agreement between two methods of clinical measurement. Lancet. 1986: 1(8476): 307-10.

Bonow, R. O. Identification of viable myocardium. Circulation. 1996: 94(11): 2674-80.

Bostrom, K., Watson, K. E., Horn, S., et al. Bone morphogenetic protein expression in human atherosclerotic lesions. J Clin Invest. 1993: 91(4): 1800-9.

Bots, M. L., Hoes, A. W., Koudstaal, P. J., et al. Common carotid intima-media thickness and risk of stroke and myocardial infarction: the Rotterdam Study. Circulation. 1997: 96(5): 1432-7.

Braunwald, E. and Rutherford, J. D. Reversible ischemic left ventricular dysfunction: evidence for the "hibernating myocardium". J Am Coll Cardiol. 1986: 8(6): 1467-70.

Brenner, L. D., Caputo, G. R., Mostbeck, G., et al. Quantification of left to right atrial shunts with velocity-encoded cine nuclear magnetic resonance imaging. J Am Coll Cardiol. 1992: 20(5): 1246-50.

Brindle, P., Beswick, A., Fahey, T., et al. Accuracy and impact of risk assessment in the primary prevention of cardiovascular disease: a systematic review. Heart. 2006: 92(12): 1752-9.

Brochu, M. C., Baril, J. F., Dore, A., et al. Improvement in exercise capacity in asymptomatic and mildly symptomatic adults after atrial septal defect percutaneous closure. Circulation. 2002: 106(14): 1821-6.

Brousseau, M. E., Schaefer, E. J., Wolfe, M. L., et al. Effects of an inhibitor of cholesteryl ester transfer protein on HDL cholesterol. N Engl J Med. 2004: 350(15): 1505-15.

Budoff, M. J., Shaw, L. J., Liu, S. T., et al. Long-term prognosis associated with coronary calcification: observations from a registry of 25,253 patients. J Am Coll Cardiol. 2007: 49(18): 1860-70.

Burgstahler, C., Wohrle, J., Kochs, M., et al. Magnetic resonance imaging to assess acute changes in atrial and ventricular parameters after transcatheter closure of atrial

septal defects. J Magn Reson Imaging. 2007: 25(6): 1136-40.

Burke, A. P., Farb, A., Malcom, G. T., et al. Coronary risk factors and plaque morphology in men with coronary disease who died suddenly. N Engl J Med. 1997: 336(18): 1276-82.

Burke, A. P., Kolodgie, F. D., Farb, A., et al. Healed plaque ruptures and sudden coronary death: evidence that subclinical rupture has a role in plaque progression. Circulation. 2001: 103(7): 934-40.

Burke, A. P., Taylor, A., Farb, A., et al. Coronary calcification: insights from sudden coronary death victims. Z Kardiol. 2000: 89 Suppl 2: 49-53.

Burke, A. P., Virmani, R., Galis, Z., et al. Task force #2--what is the pathologic basis for new atherosclerosis imaging techniques? Journal of the American College of Cardiology. 2003: 41(11): 1874-1886.

Burleigh, M. C., Briggs, A. D., Lendon, C. L., et al. Collagen types I and III, collagen content, GAGs and mechanical strength of human atherosclerotic plaque caps: span-wise variations. Atherosclerosis. 1992: 96(1): 71-81.

Busch, S., Johnson, T. R., Nikolaou, K., et al. Visual and automatic grading of coronary artery stenoses with 64-slice CT angiography in reference to invasive angiography. Eur Radiol. 2007: 17(6): 1445-51.

Cai, J., Hatsukami, T. S., Ferguson, M. S., et al. In vivo quantitative measurement of intact fibrous cap and lipid-rich necrotic core size in atherosclerotic carotid plaque: comparison of high-resolution, contrast-enhanced magnetic resonance imaging and histology. Circulation. 2005: 112(22): 3437-44.

Cai, J.-M., Hatsukami, T. S., Ferguson, M. S., et al. Classification of Human Carotid Atherosclerotic Lesions With In Vivo Multicontrast Magnetic Resonance Imaging. Circulation. 2002: 106(11): 1368-1373.

Callister, T. Q., Cooil, B., Raya, S. P., et al. Coronary artery disease: improved reproducibility of calcium scoring with an electron-beam CT volumetric method. Radiology. 1998: 208(3): 807-14.

Callister, T. Q., Raggi, P., Cooil, B., et al. Effect of HMG-CoA reductase inhibitors on coronary artery disease as assessed by electron-beam computed tomography. N Engl J Med. 1998: 339(27): 1972-8.

Campbell, M. Natural history of atrial septal defect. Br Heart J. 1970: 32(6): 820-6.

Cao, Q., Radtke, W., Berger, F., et al. Transcatheter closure of multiple atrial septal defects. Initial results and value of two- and three-dimensional transoesophageal echocardiography. Eur Heart J. 2000: 21(11): 941-7.

Caussin, C., Ohanessian, A., Lancelin, B., et al. Coronary plaque burden detected by multislice computed tomography after acute myocardial infarction with near-normal coronary arteries by angiography. Am J Cardiol. 2003: 92(7): 849-52.

Celermajer, D. S. Noninvasive Detection of Atherosclerosis. N Engl J Med. 1998: 339(27): 2014-2015.

Chambless, L. E., Heiss, G., Folsom, A. R., et al. Association of coronary heart disease incidence with carotid arterial wall thickness and major risk factors: the Atherosclerosis Risk in Communities (ARIC) Study, 1987-1993. Am J Epidemiol. 1997: 146(6): 483-94.

Chan, K. C., Godman, M. J., Walsh, K., et al. Transcatheter closure of atrial septal defect and interatrial communications with a new self expanding nitinol double disc device (Amplatzer septal occluder): multicentre UK experience. Heart. 1999: 82(3): 300-6.

Cheng, G. C., Loree, H. M., Kamm, R. D., et al. Distribution of circumferential stress in ruptured and stable atherosclerotic lesions. A structural analysis with histopathological correlation. Circulation. 1993: 87(4): 1179-87.

Chu, B., Hatsukami, T. S., Polissar, N. L., et al. Determination of carotid artery atherosclerotic lesion type and distribution in hypercholesterolemic patients with moderate carotid stenosis using noninvasive magnetic resonance imaging. Stroke. 2004: 35(11): 2444-8.

Chu, B., Kampschulte, A., Ferguson, M. S., et al. Hemorrhage in the atherosclerotic carotid plaque: a high-resolution MRI study. Stroke. 2004: 35(5): 1079-84.

Clarke, S. E., Hammond, R. R., Mitchell, J. R., et al. Quantitative assessment of carotid plaque composition using multicontrast MRI and registered histology. Magn Reson Med. 2003: 50(6): 1199-208.

Conroy, R. M., Pyorala, K., Fitzgerald, A. P., et al. Estimation of ten-year risk of fatal cardiovascular disease in Europe: the SCORE project. Eur Heart J. 2003: 24(11): 987-1003.

Cooke, J. C., Gelman, J. S. and Harper, R. W. Echocardiologists' role in the deployment of the Amplatzer atrial septal occluder device in adults. J Am Soc Echocardiogr. 2001: 14(6): 588-94.

Coombs, B. D., Rapp, J. H., Ursell, P. C., et al. Structure of plaque at carotid bifurcation: high-resolution MRI with histological correlation. Stroke. 2001: 32(11): 2516-21.

Corti, R., Fayad, Z. A., Fuster, V., et al. Effects of lipid-lowering by simvastatin on human atherosclerotic lesions: a longitudinal study by high-resolution, noninvasive magnetic resonance imaging. Circulation. 2001: 104(3): 249-52.

Corti, R., Fuster, V., Fayad, Z. A., et al. Lipid lowering by simvastatin induces regression of human atherosclerotic lesions: two years' follow-up by high-resolution noninvasive magnetic resonance imaging. Circulation. 2002: 106(23): 2884-7.

Corti, R., Osende, J. I., Fallon, J. T., et al. The selective peroxisomal proliferator-activated receptor-gamma agonist has an additive effect on plaque regression in combination with simvastatin in experimental atherosclerosis: in vivo study by high-resolution magnetic resonance imaging. J Am Coll Cardiol. 2004: 43(3): 464-73.

Crisby, M., Nordin-Fredriksson, G., Shah, P. K., et al. Pravastatin treatment increases collagen content and decreases lipid content, inflammation, metalloproteinases, and cell death in human carotid plaques: implications for plaque stabilization. Circulation. 2001: 103(7): 926-33.

Dangas, G., Badimon, J. J., Smith, D. A., et al. Pravastatin therapy in hyperlipidemia: effects on thrombus formation and the systemic hemostatic profile. J Am Coll Cardiol. 1999: 33(5): 1294-304.

Davies, H., Oliver, G. C., Rappoport, W. J., et al. Abnormal left heart function after operation for atrial septal defect. Br Heart J. 1970: 32(6): 747-53.

Davies, M. J., Richardson, P. D., Woolf, N., et al. Risk of thrombosis in human atherosclerotic plaques: role of extracellular lipid, macrophage, and smooth muscle cell content. Br Heart J. 1993: 69(5): 377-81.

Davlouros, P. A., Niwa, K., Webb, G., et al. The right ventricle in congenital heart disease. Heart. 2006: 92 Suppl 1: i27-38.

Dhillon, R., Josen, M., Henein, M., et al. Transcatheter closure of atrial septal defect

preserves right ventricular function. Heart. 2002: 87(5): 461-5.

Didier, D., Higgins, C. B., Fisher, M. R., et al. Congenital heart disease: gated MR imaging in 72 patients. Radiology. 1986: 158(1): 227-35.

Didier, D., Ratib, O., Beghetti, M., et al. Morphologic and functional evaluation of congenital heart disease by magnetic resonance imaging. J Magn Reson Imaging. 1999: 10(5): 639-55.

Doherty, N. E., 3rd, Seelos, K. C., Suzuki, J., et al. Application of cine nuclear magnetic resonance imaging for sequential evaluation of response to angiotensin-converting enzyme inhibitor therapy in dilated cardiomyopathy. J Am Coll Cardiol. 1992: 19(6): 1294-302.

Downs, J. R., Clearfield, M., Weis, S., et al. Primary prevention of acute coronary events with lovastatin in men and women with average cholesterol levels: results of AFCAPS/TexCAPS. Air Force/Texas Coronary Atherosclerosis Prevention Study. JAMA. 1998: 279(20): 1615-22.

Du, Z. D., Cao, Q. L., Koenig, P., et al. Speed of normalization of right ventricular volume overload after transcatheter closure of atrial septal defect in children and adults. Am J Cardiol. 2001: 88(12): 1450-3, A9.

Du, Z. D., Hijazi, Z. M., Kleinman, C. S., et al. Comparison between transcatheter and surgical closure of secundum atrial septal defect in children and adults: results of

a multicenter nonrandomized trial. J Am Coll Cardiol. 2002: 39(11): 1836-44.

Du, Z. D., Koenig, P., Cao, Q. L., et al. Comparison of transcatheter closure of secundum atrial septal defect using the Amplatzer septal occluder associated with deficient versus sufficient rims. Am J Cardiol. 2002: 90(8): 865-9.

Durongpisitkul, K., Tang, N. L., Soongswang, J., et al. Predictors of successful transcatheter closure of atrial septal defect by cardiac magnetic resonance imaging. Pediatr Cardiol. 2004: 25(2): 124-30.

Ehara, S., Kobayashi, Y., Yoshiyama, M., et al. Spotty calcification typifies the culprit plaque in patients with acute myocardial infarction: an intravascular ultrasound study. Circulation. 2004: 110(22): 3424-9.

Eidem, B. W., O'Leary, P. W., Tei, C., et al. Usefulness of the myocardial performance index for assessing right ventricular function in congenital heart disease. Am J Cardiol. 2000: 86(6): 654-8.

Eidem, B. W., Tei, C., O'Leary, P. W., et al. Nongeometric quantitative assessment of right and left ventricular function: myocardial performance index in normal children and patients with Ebstein anomaly. J Am Soc Echocardiogr. 1998: 11(9): 849-56.

Falk, E. Plaque rupture with severe pre-existing stenosis precipitating coronary thrombosis. Characteristics of coronary atherosclerotic plaques underlying fatal

occlusive thrombi. Br Heart J. 1983: 50(2): 127-34.

Falk, E., Shah, P. K. and Fuster, V. Coronary Plaque Disruption. Circulation. 1995: 92(3): 657-671.

Fayad, Z. A., Fuster, V., Fallon, J. T., et al. Noninvasive in vivo human coronary artery lumen and wall imaging using black-blood magnetic resonance imaging. Circulation. 2000: 102(5): 506-10.

Fernandez-Ortiz, A., Badimon, J. J., Falk, E., et al. Characterization of the relative thrombogenicity of atherosclerotic plaque components: implications for consequences of plaque rupture. J Am Coll Cardiol. 1994: 23(7): 1562-9.

Ferrari, V. A., Scott, C. H., Holland, G. A., et al. Ultrafast three-dimensional contrast-enhanced magnetic resonance angiography and imaging in the diagnosis of partial anomalous pulmonary venous drainage. J Am Coll Cardiol. 2001: 37(4): 1120-8.

Fieno, D. S., Jaffe, W. C., Simonetti, O. P., et al. TrueFISP: assessment of accuracy for measurement of left ventricular mass in an animal model. J Magn Reson Imaging. 2002: 15(5): 526-31.

Fischer, G., Kramer, H. H., Stieh, J., et al. Transcatheter closure of secundum atrial septal defects with the new self-centering Amplatzer Septal Occluder. Eur Heart J. 1999: 20(7): 541-9.

Fitzpatrick, L. A., Severson, A., Edwards, W. D., et al. Diffuse calcification in human coronary arteries. Association of osteopontin with atherosclerosis. J Clin Invest. 1994: 94(4): 1597-604.

Foger, B., Chase, M., Amar, M. J., et al. Cholesteryl ester transfer protein corrects dysfunctional high density lipoproteins and reduces aortic atherosclerosis in lecithin cholesterol acyltransferase transgenic mice. J Biol Chem. 1999: 274(52): 36912-20.

Frick, M. H., Elo, O., Haapa, K., et al. Helsinki Heart Study: primary-prevention trial with gemfibrozil in middle-aged men with dyslipidemia. Safety of treatment, changes in risk factors, and incidence of coronary heart disease. N Engl J Med. 1987: 317(20): 1237-45.

Fujii, K., Carlier, S. G., Mintz, G. S., et al. Intravascular ultrasound study of patterns of calcium in ruptured coronary plaques. Am J Cardiol. 2005: 96(3): 352-7.

Funabashi, N., Kobayashi, Y., Perlroth, M., et al. Coronary artery: quantitative evaluation of normal diameter determined with electron-beam CT compared with cine coronary angiography initial experience. Radiology. 2003: 226(1): 263-71.

Fuster, V., Badimon, L., Badimon, J. J., et al. The pathogenesis of coronary artery disease and the acute coronary syndromes (1). N Engl J Med. 1992: 326(4): 242-50.

Fuster, V., Badimon, L., Badimon, J. J., et al. The pathogenesis of coronary artery

disease and the acute coronary syndromes (2). N Engl J Med. 1992: 326(5): 310-8.

Fuster, V., Fayad, Z. A., Moreno, P. R., et al. Atherothrombosis and high-risk plaque: Part II: approaches by noninvasive computed tomographic/magnetic resonance imaging. J Am Coll Cardiol. 2005: 46(7): 1209-18.

Galal, M. O., Wobst, A., Halees, Z., et al. Peri-operative complications following surgical closure of atrial septal defect type II in 232 patients--a baseline study. Eur Heart J. 1994: 15(10): 1381-4.

Gatehouse, P. D. and Firmin, D. N. The cardiovascular magnetic resonance machine: hardware and software requirements. Herz. 2000: 25(4): 317-30.

Gertz, S. D. and Roberts, W. C. Hemodynamic shear force in rupture of coronary arterial atherosclerotic plaques. Am J Cardiol. 1990: 66(19): 1368-72.

Geva, T., Vick, G. W., 3rd, Wendt, R. E., et al. Role of spin echo and cine magnetic resonance imaging in presurgical planning of heterotaxy syndrome. Comparison with echocardiography and catheterization. Circulation. 1994: 90(1): 348-56.

Giardini, A., Donti, A., Specchia, S., et al. Long-term impact of transcatheter atrial septal defect closure in adults on cardiac function and exercise capacity. Int J Cardiol. 2007.

Giesler, T., Baum, U., Ropers, D., et al. Noninvasive visualization of coronary

arteries using contrast-enhanced multidetector CT: influence of heart rate on image quality and stenosis detection. AJR Am J Roentgenol. 2002: 179(4): 911-6.

Gordon, D. J., Probstfield, J. L., Garrison, R. J., et al. High-density lipoprotein cholesterol and cardiovascular disease. Four prospective American studies. Circulation. 1989: 79(1): 8-15.

Gotte, M. J., Germans, T., Russel, I. K., et al. Myocardial strain and torsion quantified by cardiovascular magnetic resonance tissue tagging: studies in normal and impaired left ventricular function. J Am Coll Cardiol. 2006: 48(10): 2002-11.

Gotto, A. M., Jr. Statin therapy: where are we? Where do we go next? Am J Cardiol. 2001: 87(5A): 13B-18B.

Greenland, P., LaBree, L., Azen, S. P., et al. Coronary artery calcium score combined with Framingham score for risk prediction in asymptomatic individuals. Jama. 2004: 291(2): 210-5.

Grothues, F., Moon, J. C., Bellenger, N. G., et al. Interstudy reproducibility of right ventricular volumes, function, and mass with cardiovascular magnetic resonance. Am Heart J. 2004: 147(2): 218-23.

Grothues, F., Smith, G. C., Moon, J. C., et al. Comparison of interstudy reproducibility of cardiovascular magnetic resonance with two-dimensional echocardiography in normal subjects and in patients with heart failure or left

ventricular hypertrophy. Am J Cardiol. 2002: 90(1): 29-34.

Group, L.-T. I. w. P. i. I. D. L. S. Prevention of cardiovascular events and death with pravastatin in patients with coronary heart disease and a broad range of initial cholesterol levels. The Long-Term Intervention with Pravastatin in Ischaemic Disease (LIPID) Study Group. N Engl J Med. 1998: 339(19): 1349-57.

Group, S. S. S. S. Randomised trial of cholesterol lowering in 4444 patients with coronary heart disease: the Scandinavian Simvastatin Survival Study (4S). Lancet. 1994: 344(8934): 1383-9.

Haider, A. W., Larson, M. G., Benjamin, E. J., et al. Increased left ventricular mass and hypertrophy are associated with increased risk for sudden death. J Am Coll Cardiol. 1998: 32(5): 1454-9.

Harper, R. W., Mottram, P. M. and McGaw, D. J. Closure of secundum atrial septal defects with the Amplatzer septal occluder device: techniques and problems. Catheter Cardiovasc Interv. 2002: 57(4): 508-24.

Hatsukami, T. S., Ross, R., Polissar, N. L., et al. Visualization of Fibrous Cap Thickness and Rupture in Human Atherosclerotic Carotid Plaque In Vivo With High-Resolution Magnetic Resonance Imaging. Circulation. 2000: 102(9): 959-964.

Hauser, T. H., McClennen, S., Katsimaglis, G., et al. Assessment of left atrial volume by contrast enhanced magnetic resonance angiography. J Cardiovasc Magn

Reson. 2004: 6(2): 491-7.

Helft, G., Worthley, S. G., Fuster, V., et al. Progression and Regression of Atherosclerotic Lesions: Monitoring With Serial Noninvasive Magnetic Resonance Imaging. Circulation. 2002: 105(8): 993-998.

Helft, G., Worthley, S. G., Fuster, V., et al. Atherosclerotic aortic component quantification by noninvasive magnetic resonance imaging: an in vivo study in rabbits. J Am Coll Cardiol. 2001: 37(4): 1149-54.

Herlong, J. R., Jaggers, J. J. and Ungerleider, R. M. Congenital Heart Surgery Nomenclature and Database Project: pulmonary venous anomalies. Ann Thorac Surg. 2000: 69(4 Suppl): S56-69.

Hernandez-Perera, O., Perez-Sala, D., Navarro-Antolin, J., et al. Effects of the 3-hydroxy-3-methylglutaryl-CoA reductase inhibitors, atorvastatin and simvastatin, on the expression of endothelin-1 and endothelial nitric oxide synthase in vascular endothelial cells. J Clin Invest. 1998: 101(12): 2711-9.

Higgins, C. B., Byrd, B. F., 3rd, Farmer, D. W., et al. Magnetic resonance imaging in patients with congenital heart disease. Circulation. 1984: 70(5): 851-60.

Hill, S. A. and McQueen, M. J. Reverse cholesterol transport--a review of the process and its clinical implications. Clin Biochem. 1997: 30(7): 517-25.

Hirsch, R., Kilner, P. J., Connelly, M. S., et al. Diagnosis in adolescents and adults with congenital heart disease. Prospective assessment of individual and combined roles of magnetic resonance imaging and transesophageal echocardiography. Circulation. 1994: 90(6): 2937-51.

Hoffman, J. I. and Kaplan, S. The incidence of congenital heart disease. J Am Coll Cardiol. 2002: 39(12): 1890-900.

Hoffman, J. I., Kaplan, S. and Liberthson, R. R. Prevalence of congenital heart disease. Am Heart J. 2004: 147(3): 425-39.

Hoffmann, M. H., Shi, H., Manzke, R., et al. Noninvasive coronary angiography with 16-detector row CT: effect of heart rate. Radiology. 2005: 234(1): 86-97.

Hoffmann, U., Moselewski, F., Cury, R. C., et al. Predictive value of 16-slice multidetector spiral computed tomography to detect significant obstructive coronary artery disease in patients at high risk for coronary artery disease: patient-versus segment-based analysis. Circulation. 2004: 110(17): 2638-43.

Holmvang, G., Palacios, I. F., Vlahakes, G. J., et al. Imaging and sizing of atrial septal defects by magnetic resonance. Circulation. 1995: 92(12): 3473-80.

Hong, C., Becker, C. R., Schoepf, U. J., et al. Coronary artery calcium: absolute quantification in nonenhanced and contrast-enhanced multi-detector row CT studies. Radiology. 2002: 223(2): 474-80.

Hoppe, U. C., Dederichs, B., Deutsch, H. J., et al. Congenital heart disease in adults and adolescents: comparative value of transthoracic and transesophageal echocardiography and MR imaging. Radiology. 1996: 199(3): 669-77.

Huang, H., Virmani, R., Younis, H., et al. The impact of calcification on the biomechanical stability of atherosclerotic plaques. Circulation. 2001: 103(8): 1051-6.

Hudsmith, L. E., Petersen, S. E., Francis, J. M., et al. Normal human left and right ventricular and left atrial dimensions using steady state free precession magnetic resonance imaging. J Cardiovasc Magn Reson. 2005: 7(5): 775-82.

Hundley, W. G., Li, H. F., Lange, R. A., et al. Assessment of left-to-right intracardiac shunting by velocity-encoded, phase-difference magnetic resonance imaging. A comparison with oximetric and indicator dilution techniques. Circulation. 1995: 91(12): 2955-60.

Investigators, M. B. H. P. S. MRC/BHF Heart Protection Study of cholesterol lowering with simvastatin in 20,536 high-risk individuals: a randomised placebo-controlled trial. Lancet. 2002: 360(9326): 7-22.

Janowitz, W. R., Agatston, A. S., Kaplan, G., et al. Differences in prevalence and extent of coronary artery calcium detected by ultrafast computed tomography in asymptomatic men and women. Am J Cardiol. 1993: 72(3): 247-54.

Jarvinen, V. M., Kupari, M. M., Hekali, P. E., et al. Right atrial MR imaging studies of cadaveric atrial casts and comparison with right and left atrial volumes and function in healthy subjects. Radiology. 1994: 191(1): 137-42.

Jarvinen, V. M., Kupari, M. M., Poutanen, V. P., et al. Right and left atrial phasic volumetric function in mildly symptomatic dilated and hypertrophic cardiomyopathy: cine MR imaging assessment. Radiology. 1996: 198(2): 487-95.

Jarvisalo, M. J., Toikka, J. O., Vasankari, T., et al. HMG CoA reductase inhibitors are related to improved systemic endothelial function in coronary artery disease. Atherosclerosis. 1999: 147(2): 237-42.

Jauhiainen, T., Jarvinen, V. M., Hekali, P. E., et al. MR gradient echo volumetric analysis of human cardiac casts: focus on the right ventricle. J Comput Assist Tomogr. 1998: 22(6): 899-903.

Jiamsripong, P., Honda, T., Reuss, C. S., et al. Three methods for evaluation of left atrial volume. Eur J Echocardiogr. 2007.

Jones, H. R., Jr., Caplan, L. R., Come, P. C., et al. Cerebral emboli of paradoxical origin. Ann Neurol. 1983: 13(3): 314-9.

Katz, J., Milliken, M. C., Stray-Gundersen, J., et al. Estimation of human myocardial mass with MR imaging. Radiology. 1988: 169(2): 495-8.

Katz, J., Whang, J., Boxt, L. M., et al. Estimation of right ventricular mass in normal subjects and in patients with primary pulmonary hypertension by nuclear magnetic resonance imaging. J Am Coll Cardiol. 1993: 21(6): 1475-81.

Keech, A., Simes, R. J., Barter, P., et al. Effects of long-term fenofibrate therapy on cardiovascular events in 9795 people with type 2 diabetes mellitus (the FIELD study): randomised controlled trial. Lancet. 2005: 366(9500): 1849-61.

Kilner, P. J., Firmin, D. N., Rees, R. S., et al. Valve and great vessel stenosis: assessment with MR jet velocity mapping. Radiology. 1991: 178(1): 229-35.

Kilner, P. J., Manzara, C. C., Mohiaddin, R. H., et al. Magnetic resonance jet velocity mapping in mitral and aortic valve stenosis. Circulation. 1993: 87(4): 1239-48.

Kim, R. J., Chen, E. L., Lima, J. A., et al. Myocardial Gd-DTPA kinetics determine MRI contrast enhancement and reflect the extent and severity of myocardial injury after acute reperfused infarction. Circulation. 1996: 94(12): 3318-26.

Kim, R. J., Fieno, D. S., Parrish, T. B., et al. Relationship of MRI Delayed Contrast Enhancement to Irreversible Injury, Infarct Age, and Contractile Function. Circulation. 1999: 100(19): 1992-2002.

Kim, R. J., Wu, E., Rafael, A., et al. The use of contrast-enhanced magnetic resonance imaging to identify reversible myocardial dysfunction. N Engl J Med.

2000: 343(20): 1445-53.

Kircher, B., Abbott, J. A., Pau, S., et al. Left atrial volume determination by biplane two-dimensional echocardiography: validation by cine computed tomography. Am Heart J. 1991: 121(3 Pt 1): 864-71.

Knez, A., Becker, C., Becker, A., et al. Determination of coronary calcium with multi-slice spiral computed tomography: a comparative study with electron-beam CT. Int J Cardiovasc Imaging. 2002: 18(4): 295-303.

Kondo, C., Caputo, G. R., Semelka, R., et al. Right and left ventricular stroke volume measurements with velocity-encoded cine MR imaging: in vitro and in vivo validation. AJR Am J Roentgenol. 1991: 157(1): 9-16.

Kondos, G. T., Hoff, J. A., Sevrukov, A., et al. Electron-beam tomography coronary artery calcium and cardiac events: a 37-month follow-up of 5635 initially asymptomatic low- to intermediate-risk adults. Circulation. 2003: 107(20): 2571-6.

Konstantinides, S., Geibel, A., Olschewski, M., et al. A comparison of surgical and medical therapy for atrial septal defect in adults. N Engl J Med. 1995: 333(8): 469-73.

Kort, H. W., Balzer, D. T. and Johnson, M. C. Resolution of right heart enlargement after closure of secundum atrial septal defect with transcatheter technique. J Am Coll Cardiol. 2001: 38(5): 1528-32.

Kuettner, A., Trabold, T., Schroeder, S., et al. Noninvasive detection of coronary lesions using 16-detector multislice spiral computed tomography technology: initial clinical results. J Am Coll Cardiol. 2004: 44(6): 1230-7.

Kwong, R. Y., Chan, A. K., Brown, K. A., et al. Impact of unrecognized myocardial scar detected by cardiac magnetic resonance imaging on event-free survival in patients presenting with signs or symptoms of coronary artery disease. Circulation. 2006: 113(23): 2733-43.

Langheinrich, A. C., Bohle, R. M., Greschus, S., et al. Atherosclerotic lesions at micro CT: feasibility for analysis of coronary artery wall in autopsy specimens. Radiology. 2004: 231(3): 675-81.

Lardo, A. 2003. Cardiovascular magnetic resonance: established and emerging applications. London; New York Independence, KY, Martin Dunitz; Distributed in the USA by Fullfillment Center, Taylor & Francis.

LaRosa, J. C., Grundy, S. M., Waters, D. D., et al. Intensive lipid lowering with atorvastatin in patients with stable coronary disease. N Engl J Med. 2005: 352(14): 1425-35.

Law, M. R., Wald, N. J. and Morris, J. K. The performance of blood pressure and other cardiovascular risk factors as screening tests for ischaemic heart disease and stroke. J Med Screen. 2004: 11(1): 3-7.

Leber, A. W., Knez, A., Becker, A., et al. Accuracy of multidetector spiral computed tomography in identifying and differentiating the composition of coronary atherosclerotic plaques: a comparative study with intracoronary ultrasound. J Am Coll Cardiol. 2004: 43(7): 1241-7.

Leber, A. W., Knez, A., von Ziegler, F., et al. Quantification of obstructive and nonobstructive coronary lesions by 64-slice computed tomography: a comparative study with quantitative coronary angiography and intravascular ultrasound. J Am Coll Cardiol. 2005: 46(1): 147-54.

Leber, A. W., Knez, A., White, C. W., et al. Composition of coronary atherosclerotic plaques in patients with acute myocardial infarction and stable angina pectoris determined by contrast-enhanced multislice computed tomography. Am J Cardiol. 2003: 91(6): 714-8.

Leschka, S., Alkadhi, H., Plass, A., et al. Accuracy of MSCT coronary angiography with 64-slice technology: first experience. Eur Heart J. 2005: 26(15): 1482-7.

Libby, P. Current concepts of the pathogenesis of the acute coronary syndromes. Circulation. 2001: 104(3): 365-72.

Longmore, D. B., Klipstein, R. H., Underwood, S. R., et al. Dimensional accuracy of magnetic resonance in studies of the heart. Lancet. 1985: 1(8442): 1360-2.

Lopez, K., Dalvi, B. V., Balzer, D., et al. Transcatheter closure of large secundum

atrial septal defects using the 40 mm Amplatzer septal occluder: Results of an international registry. Catheter Cardiovasc Interv. 2005.

Lorenz, C. H., Walker, E. S., Morgan, V. L., et al. Normal human right and left ventricular mass, systolic function, and gender differences by cine magnetic resonance imaging. J Cardiovasc Magn Reson. 1999: 1(1): 7-21.

Lorenz, M. W., Markus, H. S., Bots, M. L., et al. Prediction of clinical cardiovascular events with carotid intima-media thickness: a systematic review and meta-analysis. Circulation. 2007: 115(4): 459-67.

Luft, A. R., Skalej, M., Welte, D., et al. Reliability and exactness of MRI-based volumetry: a phantom study. J Magn Reson Imaging. 1996: 6(4): 700-4.

Maceira, A. M., Joshi, J., Prasad, S. K., et al. Cardiovascular magnetic resonance in cardiac amyloidosis. Circulation. 2005: 111(2): 186-93.

Mackness, M. I., Abbott, C., Arrol, S., et al. The role of high-density lipoprotein and lipid-soluble antioxidant vitamins in inhibiting low-density lipoprotein oxidation. Biochem J. 1993: 294 (Pt 3): 829-34.

Mahrholdt, H., Goedecke, C., Wagner, A., et al. Cardiovascular magnetic resonance assessment of human myocarditis: a comparison to histology and molecular pathology. Circulation. 2004: 109(10): 1250-8.

Mahrholdt, H., Wagner, A., Deluigi, C. C., et al. Presentation, patterns of myocardial damage, and clinical course of viral myocarditis. Circulation. 2006: 114(15): 1581-90.

Manninen, V., Elo, M. O., Frick, M. H., et al. Lipid alterations and decline in the incidence of coronary heart disease in the Helsinki Heart Study. Jama. 1988: 260(5): 641-51.

Manning, W. J. and Pennell, D. J. 2002. Cardiovascular magnetic resonance. New York, Churchill Livingstone.

Masani, N. D. Transoesophageal echocardiography in adult congenital heart disease. Heart. 2001: 86 Suppl 2: II30-II40.

McCarthy, J. H. and Palmer, F. J. Incidence and significance of coronary artery calcification. Br Heart J. 1974: 36(5): 499-506.

McCrohon, J. A., Moon, J. C. C., Prasad, S. K., et al. Differentiation of Heart Failure Related to Dilated Cardiomyopathy and Coronary Artery Disease Using Gadolinium-Enhanced Cardiovascular Magnetic Resonance. Circulation. 2003: 108(1): 54-59.

McKenney, J. M., Davidson, M. H., Shear, C. L., et al. Efficacy and safety of torcetrapib, a novel cholesteryl ester transfer protein inhibitor, in individuals with below-average high-density lipoprotein cholesterol levels on a background of atorvastatin. J Am Coll Cardiol. 2006: 48(9): 1782-90.

Mehta, S. R., Eikelboom, J. W., Natarajan, M. K., et al. Impact of right ventricular involvement on mortality and morbidity in patients with inferior myocardial infarction. J Am Coll Cardiol. 2001: 37(1): 37-43.

Mintz, G. S., Pichard, A. D., Popma, J. J., et al. Determinants and correlates of target lesion calcium in coronary artery disease: a clinical, angiographic and intravascular ultrasound study. J Am Coll Cardiol. 1997: 29(2): 268-74.

Mintz, G. S., Popma, J. J., Pichard, A. D., et al. Patterns of calcification in coronary artery disease. A statistical analysis of intravascular ultrasound and coronary angiography in 1155 lesions. Circulation. 1995: 91(7): 1959-65.

Mohiaddin, R. H. 2002. Introduction to cardiovascular magnetic resonance. London, Current Medical Literature.

Mollet, N. R., Cademartiri, F. and de Feyter, P. J. Non-invasive multislice CT coronary imaging. Heart. 2005: 91(3): 401-7.

Moon, J. C., Reed, E., Sheppard, M. N., et al. The histologic basis of late gadolinium enhancement cardiovascular magnetic resonance in hypertrophic cardiomyopathy. J Am Coll Cardiol. 2004: 43(12): 2260-4.

Moon, J. C. C., Lorenz, C. H., Francis, J. M., et al. Breath-hold FLASH and FISP Cardiovascular MR Imaging: Left Ventricular Volume Differences and

Reproducibility. Radiology. 2002: 223(3): 789-797.

Morgan-Hughes, G. J., Roobottom, C. A., Owens, P. E., et al. Highly accurate coronary angiography with submillimetre, 16 slice computed tomography. Heart. 2005: 91(3): 308-13.

Morin, R. L., Gerber, T. C. and McCollough, C. H. Radiation dose in computed tomography of the heart. Circulation. 2003: 107(6): 917-22.

Morton, J. B., Sanders, P., Vohra, J. K., et al. Effect of chronic right atrial stretch on atrial electrical remodeling in patients with an atrial septal defect. Circulation. 2003: 107(13): 1775-82.

Murphy, J. G., Gersh, B. J., McGoon, M. D., et al. Long-term outcome after surgical repair of isolated atrial septal defect. Follow-up at 27 to 32 years. N Engl J Med. 1990: 323(24): 1645-50.

Nagel, E., Lehmkuhl, H. B., Bocksch, W., et al. Noninvasive diagnosis of ischemia-induced wall motion abnormalities with the use of high-dose dobutamine stress MRI: comparison with dobutamine stress echocardiography. Circulation. 1999: 99(6): 763-70.

Nandalur, K. R., Baskurt, E., Hagspiel, K. D., et al. Calcified carotid atherosclerotic plaque is associated less with ischemic symptoms than is noncalcified plaque on MDCT. AJR Am J Roentgenol. 2005: 184(1): 295-8.

Nicholls, S. J., Cutri, B., Worthley, S. G., et al. Impact of short-term administration of high-density lipoproteins and atorvastatin on atherosclerosis in rabbits. Arterioscler Thromb Vasc Biol. 2005: 25(11): 2416-21.

Nicholls, S. J., Tuzcu, E. M., Sipahi, I., et al. Statins, high-density lipoprotein cholesterol, and regression of coronary atherosclerosis. Jama. 2007: 297(5): 499-508.

Nicholls, S. J., Tuzcu, E. M., Wolski, K., et al. Coronary artery calcification and changes in atheroma burden in response to established medical therapies. J Am Coll Cardiol. 2007: 49(2): 263-70.

Nieman, K., Cademartiri, F., Lemos, P. A., et al. Reliable noninvasive coronary angiography with fast submillimeter multislice spiral computed tomography. Circulation. 2002: 106(16): 2051-4.

Nieman, K., Oudkerk, M., Rensing, B. J., et al. Coronary angiography with multi-slice computed tomography. Lancet. 2001: 357(9256): 599-603.

Nieman, K., Pattynama, P. M., Rensing, B. J., et al. Evaluation of patients after coronary artery bypass surgery: CT angiographic assessment of grafts and coronary arteries. Radiology. 2003: 229(3): 749-56.

Niendorf, T. and Sodickson, D. K. Parallel imaging in cardiovascular MRI: methods and applications. NMR Biomed. 2006: 19(3): 325-41.

Nikolaou, K., Becker, C. R., Muders, M., et al. Multidetector-row computed tomography and magnetic resonance imaging of atherosclerotic lesions in human ex vivo coronary arteries. Atherosclerosis. 2004: 174(2): 243-52.

Nissen, S. E., Nicholls, S. J., Sipahi, I., et al. Effect of very high-intensity statin therapy on regression of coronary atherosclerosis: the ASTEROID trial. Jama. 2006: 295(13): 1556-65.

Nissen, S. E., Tardif, J. C., Nicholls, S. J., et al. Effect of torcetrapib on the progression of coronary atherosclerosis. N Engl J Med. 2007: 356(13): 1304-16.

Nissen, S. E., Tsunoda, T., Tuzcu, E. M., et al. Effect of recombinant ApoA-I Milano on coronary atherosclerosis in patients with acute coronary syndromes: a randomized controlled trial. Jama. 2003: 290(17): 2292-300.

Nissen, S. E., Tuzcu, E. M., Schoenhagen, P., et al. Effect of intensive compared with moderate lipid-lowering therapy on progression of coronary atherosclerosis: a randomized controlled trial. Jama. 2004: 291(9): 1071-80.

Nissen, S. E., Tuzcu, E. M., Schoenhagen, P., et al. Statin therapy, LDL cholesterol, C-reactive protein, and coronary artery disease. N Engl J Med. 2005: 352(1): 29-38.

Noto, T. J., Jr., Johnson, L. W., Krone, R., et al. Cardiac catheterization 1990: a report of the Registry of the Society for Cardiac Angiography and Interventions (SCA&I). Cathet Cardiovasc Diagn. 1991: 24(2): 75-83.

O'Rourke, R. A., Brundage, B. H., Froelicher, V. F., et al. American College of Cardiology/American Heart Association Expert Consensus document on electron-beam computed tomography for the diagnosis and prognosis of coronary artery disease. Circulation. 2000: 102(1): 126-40.

Oakley, C. Importance of right ventricular function in congestive heart failure. Am J Cardiol. 1988: 62(2): 14A-19A.

Osman, N. F., Kerwin, W. S., McVeigh, E. R., et al. Cardiac motion tracking using CINE harmonic phase (HARP) magnetic resonance imaging. Magn Reson Med. 1999: 42(6): 1048-60.

Pache, G., Saueressig, U., Frydrychowicz, A., et al. Initial experience with 64-slice cardiac CT: non-invasive visualization of coronary artery bypass grafts. Eur Heart J. 2006: 27(8): 976-80.

Pagley, P. R., Beller, G. A., Watson, D. D., et al. Improved outcome after coronary bypass surgery in patients with ischemic cardiomyopathy and residual myocardial viability. Circulation. 1997: 96(3): 793-800.

Pattynama, P. M., Lamb, H. J., van der Velde, E. A., et al. Left ventricular measurements with cine and spin-echo MR imaging: a study of reproducibility with variance component analysis. Radiology. 1993: 187(1): 261-8.

Persy, V., Postnov, A., Neven, E., et al. High-resolution X-ray microtomography is a sensitive method to detect vascular calcification in living rats with chronic renal failure. Arterioscler Thromb Vasc Biol. 2006: 26(9): 2110-6.

Piaw, C. S., Kiam, O. T., Rapaee, A., et al. Use of non-invasive phase contrast magnetic resonance imaging for estimation of atrial septal defect size and morphology: a comparison with transesophageal echo. Cardiovasc Intervent Radiol. 2006: 29(2): 230-4.

Popio, K. A., Gorlin, R., Teichholz, L. E., et al. Abnormalities of left ventricular function and geometry in adults with an atrial septal defect. Ventriculographic, hemodynamic and echocardiographic studies. Am J Cardiol. 1975: 36(3): 302-8.

Prasad, S. K. and Pennell, D. J. Safety of cardiovascular magnetic resonance in patients with cardiovascular implants and devices. Heart. 2004: 90(11): 1241-4.

Prasad, S. K., Soukias, N., Hornung, T., et al. Role of magnetic resonance angiography in the diagnosis of major aortopulmonary collateral arteries and partial anomalous pulmonary venous drainage. Circulation. 2004: 109(2): 207-14.

Raggi, P., Davidson, M., Callister, T. Q., et al. Aggressive versus moderate lipid-lowering therapy in hypercholesterolemic postmenopausal women: Beyond Endorsed Lipid Lowering with EBT Scanning (BELLES). Circulation. 2005: 112(4): 563-71.

Rauch, U., Osende, J. I., Chesebro, J. H., et al. Statins and cardiovascular diseases: the multiple effects of lipid-lowering therapy by statins. Atherosclerosis. 2000: 153(1): 181-9.

Rehr, R. B., Malloy, C. R., Filipchuk, N. G., et al. Left ventricular volumes measured by MR imaging. Radiology. 1985: 156(3): 717-9.

Ritman, E. L. Micro-computed tomography-current status and developments. Annu Rev Biomed Eng. 2004: 6: 185-208.

Roos-Hesselink, J. W., Meijboom, F. J., Spitaels, S. E., et al. Excellent survival and low incidence of arrhythmias, stroke and heart failure long-term after surgical ASD closure at young age. A prospective follow-up study of 21-33 years. Eur Heart J. 2003: 24(2): 190-7.

Ropers, D., Baum, U., Pohle, K., et al. Detection of Coronary Artery Stenoses With Thin-Slice Multi-Detector Row Spiral Computed Tomography and Multiplanar Reconstruction. Circulation. 2003: 107(5): 664-666.

Ross, R. Atherosclerosis -- An Inflammatory Disease. N Engl J Med. 1999: 340(2): 115-126.

Rubins, H. B., Robins, S. J., Collins, D., et al. Gemfibrozil for the secondary prevention of coronary heart disease in men with low levels of high-density lipoprotein cholesterol. Veterans Affairs High-Density Lipoprotein Cholesterol

Intervention Trial Study Group. N Engl J Med. 1999: 341(6): 410-8.

Rumberger, J. A., Sheedy, P. F., Breen, J. F., et al. Coronary calcium, as determined by electron beam computed tomography, and coronary disease on arteriogram. Effect of patient's sex on diagnosis. Circulation. 1995: 91(5): 1363-7.

Rumberger, J. A., Simons, D. B., Fitzpatrick, L. A., et al. Coronary artery calcium area by electron-beam computed tomography and coronary atherosclerotic plaque area. A histopathologic correlative study. Circulation. 1995: 92(8): 2157-62.

Saam, T., Cai, J., Ma, L., et al. Comparison of symptomatic and asymptomatic atherosclerotic carotid plaque features with in vivo MR imaging. Radiology. 2006: 240(2): 464-72.

Saba, L., Sanfilippo, R., Pirisi, R., et al. Multidetector-row CT angiography in the study of atherosclerotic carotid arteries. Neuroradiology. 2007: 49(8): 623-37.

Sacks, F. M., Pfeffer, M. A., Moye, L. A., et al. The effect of pravastatin on coronary events after myocardial infarction in patients with average cholesterol levels. Cholesterol and Recurrent Events Trial investigators. N Engl J Med. 1996: 335(14): 1001-9.

Salehian, O., Horlick, E., Schwerzmann, M., et al. Improvements in cardiac form and function after transcatheter closure of secundum atrial septal defects. J Am Coll Cardiol. 2005: 45(4): 499-504.

Salonen, J. T. and Salonen, R. Ultrasound B-mode imaging in observational studies of atherosclerotic progression. Circulation. 1993: 87(3 Suppl): II56-65.

Schlosser, T., Konorza, T., Hunold, P., et al. Noninvasive visualization of coronary artery bypass grafts using 16-detector row computed tomography. J Am Coll Cardiol. 2004: 44(6): 1224-9.

Schmermund, A., Baumgart, D., Gorge, G., et al. Coronary artery calcium in acute coronary syndromes: a comparative study of electron-beam computed tomography, coronary angiography, and intracoronary ultrasound in survivors of acute myocardial infarction and unstable angina. Circulation. 1997: 96(5): 1461-9.

Schoen, S. P., Kittner, T., Bohl, S., et al. Transcatheter closure of atrial septal defects improves right ventricular volume, mass, function, pulmonary pressure, and functional class: a magnetic resonance imaging study. Heart. 2006: 92(6): 821-6.

Schoenhagen, P., Halliburton, S. S., Stillman, A. E., et al. Noninvasive imaging of coronary arteries: current and future role of multi-detector row CT. Radiology. 2004: 232(1): 7-17.

Schoepf, U. J., Becker, C. R., Ohnesorge, B. M., et al. CT of coronary artery disease. Radiology. 2004: 232(1): 18-37.

Schroeder, S., Kopp, A. F., Baumbach, A., et al. Noninvasive detection and

evaluation of atherosclerotic coronary plaques with multislice computed tomography. J Am Coll Cardiol. 2001: 37(5): 1430-5.

Schroeder, S., Kopp, A. F., Kuettner, A., et al. Influence of heart rate on vessel visibility in noninvasive coronary angiography using new multislice computed tomography: Experience in 94 patients. Clinical Imaging. 2002: 26(2): 106-111.

Schussler, J. M., Anwar, A., Phillips, S. D., et al. Effect on right ventricular volume of percutaneous Amplatzer closure of atrial septal defect in adults. Am J Cardiol. 2005: 95(8): 993-5.

Seifarth, H., Raupach, R., Schaller, S., et al. Assessment of coronary artery stents using 16-slice MDCT angiography: evaluation of a dedicated reconstruction kernel and a noise reduction filter. Eur Radiol. 2005: 15(4): 721-6.

Semelka, R., Tomei, E., Wagner, S., et al. Normal left ventricular dimensions and function: interstudy reproducibility of measurements with cine MR imaging. Radiology. 1990: 174(3): 763-768.

Semelka, R. C., Tomei, E., Wagner, S., et al. Interstudy reproducibility of dimensional and functional measurements between cine magnetic resonance studies in the morphologically abnormal left ventricle. Am Heart J. 1990: 119(6): 1367-73.

Serfaty, J. M., Chaabane, L., Tabib, A., et al. Atherosclerotic plaques: classification and characterization with T2-weighted high-spatial-resolution MR imaging-- an in

vitro study. Radiology. 2001: 219(2): 403-10.

Shah, P. K., Yano, J., Reyes, O., et al. High-dose recombinant apolipoprotein A-I(milano) mobilizes tissue cholesterol and rapidly reduces plaque lipid and macrophage content in apolipoprotein e-deficient mice. Potential implications for acute plaque stabilization. Circulation. 2001: 103(25): 3047-50.

Shaheen, J., Alper, L., Rosenmann, D., et al. Effect of surgical repair of secundum-type atrial septal defect on right atrial, right ventricular, and left ventricular volumes in adults. Am J Cardiol. 2000: 86(12): 1395-7, A6.

Shapiro, E. P., Rogers, W. J., Beyar, R., et al. Determination of left ventricular mass by magnetic resonance imaging in hearts deformed by acute infarction. Circulation. 1989: 79(3): 706-11.

Shaw, L. J., Raggi, P., Schisterman, E., et al. Prognostic value of cardiac risk factors and coronary artery calcium screening for all-cause mortality. Radiology. 2003: 228(3): 826-33.

Shepherd, J., Cobbe, S. M., Ford, I., et al. Prevention of coronary heart disease with pravastatin in men with hypercholesterolemia. West of Scotland Coronary Prevention Study Group. N Engl J Med. 1995: 333(20): 1301-7.

Shinnar, M., Fallon, J. T., Wehrli, S., et al. The diagnostic accuracy of ex vivo MRI for human atherosclerotic plaque characterization. Arterioscler Thromb Vasc Biol.

1999: 19(11): 2756-61.

Sievers, B., Kirchberg, S., Addo, M., et al. Assessment of left atrial volumes in sinus rhythm and atrial fibrillation using the biplane area-length method and cardiovascular magnetic resonance imaging with TrueFISP. J Cardiovasc Magn Reson. 2004: 6(4): 855-63.

Simonetti, O. P., Finn, J. P., White, R. D., et al. "Black blood" T2-weighted inversion-recovery MR imaging of the heart. Radiology. 1996: 199(1): 49-57.

Smedema, J. P., Snoep, G., van Kroonenburgh, M. P., et al. Evaluation of the accuracy of gadolinium-enhanced cardiovascular magnetic resonance in the diagnosis of cardiac sarcoidosis. J Am Coll Cardiol. 2005: 45(10): 1683-90.

Soma, M. R., Donetti, E., Parolini, C., et al. Recombinant apolipoprotein A-IMilano dimer inhibits carotid intimal thickening induced by perivascular manipulation in rabbits. Circ Res. 1995: 76(3): 405-11.

Stary, H. C. The development of calcium deposits in atherosclerotic lesions and their persistence after lipid regression. Am J Cardiol. 2001: 88(2A): 16E-19E.

Stary, H. C., Chandler, A. B., Dinsmore, R. E., et al. A definition of advanced types of atherosclerotic lesions and a histological classification of atherosclerosis. A report from the Committee on Vascular Lesions of the Council on Arteriosclerosis, American Heart Association. Circulation. 1995: 92(5): 1355-74.

Steele, P. M., Fuster, V., Cohen, M., et al. Isolated atrial septal defect with pulmonary vascular obstructive disease--long-term follow-up and prediction of outcome after surgical correction. Circulation. 1987: 76(5): 1037-42.

Sugano, M., Makino, N., Sawada, S., et al. Effect of antisense oligonucleotides against cholesteryl ester transfer protein on the development of atherosclerosis in cholesterol-fed rabbits. J Biol Chem. 1998: 273(9): 5033-6.

Sukhova, G. K., Williams, J. K. and Libby, P. Statins reduce inflammation in atheroma of nonhuman primates independent of effects on serum cholesterol. Arterioscler Thromb Vasc Biol. 2002: 22(9): 1452-8.

Takaya, N., Yuan, C., Chu, B., et al. Presence of intraplaque hemorrhage stimulates progression of carotid atherosclerotic plaques: a high-resolution magnetic resonance imaging study. Circulation. 2005: 111(21): 2768-75.

Takaya, N., Yuan, C., Chu, B., et al. Association between carotid plaque characteristics and subsequent ischemic cerebrovascular events: a prospective assessment with MRI--initial results. Stroke. 2006: 37(3): 818-23.

Teichholz, L. E., Kreulen, T., Herman, M. V., et al. Problems in echocardiographic volume determinations: echocardiographic-angiographic correlations in the presence of absence of asynergy. Am J Cardiol. 1976: 37(1): 7-11.

Thilen, U., Berlind, S. and Varnauskas, E. Atrial septal defect in adults. Thirty-eight-year follow-up of a surgically and a conservatively managed group. Scand Cardiovasc J. 2000: 34(1): 79-83.

Thilen, U. and Persson, S. Closure of atrial septal defect in the adult. Cardiac remodeling is an early event. Int J Cardiol. 2006: 108(3): 370-5.

Toussaint, J. F., LaMuraglia, G. M., Southern, J. F., et al. Magnetic resonance images lipid, fibrous, calcified, hemorrhagic, and thrombotic components of human atherosclerosis in vivo. Circulation. 1996: 94(5): 932-8.

Toussaint, J. F., Southern, J. F., Fuster, V., et al. T2-weighted contrast for NMR characterization of human atherosclerosis. Arterioscler Thromb Vasc Biol. 1995: 15(10): 1533-42.

Tuzcu, E. M., Berkalp, B., De Franco, A. C., et al. The dilemma of diagnosing coronary calcification: angiography versus intravascular ultrasound. J Am Coll Cardiol. 1996: 27(4): 832-8.

van der Wall, E. E., Vliegen, H. W., de Roos, A., et al. Magnetic resonance imaging in coronary artery disease. Circulation. 1995: 92(9): 2723-39.

Veldtman, G. R., Razack, V., Siu, S., et al. Right ventricular form and function after percutaneous atrial septal defect device closure. J Am Coll Cardiol. 2001: 37(8): 2108-13.

Vengrenyuk, Y., Carlier, S., Xanthos, S., et al. A hypothesis for vulnerable plaque rupture due to stress-induced debonding around cellular microcalcifications in thin fibrous caps. Proc Natl Acad Sci U S A. 2006: 103(40): 14678-83.

Virmani, R., Burke, A. P., Farb, A., et al. Pathology of the vulnerable plaque. J Am Coll Cardiol. 2006: 47(8 Suppl): C13-8.

Virmani, R., Burke, A. P., Kolodgie, F. D., et al. Pathology of the thin-cap fibroatheroma: a type of vulnerable plaque. J Interv Cardiol. 2003: 16(3): 267-72.

Virmani, R., Kolodgie, F. D., Burke, A. P., et al. Lessons from sudden coronary death: a comprehensive morphological classification scheme for atherosclerotic lesions. Arterioscler Thromb Vasc Biol. 2000: 20(5): 1262-75.

Walker, R. E., Moran, A. M., Gauvreau, K., et al. Evidence of adverse ventricular interdependence in patients with atrial septal defects. Am J Cardiol. 2004: 93(11): 1374-7, A6.

Wang, S., Detrano, R. C., Secci, A., et al. Detection of coronary calcification with electron-beam computed tomography: evaluation of interexamination reproducibility and comparison of three image-acquisition protocols. Am Heart J. 1996: 132(3): 550-8.

Wasserman, B. A., Smith, W. I., Trout, H. H., 3rd, et al. Carotid artery

atherosclerosis: in vivo morphologic characterization with gadolinium-enhanced double-oblique MR imaging initial results. Radiology. 2002: 223(2): 566-73.

Weber, M., Dill, T., Deetjen, A., et al. Left ventricular adaptation after atrial septal defect closure assessed by increased concentrations of N-terminal pro-brain natriuretic peptide and cardiac magnetic resonance imaging in adult patients. Heart. 2006: 92(5): 671-5.

Wexler, L., Brundage, B., Crouse, J., et al. Coronary artery calcification: pathophysiology, epidemiology, imaging methods, and clinical implications. A statement for health professionals from the American Heart Association. Writing Group. Circulation. 1996: 94(5): 1175-92.

Weyman, A. E., Wann, S., Feigenbaum, H., et al. Mechanism of abnormal septal motion in patients with right ventricular volume overload: a cross-sectional echocardiographic study. Circulation. 1976: 54(2): 179-86.

Wilson, P. W., D'Agostino, R. B., Levy, D., et al. Prediction of coronary heart disease using risk factor categories. Circulation. 1998: 97(18): 1837-47.

Wintersperger, B. J. and Nikolaou, K. Basics of cardiac MDCT: techniques and contrast application. Eur Radiol. 2005: 15 Suppl 2: B2-9.

Wong, N. D., Budoff, M. J., Pio, J., et al. Coronary calcium and cardiovascular event risk: evaluation by age- and sex-specific quartiles. Am Heart J. 2002: 143(3): 456-9.

Wood, J. C. Anatomical assessment of congenital heart disease. J Cardiovasc Magn Reson. 2006: 8(4): 595-606.

Worthley, S. G. and Badimon, J. J. (2005). Magnetic Resonance Imaging of high-Risk Plaque. High-Risk Atherosclerotic Plaques. L. M. Khachigian, CRC Press**:** 101-28.

Worthley, S. G., Helft, G., Fuster, V., et al. High resolution ex vivo magnetic resonance imaging of in situ coronary and aortic atherosclerotic plaque in a porcine model. Atherosclerosis. 2000: 150(2): 321-9.

Worthley, S. G., Helft, G., Fuster, V., et al. Noninvasive in vivo magnetic resonance imaging of experimental coronary artery lesions in a porcine model. Circulation. 2000: 101(25): 2956-61.

Worthley, S. G., Helft, G., Fuster, V., et al. Serial in vivo MRI documents arterial remodeling in experimental atherosclerosis. Circulation. 2000: 101(6): 586-9.

Worthley, S. G., Helft, G., Zaman, A. G., et al. Atherosclerosis and the vulnerable plaque--imaging: Part II. Aust N Z J Med. 2000: 30(6): 704-10.

Yang, P. C., Kerr, A. B., Liu, A. C., et al. New real-time interactive cardiac magnetic resonance imaging system complements echocardiography. J Am Coll Cardiol. 1998: 32(7): 2049-56.

Yuan, C., Beach, K. W., Smith, L. H., Jr, et al. Measurement of Atherosclerotic Carotid Plaque Size In Vivo Using High Resolution Magnetic Resonance Imaging. Circulation. 1998: 98(24): 2666-2671.

Yuan, C., Kerwin, W. S., Ferguson, M. S., et al. Contrast-enhanced high resolution MRI for atherosclerotic carotid artery tissue characterization. J Magn Reson Imaging. 2002: 15(1): 62-7.

Yuan, C., Mitsumori, L. M., Ferguson, M. S., et al. In Vivo Accuracy of Multispectral Magnetic Resonance Imaging for Identifying Lipid-Rich Necrotic Cores and Intraplaque Hemorrhage in Advanced Human Carotid Plaques. Circulation. 2001: 104(17): 2051-2056.

Yuan, C., Zhang, S.-x., Polissar, N. L., et al. Identification of Fibrous Cap Rupture With Magnetic Resonance Imaging Is Highly Associated With Recent Transient Ischemic Attack or Stroke. Circulation. 2002: 105(2): 181-185.

Zhao, X. Q., Yuan, C., Hatsukami, T. S., et al. Effects of prolonged intensive lipid-lowering therapy on the characteristics of carotid atherosclerotic plaques in vivo by MRI: a case-control study. Arterioscler Thromb Vasc Biol. 2001: 21(10): 1623-9.

Zhu, W., Cao, Q. L., Rhodes, J., et al. Measurement of atrial septal defect size: a comparative study between three-dimensional transesophageal echocardiography and the standard balloon sizing methods. Pediatr Cardiol. 2000: 21(5): 465-9.